

Supported liquid phase catalysts

vorgelegt von
Master of Science
Hamideh Ahi
geb. in Amol (Iran)

von der Fakultät II - Mathematik und Naturwissenschaften
der Technischen Universität Berlin
zur Erlangung des akademischen Grades

Doktor der Ingenieurwissenschaften
- Dr.-Ing. -

genehmigte Dissertation

Promotionsausschuss:

Vorsitzender: Prof. Dr. Thorsten Ressler
Gutachter: Prof. Dr. Robert Schlögl
Gutachter: Prof. Dr. Reinhard Schomäcker
Gutachter: Prof. Dr. Klaus Rademann

Tag der wissenschaftlichen Aussprache: 19. Dezember 2017

Berlin 2018

Logic will get you from A
to B. Imagination will take
you everywhere.

- *Albert Einstein* -

Acknowledgement

I am extremely thankful and pay my gratitude to my supervisor Prof. Dr. Robert Schlögl for giving me the opportunity to be a member of the Fritz Haber Institute of the Max-Planck Society (FHI-MPG). His constructive criticism and inspiring guidance during PhD days and project meetings created a motivating atmosphere for me during my PhD period.

I would like to express my deepest thanks and sincere appreciation to Dr. Annette Trunschke for her creative and comprehensive advices, encouragement and unconditional support. This book would not have been in this level without her.

I would also like to express my gratitude to Dr. Frank Rosowski for letting me fulfill my dream of being a member of UniCat-BASF joinLab (BasCat). The regular discussions in monthly BasCat meetings and his generous advice gave me the chance to keep on the purpose of the project.

I appreciate all the help I received from Berlin International Graduate School of Natural Sciences and Engineering (BIG-NSE) in particular from its managing director Dr Jean-Philippe Lonjaret.

At this point I would like to express my appreciation to my defense committee members, Prof. Dr. Robert Schlögl, Prof. Dr. Reinhard Schomäcker, and Prof. Dr. Klaus Rademann, and to Prof. Dr. Thorsten Ressler for taking the chair of the examination board.

I take this opportunity to acknowledge my nice FHI and BasCat colleagues for all the academic support and friendship. In particular, Dr. Yuanqing Wang (DFT calculations), Pierre Kube (reactivity measurements and technical supports), Dr. Frank Girgsdies (XRD), Dr. Detre Teschner (XPS), Dr. Olaf Timpe (XRF) Dr. Andrey Tarasov (TG-MS), Jasmin Allan (TG-MS), Dr. Marc Willinger (SEM), Dr. Thomas Lunkenbein (TEM), Dr. Manfred Schuster, Wiebke Frandsen (SEM/EDX), Maike Hashagen (BET), Maria Heenemann, Marie-M. Millet, Elisabeth Wolf, Anna Wernbacher, Xuan Li, Teng Fu, Hua Fan and Verena Pfeifer.

Last but not least, the most deserved acknowledgement to my parents by devoting some words in my native language, Persian, to them:

پدر و مادر عزیزم، تمام تجربه‌های زیبای زندگیم را مدیون وجود شما هستم.

I extend my gratitude to my only sister, Saiedeh, and her husband, Masoud, for kind endless help and creating a happy life for me.

Last but certainly not least, my love and appreciation extends to my husband, Omid-Henrik, who blesses me with a life of joy in the limited hours that we spend together. This book would not have been possible without his patience and instant mental and scientific support.

Abstract

This thesis deals with the investigation of silica-supported vanadia-based Supported Liquid Phase (SLP) catalysts in Oxidative Dehydrogenation of Propane (ODP). The aim is a better understanding of the structural requirements of oxidation catalysts. The approach is based on the observation that high-performance catalysts in selective oxidation exhibit a thin surface layer, which is chemically and structurally different from the bulk. Furthermore, it has been shown that strain is responsible for high activity. SLP catalysts provide a unique opportunity to study structure-activity relationships, since they can be operated in both solid and molten states. The main criterion, which should be fulfilled, concerns the melting point of the coating, which should be in the range of the target reaction. The potassium vanadate system meets this requirement. Varying the ratio of K:V, mixed as well as single phase compounds with different melting points were formed on the surface of silica (Aerosil) as support.

The thesis is divided into three main parts: The first part deals with the preparation and spectroscopic characterization of the alkali vanadates $K_3V_5O_{14}$ and $K_2V_8O_{21}$, which are used as reference for characterization of the supported catalysts. The focus of the second part is on the exploration of SLP catalysts for the ODP reaction. In the third part supported solid samples were investigated to have a comparison between solid and molten layers.

The performance of SLP catalysts has been studied before and after the melting point of the coated thin layer using reaction data measured in a parallel reaction set-up. The activity is lowered in the liquid state perhaps due to the reduction of the number of active surface sites since no change in the activation energy was observed. Additional experiments were carried out at fixed temperature but at different contact times for solid and super-cooled liquids in order to investigate solid and liquid at same temperature and conversion. The results reveal that an increase in propene selectivity (20-30%) is achieved by operating in the molten state.

A lower coordination number of vanadium in the molten state, demonstrated by in-situ UV-Vis spectroscopy, is proposed as a relevant factor for superior propene selectivity. Partial breaking of bridging bonds during melting is indicated by a decrease in intensity of Raman bands due to M-O-M vibrations at $200-800\text{ cm}^{-1}$. Kinetic data point to changes in the adsorption or activation of propane and oxygen by transformation from solid to liquid state. A higher reaction order for both oxygen and propane demonstrates that activation of the reactants is more demanding when the active phase is in the molten state.

The investigation of supported solid catalysts reveals that the beneficial geometry of active species, low coordination number, and consequently better propene productivity could be also achieved in the solid state. The complex nature of prepared catalysts, however, prevents a detailed investigation and direct comparison of these samples with SLP catalysts.

Zusammenfassung

Diese Arbeit beschäftigt sich mit Vanadiumoxid-basierten Supported-Liquid-Phase-(SLP)-Katalysatoren für die oxidative Dehydrierung von Propan (ODP). Ziel ist ein besseres Verständnis der Zusammenhänge zwischen Struktur und Reaktivität in der Oxidationskatalyse. Die Motivation für diese Studien lag in der Erkenntnis, dass Hochleistungskatalysatoren in der Selektivoxidation durch einen dünnen Oberflächenfilm gekennzeichnet sind, der sich chemisch und strukturell von der Volumenphase unterscheidet. Außerdem wurde beobachtet, dass Verspannungen zu einer höheren Aktivität in Oxidationsreaktionen führen. SLP-Katalysatoren bieten die einzigartige Gelegenheit zur Untersuchung von Struktur-Aktivitäts-Beziehungen, da die Reaktivität sowohl im festen als auch im geschmolzenen Zustand gemessen werden kann. Das Hauptkriterium dabei ist der Schmelzpunkt der Beschichtung. Dieser muss im Bereich der Zielreaktionstemperatur liegen. Das Kaliumvanadat-System wurde gewählt, weil hier Phasen mit unterschiedlichen K zu V Verhältnissen und unterschiedlichen Schmelzpunkten auf der Oberfläche von Siliziumdioxid (Aerosil) als Träger gebildet werden können.

Diese Studie ist in drei Kapitel unterteilt: Der erste Teil beschreibt die Herstellung und spektroskopische Charakterisierung von $K_3V_5O_{14}$ und $K_2V_8O_{21}$. Die Phasen dienen als Referenzen für die Charakterisierung der geträgerten Katalysatoren. Der Schwerpunkt des zweiten Teils liegt auf der Untersuchung der SLP-Katalysatoren in der ODP-Reaktion. Im dritten Teil werden geträgerte Proben untersucht, deren Oberflächenschicht nicht schmilzt, um einen Vergleich zwischen fester und geschmolzener Schicht zu erhalten.

Die Eigenschaften der SLP-Katalysatoren wurden unterhalb und oberhalb des Schmelzpunktes der Beschichtung in der oxidativen Dehydrierung von Propan untersucht. Die Experimente wurden in einem Parallelreaktor durchgeführt. Beim Erreichen des Schmelzpunktes kommt es zu einer Abnahme der Aktivität. Das ist vermutlich auf eine Reduzierung der verfügbaren aktiven Zentren zurückzuführen, denn es wurde keine Änderung der Aktivierungsenergie beobachtet. Außerdem wurden Experimente bei konstanter Temperatur an der festen und der unterkühlten flüssigen Oberflächenschicht unter Variation der Verweilzeit durchgeführt. Die Ergebnisse zeigen, dass im geschmolzenen Zustand bei vergleichbarer Temperatur und gleichem Umsatz eine um 20-30% erhöhte Selektivität zu Propen erreicht werden kann.

Durch in-situ-UV-Vis-Spektroskopie konnte demonstriert werden, dass eine niedrigere Koordinationszahl für Vanadium im geschmolzenen Zustand mit der höheren Selektivität zu Propen im Zusammenhang zu stehen scheint. Die Raman-Spektroskopie weist darauf hin, dass es beim Schmelzen zum Bruch von M-O-M Bindungen kommt. Das ist an einen Intensitätsrückgang entsprechender Banden im Bereich $200-800\text{ cm}^{-1}$ erkennbar. Kinetisch Untersuchungen ergaben höhere Reaktionsordnungen für beide Reaktionspartner im geschmolzenen Zustand. Das deutet darauf hin, dass die Adsorption oder Aktivierung sowohl von Sauerstoff als auch von Propan an der flüssigen Phase schwieriger ist.

Die Untersuchung von geträgerten festen Katalysatoren zeigt, dass eine vorteilhafte Geometrie der aktiven Spezies, charakterisiert durch eine niedrige Koordinationszahl, und die damit verbundene verbesserte Selektivität zu Propen auch durch in der festen Phase erreicht werden kann. Die Komplexität der hergestellten Katalysatoren lässt jedoch eine detaillierte Untersuchung und den direkten Vergleich dieser Proben mit SLP-Katalysatoren nicht zu.

Table of contents

Table of contents	1
1 Introduction	1
1.1 Why selective oxidation?	1
1.2 Supported vanadium oxide catalysts	2
1.3 Supported liquid phase catalysts	5
1.3.1 Sulfuric acid catalyst	5
1.3.2 Dy ₂ O ₃ /MgO supported alkali chloride for oxidative dehydrogenation of propane and ethane	7
1.3.3 The Na-Mn-W-Oxide OCM catalysts	7
1.4 Effect of additives	8
1.5 Motivation and aim of the thesis	10
1.6 Outline of the thesis	12
1.7 Bibliography	13
2 Temperature dependent Raman and UV-Vis spectroscopy of potassium vanadates: K₂V₈O₂₁ and K₃V₅O₁₄	15
2.1 Introduction	15
2.2 Experimental	16
2.2.1 Preparation	16
2.2.2 Characterization	17
2.3 Results	20
2.3.1 Synthesis	20
2.3.2 Raman and IR spectra at ambient temperature	23
2.3.3 Temperature dependent Raman spectroscopy of K ₂ V ₈ O ₂₁	28
2.3.4 Temperature dependent Raman spectroscopy of K ₃ V ₅ O ₁₄	30
2.3.5 Temperature dependent UV-Vis spectroscopy of K ₂ V ₈ O ₂₁	33
2.3.6 Temperature dependent UV-Vis of K ₃ V ₅ O ₁₄	35
2.4 Discussion	36
2.5 Conclusion	37
2.6 Bibliography	38
2.7 Appendix	40
3 Supported liquid phase catalysts; the influence of local geometric structure on selectivity in propane oxidation to propene	53
3.1 Introduction	53
3.2 Experimental	55
3.2.1 Preparation	55
3.2.2 Characterization	55
3.3 Results	58
3.3.1 Physical and chemical properties of the prepared catalysts	58
3.3.2 DSC analysis	63
3.3.3 XPS analysis	66
3.3.4 Catalytic activity test	69
3.3.5 Characterization of spent catalysts	74
3.4 In-situ characterizations	78

3.4.1	High temperature XPS	78
3.4.2	In-situ Raman.....	80
3.4.3	In-situ UV-Vis spectroscopy	84
3.5	Discussion	86
3.6	Conclusion	89
3.7	Bibliography	91
3.8	Appendix	93
4	In-situ formation of potassium doped vanadium monolayer on silica applying thermal spreading method	95
4.1	Introduction	95
4.2	Experimental	96
4.2.1	Preparation	96
4.2.2	Characterization	97
4.3	Results	100
4.3.1	Physical and chemical properties of prepared catalysts.....	100
4.3.2	Oxidative dehydrogenation of propane	101
4.3.3	Characterization of fresh catalysts	103
4.3.4	Characterization of spent catalysts.....	107
4.4	In-situ characterization	111
4.4.1	High temperature XRD.....	111
4.4.2	High temperature XPS	112
4.4.3	In-situ Raman.....	113
4.4.4	In-situ UV-Vis spectroscopy	116
4.5	Discussion	119
4.6	Conclusion	120
4.7	Bibliography	122
4.8	Appendix	124
5	Summary and final conclusions	127
	Abbreviations	131
	List of Figures	133
	List of tables	135

1 Introduction

1.1 Why selective oxidation?

Steam cracking, fluid catalytic cracking, and catalytic dehydrogenation, nowadays, are the main sources of olefins. These processes, however, suffer from some intrinsic limitations. As it can be seen in Figure 1.1; ethene is the main product in steam cracking while the demand for propene, especially in Western Europe, is greater. Propene yield is quite low for fluid catalytic cracking as well. Regarding the dehydrogenation, one needs to deal with thermodynamic constraints and problem of coking.¹

On the other hand, change of operating conditions in steam and catalytic cracking, and unstable situation regarding availability of their feed stock, initiated from instability in Middle East, have brought about new interest for substitution of the oil-based feedstocks by natural gas as initial material for production of value added chemicals. This trend speeded up mainly in the US after the shale gas revolution. Moreover, due to low cost and minor environmental impact of lower alkanes intense research effort has been devoted to utilization of low hydrocarbons such as propane as feedstock.²

Among the existing alkane oxidation reactions only n-butane oxidation and propane ammoxidation have reached the stage of commercialization. Oxidative Dehydrogenation of Propane (ODP), owing improved selectivity due to producing propene as the main product is effective provocation.¹

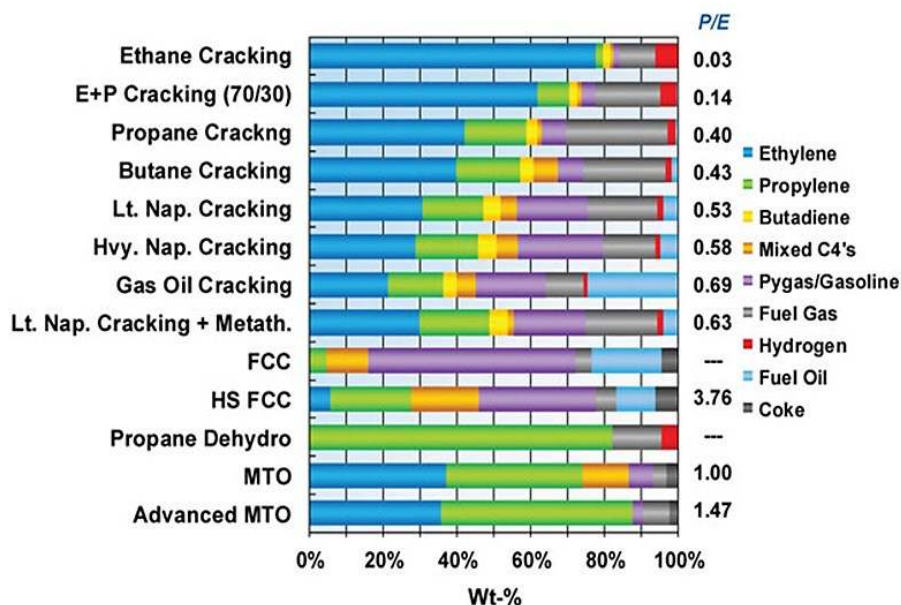


Figure 1.1. Yields of various propene production processes.

Therefore, a great deal of effort has been devoted to overcome economic constraints of ODP reaction by improvements in catalysts, reactor and process design. In terms of catalysts, the main focus was on vanadia based catalysts due to superior performance of this family of material in selective oxidation reactions.

1.2 Supported vanadium oxide catalysts

Vanadia based catalysts, owing superior performance in selective oxidation of propane, will be explained here in more detail. A deeper knowledge on structure-activity/selectivity relationship in oxidative reaction on vanadium oxide catalysts can be beneficial in sorting out the challenge of increasing the selectivity. This topic has been investigated in literatures.^{1, 3-5} Applying a proper loading for preparation of supported vanadia can lead to dispersed surface vanadia species. The structural properties of surface vanadia species on the support was investigated applying several in-situ spectroscopy characterizations. The characterizations applying solid state ^{51}V NMR^{6, 7} and XANES/EXAFS⁸ reveal tetrahedral coordination for vanadia species in dehydrates state. The presence of V-O-V bridging bonds and polymeric structure of vanadia was confirmed by Raman and UV-Vis spectroscopies.⁹ Potential structures of supported vanadium oxide surface species on fully oxidized and partially reduced surfaces are depicted in Figure 1.2. Tuning the loading of vanadia on the

surface of support can yield on different surface structures. The isolated surface VO_4 species which are present at low loadings turn to polymeric surface VO_4 species close to monolayer coverage.³ Depending on the target reaction either of the configurations can be beneficial.

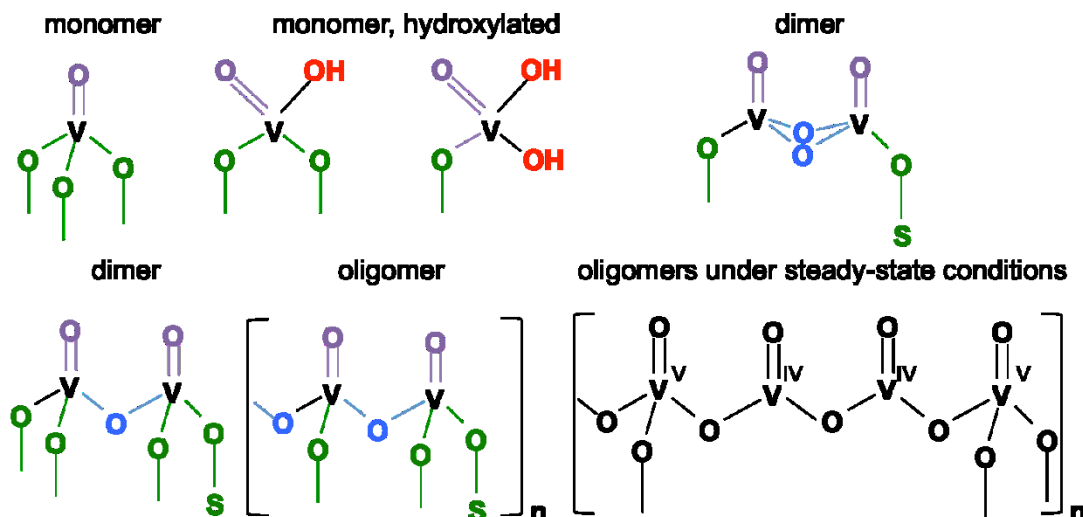


Figure 1.2. Potential structures of supported vanadium oxide surface species on fully oxidized and partially reduced surfaces; color code: vanadyl oxygen in purple, V-O-V bridges in blue, V-O-support bridges in green, vanadium hydroxyl groups in red.

If the reaction requires one oxygen or two electrons the isolated vanadia can perform as good as polymeric surface species. In the case of reaction like oxidation of *n*-butane to maleic anhydride¹⁰ and oxidation of propene to acrolein¹¹ polymeric configuration is favorable due to more oxygen which is available on the surface. Consistent with that, the measurement of kinetic isotope effects over silica-supported vanadium oxide and polycrystalline MoVTenb oxide with M1 structure has demonstrated essential diversities.¹² While applying M1 as catalyst, the propane consumption rate was influenced by deuteration of both methylene and the methyl groups. Therefore, for M1 a simultaneous abstraction of two hydrogen atoms has been proposed based on results of KIEs measurement. In contrast, in the case of V/SBA-15 only the substitution of hydrogen by deuterium in methylene position affects the overall consumption rate of propane. Accordingly, the abstraction of hydrogen atoms is occurring in two separate steps for V/SBA-15, considering as a reason for different performance of this catalyst in selective oxidation of propane. One possible explanation for observed distinction could be the higher number of propane adsorption sites on the surface of M1 when comparing with V/SBA-15.¹³

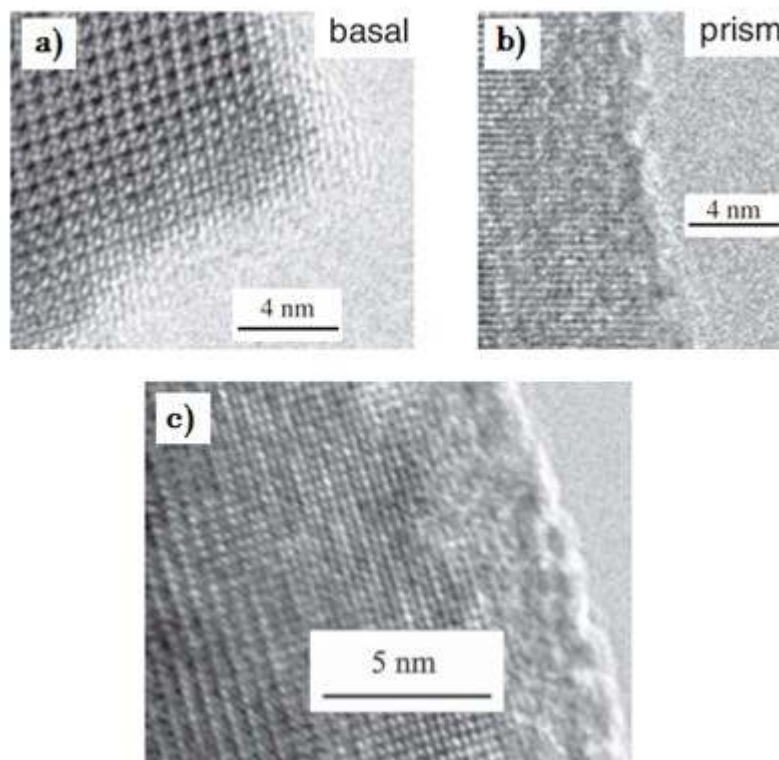


Figure 1.3. HR-TEM of the a) basal b) prism c) Non-crystalline adlayer on the surface of a VPP particle. (adopted from Ref 15)

The characterization techniques such as Raman, UV-Vis DRS, X-ray absorption spectroscopy, HR-TEM, solid state NMR which allows us to investigate amorphous phases opened up new insight into the field of heterogeneous catalysts. It was demonstrated that the amorphous metal oxides which are in most of the cases present on the surface of catalyst are the more relevant catalytic active sites.^{5, 14} The presence of the amorphous over layer on the surface of VPO catalyst was proved by HR-TEM^{14, 15} and in-situ XAS¹⁶ studies, see Figure 1.3.

The existing research areas of propane oxidative dehydrogenation reaction are more focused on heterogeneous gas phase processes with solid catalysts. Although, in the case of most promising catalysts for oxidation of propane (M1)¹⁷ and n-butane (VPO)^{14, 15} surface termination or formation of amorphous over layer on the surface of phase pure crystalline material was reported. Taking this point into the consideration, investigation of amorphous material in oxidation of lower alkanes will certainly be a challenge for the future. Therefore activation of alkanes on the molten layer, being a good representative for amorphous over-layer, can open up interesting possibilities for further understanding of lower alkane oxidation catalysts.

1.3 Supported liquid phase catalysts

Depending on type of catalyst or reaction the molten layer can be playing different roles; as an exchanging medium, as a solvent, or it can be itself a catalyst.¹⁸ This work is dealing with the last category, applying molten layer as catalyst. Examples for application of molten catalysts will be given in following.

Important examples in catalysis

The molten catalysts have been applied in a variety of reaction such as condensation, cracking, isomerization, halogenation, oxychlorination, the deacon reaction, and oxidation reactions.¹⁸ Activation of hydrocarbons which is relevant to our study has been also subject of study. Supported melts of Cu-Cl-KCl which contain PdCl_2 have been employed for oxidation of ethene and propene.¹⁹ The formation of acetaldehyde from hydrocarbon applying molten metal oxychloride has been also investigated. (German Patent 2, 47, 43. 1973). In addition, vapor phase oxidation of aromatic hydrocarbons on fused salts (US. Patent 3, 12, 43. 1958.) and conversion of naphthalene and p-xylene to phthalic anhydride on $\text{K}_2\text{S}_2\text{O}_7\text{-V}_2\text{O}_5$ (British Patent 1, 82, 26. 1967) have been patented by I.C.I and BASF, respectively. Methane pyrolysis on a molten media was also investigated and it was demonstrated that applying molten catalyst the problem of coking can be overcome.²⁰

Three of relevant examples where the active phase was completely or partly molten have been selected to be explained with more detail here.

1.3.1 Sulfuric acid catalyst

The best example for industrial application of SLP catalysts is the sulfuric acid catalyst. The oxidation of sulfur dioxide to sulfur trioxide, the important step in sulfuric acid production, is performed on a alkali promoted vanadium pentoxide.¹⁸ The active phase, which is dispersed on an inert porous support, forms an alkali pyrosulfate melt under the reaction conditions. The later forms after taking up SO_2 from reaction feed.²¹ However, a dynamic transformation of different species is expected under different reaction conditions.²² The mentioned processes can be written as follows:²³



Where, l: liquid, g: gas, and melt: gaseous species dissolved in the liquid

As it can be seen from the reactions, the composition of gas in the environment can influence the composition of the melt. Therefore different species could be present under the reaction conditions. Three possible structures for this catalyst are shown in Figure 1.4.²⁴ Figure 1.4a illustrates the molecular structure of catalysts under O_2 atmosphere. The possible structure under the reaction feed and at low temperatures which is accompanied by reduction and solidification of the active phase are depicted in Figure 1.4b and 1.4c, respectively. The molten pyrosulfate has the ability to dissolve vanadium oxide in it which is considered as active specie for activation of SO_2 and O_2 . The presence of alkali is beneficial for lowering the melting point²⁵, which correlates with a higher stability of the catalyst. Catalyst deactivation occurs via solidification and consequent transformation of V^{5+} to V^{4+} .²³

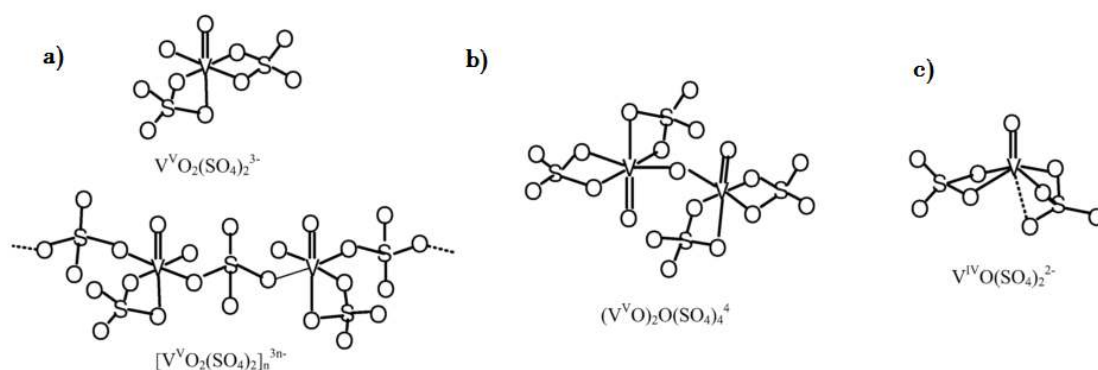


Figure 1.4. Molecular structural models for vanadium species in sulfuric acid catalyst.
(adopted from Ref 24)

1.3.2 Dy₂O₃/MgO supported alkali chloride for oxidative dehydrogenation of propane and ethane

Activation of hydrocarbons on molten layers has been the point of interest, once again recently. Oxidative dehydrogenation of light alkanes on supported molten alkali metal chloride catalysts was investigated by J. A. Lercher and coworkers.²⁶⁻²⁸

The melting point of coating was reduced by introducing alkali. An increase in selectivity to the alkene by lowering the melting point was reported.^{26, 27} Isolated hypochloride anions were proposed as active sites,^{26, 28} while high mobility of cations and anions was considered to be responsible for higher selectivity.^{26, 27} The high mobility can improve the selectivity via facilitating desorption of formed alkenes and preventing further oxidation.^{26, 27} Lower number of Lewis sites, however, could also contribute to higher selectivity.²⁶

In this special case low stability of catalyst due to volatile chloride should be taken into consideration.

1.3.3 The Na-Mn-W-Oxide OCM catalysts

Oxidative Coupling of Methane (OCM) to ethane and ethylene is an attractive alternative to the production of crude-oil-based bulk chemicals, but suitable catalysts that fulfil all desired criteria with respect to activity, selectivity, and stability have not been identified yet. A large number of chemically different materials have been investigated over the last 30 years.^{29, 30} Manganese, and tungsten belong to the key elements that exhibit a positive impact on the catalyst activity³¹, whereas alkali metals used as dopants increase the selectivity of the host oxides³⁰. Due to high thermodynamic stability of methane, the reaction temperatures applied in OCM are usually above 730 °C. Under these reaction conditions, liquefaction of an active component that contains alkali and transition metal oxides should be taken into consideration. Sodium tungstate (Na₂WO₄), for instance, is known to be present on the surface of catalyst at room temperature.³²⁻³⁶ Knowing the melting point of this substance at 695 °C, presence of crystalline Na₂WO₄ under the OCM working conditions is impossible. Simon et al.³⁷ have investigated Mn-Na-W/SiO₂ catalysts prepared via fluidized bed processing. Based on Differential Thermal Analysis (DTA) of as-prepared catalysts, indication for phase transition of Na₂WO₄ from solid to liquid was observed. Furthermore, a study on

isothermal phase diagram of the $\text{Na}_2\text{O}-\text{WO}_3-\text{MnO}-\text{Mn}_2\text{O}_3$ and $\text{Na}_2\text{O}-\text{WO}_3-\text{Mn}_2\text{O}_3-\text{SiO}_2$ has demonstrated presence of molten Na_2WO_4 that favors formation of tridymite- SiO_2 .³⁸ Probable formation of a layer of molten Na_2WO_4 ³⁹ and amorphous features of working catalysts⁴⁰ were also addressed in other papers. However, it has not been established so far whether the discussed liquefaction is responsible for the high performance of this catalyst or if there are some other phenomena going on as a consequence of this phase transition.

1.4 Effect of additives

Lowering of melting point to meet the temperature range of desired reaction is an important issue in preparation of SLP catalysts. Introducing additives to catalysts is an appropriate way of dealing with this obstacle. Therefore, the effect of additives in performance of prepared catalysts needed to be considered. Alkali elements are frequently used as fluxing agents. Improvement of catalysts performance applying additives has been investigated intensively in literatures.¹ However, the role of alkali on structure and properties of supported vanadia catalysts is still not fully understood. Two crucial factors in ODH reactions are acid base characters and redox properties.^{41 42} It is agreed upon that the addition of alkali can influence both acid base and redox properties of catalysts. An olefin as a base (nucleophile) is more difficult to adsorb on a basic surface than an acidic one.⁴³ The effect of additives in terms of increasing basicity of active center has been demonstrated before, performing isopropanol decomposition as a probe reaction.^{44, 45} However, it has been shown that not the basicity itself but electron density around the active center could play the major role for higher selectivity.⁴⁴ The environment of the metal oxygen bond can change the degree of polarization and consequently the oxygen will exhibit electrophilic or nucleophilic properties. The nucleophilic oxygen will favor dehydrogenation reaction by forming OH groups.⁴² It was demonstrated previously that for the active center to be more selective for partial oxidation products, higher electron density would be necessary to decrease the surface energy barrier which is needed to transfer electrons from catalyst to adsorbed reactant.⁴⁶ Theoretical calculations demonstrated that K cation can not only transfer its electrons to neighboring oxygen anions but also to the vanadyl group which makes it one of the best additives.⁴³

The activity of alkali doped catalysts, however, was decreased due to a decrease in redox properties of active site.

1.5 Motivation and aim of the thesis

In the present work the impact of phase transition from solid to liquid on performance of supported catalysts is investigated. The focus is on comparison of performance before and after melting of the active layer. The potassium vanadates have been selected for preparation of silica-supported model catalysts due to appropriate melting points of these solids (390-520 °C), which are within the range of reaction temperatures usually applied in the oxidative dehydrogenation of alkanes. Oxidative Dehydrogenation of Propane (ODP) will be performed as test reaction. The melting point of the supported $K_2O-V_2O_5$ mixture is varied by changing the potassium to vanadium ratio in the coating. The investigation of the prepared model catalysts under operation conditions of ODP reaction applying kinetic and spectroscopic studies will give an insight into the impact of phase transformation on activity and selectivity in the activation of lower alkanes. In particular, the role of the coordination environment of the active vanadium oxide surface species with respect to catalytic performance in the ODP reaction will be addressed.

In previous studies it was demonstrated that strain in supported metal oxide species leads to higher rates in C-H activation reactions due to a high potential energy at the active oxygen that facilitates C-H bond splitting.⁴⁷ In the molten state the formation of structurally equilibrated species is assumed. To scrutinize the impact of strain on reactivity further, we pursue in the present work the following approach:

1. Synthesis of supported liquid-phase catalysts and investigation of phase transition, homogeneity, and structure of the supported solid and liquefied species by using differential calorimetry, X-ray diffraction, and spectroscopic techniques.
2. Synthesis and characterization of reference V-K compounds to study phase transitions, spectroscopic properties and reactivity in absence of the support.
3. Investigation of the synthesized catalysts in the oxidative dehydrogenation of propane with respect to activity and selectivity.
4. Operando studies applying Raman and UV-Vis spectroscopy to analyze correlations between changes in the structure of the supported metal oxide species and reactivity in the oxidative dehydrogenation of propane.

The task is challenging, because an analysis of the influence of structural changes during melting on the reactivity of the supported catalysts requires homogeneity of the supported phase. However, the interaction of the potassium vanadate species with the silica support may change the melting behavior of the mixed V-K oxides and cause chemical and/or morphological modifications of the support. Furthermore, the sensitivity of the characterization techniques is crucial and needs a certain loading. Therefore, high loadings close to and above a monolayer will be prepared and comprehensive *in operando* analysis will only be performed using catalysts that show phase transitions of the entire supported phase with the aim to establish relations between the structure of vanadium oxide species and activity and selectivity in propane oxidation.

1.6 Outline of the thesis

Chapter 2 provides a detailed discussion on preparation and characterization of two prominent phases in the phase diagram, $K_2V_8O_{21}$ and $K_3V_5O_{14}$, with the focus on temperature-dependent Raman and UV-Vis spectroscopy to provide a database applicable as a reference for characterization of supported catalysts.

Chapter 3 deals with the synthesis, characterizations and reactivity test of potassium vanadate based SLP catalysts. This chapter is targeted on feasibility study on applying this new family of catalysts in oxidative dehydrogenation of propane. Formation of molten layer is observed by DSC and further proved by high temperature XRD. An increase in selectivity to propene in ODP reaction at comparable conversions is observed after phase transition from solid to liquid. The possible reasons for the superior selectivity of molten layer were studied applying in-situ Raman, in-situ UV-Vis spectroscopy and kinetic investigations. A correlation between the lower coordination number for vanadium centers induced after liquefaction and increased selectivity to propene are established. The concept provides a promising approach for achieving increased propene selectivity in activation of propane.

Chapter 4 is devoted to solid samples still in the potassium vanadates system to have a comparison between supported liquid and solid catalysts. The low coordinated vanadium species is shown to be beneficial with respect to selectivity for solid catalysts as well.

Chapter 5 includes final conclusions and outlook.

1.7 Bibliography

1. F. Cavani, N. Ballarini and A. Cericola, *Catalysis Today*, 2007, **127**, 113-131.
2. G. Centi, F. Cavani and F. Trifirò, *Selective Oxidation by Heterogeneous Catalysis*, Springer US, 2001.
3. C. A. Carrero, R. Schloegl, I. E. Wachs and R. Schomaecker, *ACS Catalysis*, 2014, **4**, 3357-3380.
4. G. C. Bond and S. F. Tahir, *Applied Catalysis*, 1991, **71**, 1-31.
5. I. E. Wachs, *Catalysis Today*, 2005, **100**, 79-94.
6. H. Eckert and I. E. Wachs, *MRS Proceedings*, 2011, **111**.
7. H. Eckert and I. E. Wachs, *The Journal of Physical Chemistry*, 1989, **93**, 6796-6805.
8. T. Tanaka, H. Yamashita, R. Tsuchitani, T. Funabiki and S. Yoshida, *Journal of the Chemical Society, Faraday Transactions 1: Physical Chemistry in Condensed Phases*, 1988, **84**, 2987-2999.
9. M. A. Bañares, M. V. Martínez-Huerta, X. Gao, J. L. G. Fierro and I. E. Wachs, *Catalysis Today*, 2000, **61**, 295-301.
10. I. E. Wachs, J.-M. Jehng, G. Deo, B. M. Weckhuysen, V. V. Guliants, J. B. Benziger and S. Sundaresan, *Journal of Catalysis*, 1997, **170**, 75-88.
11. C. Zhao and I. E. Wachs, *Catalysis Today*, 2006, **118**, 332-343.
12. P. Kube, B. Frank, R. Schlögl and A. Trunschke, *ChemCatChem*, n/a-n/a.
13. P. Kube, B. Frank, S. Wrabetz, J. Kröhnert, M. Hävecker, J. Velasco-Vélez, J. Noack, R. Schlögl and A. Trunschke, *ChemCatChem*, 2017, n/a-n/a.
14. V. V. Guliants, J. B. Benziger, S. Sundaresan, N. Yao and I. E. Wachs, *Catal Lett*, 1995, **32**, 379-386.
15. H. Bluhm, M. Hävecker, E. Kleimenov, A. Knop-Gericke, A. Liskowski, R. Schlögl and D. S. Su, *Top Catal*, 2003, **23**, 99-107.
16. M. Hävecker, A. Knop-Gericke, H. Bluhm, E. Kleimenov, R. W. Mayer, M. Fait and R. Schlögl, *Applied Surface Science*, 2004, **230**, 272-282.
17. C. Heine, M. Hävecker, M. Sanchez-Sanchez, A. Trunschke, R. Schlögl and M. Eichelbaum, *The Journal of Physical Chemistry C*, 2013, **117**, 26988-26997.
18. C. N. Kenney, *Catal Rev*, 1975, **11**, 197-224.
19. P. R. Rony, *Annals of the New York Academy of Sciences*, 1970, **172**, 238-243.
20. B. Parkinson, J. W. Matthews, T. B. McConaughy, D. C. Upham and E. W. McFarland, *Chemical Engineering & Technology*, 2017, **40**, 1022-1030.
21. J. H. Frazer and W. J. Kirkpatrick, *Journal of the American Chemical Society*, 1940, **62**, 1659-1660.
22. K. M. Eriksen, D. A. Karydis, S. Boghosian and R. Fehrmann, *Journal of Catalysis*, 1995, **155**, 32-42.
23. F. Cavalca, P. Beato, J. Hyltoft, K. Christensen and S. Helveg, *The Journal of Physical Chemistry C*, 2017, **121**, 3350-3364.
24. A. Christodoulakis and S. Boghosian, *Journal of Catalysis*, 2003, **215**, 139-150.
25. F. J. Doering and D. A. Berkel, *Journal of Catalysis*, 1987, **103**, 126-139.
26. C. P. Kumar, S. Gaab, T. E. Müller and J. A. Lercher, *Top Catal*, 2008, **50**, 156-167.
27. B. Tope, Y. Zhu and J. A. Lercher, *Catalysis Today*, 2007, **123**, 113-121.
28. C. A. Gartner, A. C. van Veen and J. A. Lercher, *Journal of the American Chemical Society*, 2014, **136**, 12691-12701.
29. S. Arndt, T. Otremba, U. Simon, M. Yildiz, H. Schubert and R. Schomäcker, *Appl Catal A Gen*, 2012, **425-426**, 53-61.

30. U. Zavyalova, M. Holena, R. Schlögl and M. Baerns, *ChemCatChem*, 2011, **3**, 1935-1947.
31. S. F. Ji, T. C. Xiao, S. B. Li, C. Z. Xu, R. L. Hou, K. S. Coleman and M. L. H. Green, *Applied Catalysis a-General*, 2002, **225**, 271-284.
32. Y. T. Chua, A. R. Mohamed and S. Bhatia, *Applied Catalysis a-General*, 2008, **343**, 142-148.
33. T. W. Elkins and H. E. Hagelin-Weaver, *Applied Catalysis a-General*, 2015, **497**, 96-106.
34. H. R. Godini, A. Gili, O. Gorke, S. Arndt, U. Simon, A. Thomas, R. Schomacker and G. Wozny, *Catalysis Today*, 2014, **236**, 12-22.
35. T. Serres, C. Aquino, C. Mirodatos and Y. Schuurman, *Applied Catalysis a-General*, 2015, **504**, 509-518.
36. V. Salehoun, A. Khodadadi, Y. Mortazavi and A. Talebizadeh, *Chemical Engineering Science*, 2008, **63**, 4910-4916.
37. U. Simon, O. Görke, A. Berthold, S. Arndt, R. Schomäcker and H. Schubert, *Chemical Engineering Journal*, 2011, **168**, 1352-1359.
38. G. D. Nipan, *Inorg Mater+*, 2014, **50**, 1012-1017.
39. R. Koirala, R. Buchel, S. E. Pratsinis and A. Baiker, *Applied Catalysis a-General*, 2014, **484**, 97-107.
40. Y. Kou, B. Zhang, J. Z. Niu, S. B. Li, H. L. Wang, T. Tanaka and S. Yoshida, *Journal of Catalysis*, 1998, **173**, 399-408.
41. A. Corma and H. García, *Chem. Rev.*, 2002, **102**, 3837-3892.
42. J. C. Vedrine, J. M. M. Millet and J.-C. Volta, *Catalysis Today*, 1996, **32**, 115-123.
43. A. Klisińska, A. Haras, K. Samson, M. Witko and B. Grzybowska, *J. Mol. Catal. A Chem.*, 2004, **210**, 87-92.
44. R. Grabowski, B. Grzybowska, K. Samson, J. Słoczyński, J. Stoch and K. Wcisło, *Appl Catal A Gen*, 1995, **125**, 129-144.
45. B. Grzybowska, P. Mekšs, R. Grabowski, K. Wcisło, Y. Barboux and L. Gengembre, in *Studies in Surface Science and Catalysis*, eds. V. C. Corberán and S. V. Bellón, Elsevier, 1994, vol. Volume 82, pp. 151-158.
46. B. Grzybowska, J. Słoczyński, R. Grabowski, K. Samson, I. Gressel, K. Wcisło, L. Gengembre and Y. Barboux, *Applied Catalysis a-General*, 2002, **230**, 1-10.
47. K. Amakawa, L. L. Sun, C. S. Guo, M. Havecker, P. Kube, I. E. Wachs, S. Lwin, A. I. Frenkel, A. Patlolla, K. Hermann, R. Schlögl and A. Trunschke, *Angewandte Chemie-International Edition*, 2013, **52**, 13553-13557.

2 Temperature dependent Raman and UV-Vis spectroscopy of potassium vanadates: $K_2V_8O_{21}$ and $K_3V_5O_{14}$

2.1 Introduction

In recent years, supported vanadium monolayer catalysts have been receiving more attention due to their potential use in oxidation of lower alkanes¹. Alkali doping is shown to be quite promising in improving the performance of vanadia based catalysts.^{1, 2} It is agreed upon that the addition of alkali can have a beneficial effect for selectivity to alkenes by increasing the basicity^{3, 4} and electron density³ of the active center. For the structural-activity relationship interpretations, knowledge about the molecular structure of surface vanadium species is essential. With respect to potassium doped catalysts, formation of a minor amount of potassium vanadates via doping should be taken into consideration. Presence of amorphous or crystalline support may hinder detection of formed potassium vanadate phases, especially in XRD, if it is in minor amount. Accordingly, further characterization techniques would help for detection of the nano-crystalline phases which may play an important role in catalysis. $K_2V_8O_{21}$ and $K_3V_5O_{14}$ as two possible phases were selected to study in more detail here. The spectroscopic characterization data of these materials could be used as finger print for detection of these phases in the catalysts. In literature, the crystalline structure of $K_2V_8O_{21}$ was determined by X-ray and neutron powder

diffraction⁵. Besides, $K_2V_8O_{21}$ has been characterized with various characterization techniques such as Raman⁶, SEM⁷, IR⁶, EPR⁶. Regarding $K_3V_5O_{14}$ there are also studies concerning preparation and initial characterization, namely IR and UV-Vis spectroscopy.⁸⁻¹³ On the other hand, information about UV-Vis and XPS spectroscopy of $K_2V_8O_{21}$, Raman spectra of $K_3V_5O_{14}$ and specially the behavior of these materials at high temperatures are missing. Moreover, no vibrational assignments have been conducted for the Raman and IR spectral features of $K_2V_8O_{21}$ and $K_3V_5O_{14}$ using DFT calculations based on the crystal structure. Therefore, reproduction of this material along with full characterization, as well as applying theory calculation for support of performed experiments would add valuable information. As regards special application in catalysis, the behavior of alkalivanadates at high temperatures turns to be more relevant. Apart from some ex-situ studies on reduction behavior of $K_2V_8O_{21}$ at high temperatures⁶, a systematic high temperature characterization for possible temperature induced changes has not been conducted so far.

The subject of our study was the synthesis of $K_2V_8O_{21}$ and $K_3V_5O_{14}$ along with full characterizations. The investigations involved several techniques, including XRD, BET, XRF, DSC, SEM, TEM, IR, XPS, Raman and UV-Vis spectroscopy. This study tries to go one step further by using DFT calculations to determine vibrational assignments to the Raman and IR spectral features of crystalline $K_2V_8O_{21}$ and $K_3V_5O_{14}$. Besides, temperature dependent UV-Vis spectroscopy and temperature dependent Raman enabled an insight into the course of stability of these materials under increased temperatures and associated changes of the structure upon melting.

2.2 Experimental

2.2.1 Preparation

$K_2V_8O_{21}$ was prepared according to the procedure reported by V. N. Krasil'nikov et al.⁵ with minor alterations. Briefly, V_2O_5 (BASF) and K_2CO_3 (Merck) have been used as precursors after drying at 110 °C and 300 °C, respectively. The precursors were mixed with stoichiometric ratio and ground finely, then pressed to small pellets. Thermal annealing at 450 °C for 50 h under the flow of 100 ml/min oxygen, following by slow cooling down to room temperature led to phase-pure $K_2V_8O_{21}$.

For preparation of phase-pure $K_3V_5O_{14}$, likewise, solid state synthesis was employed. The synthesis procedure was adapted from J. Yeon et al.⁸, applying one washing step at the end to remove impurities. To do so, KNO_3 (Merck) and V_2O_5 (BASF) were mixed with stoichiometric ratio and ground for 1 h. The prepared mixture was pressed to small pellets and heated to 380 °C in flowing 21 % O_2 in Ar and held there for 4 days, then cooled down slowly to room temperature. The procedure was repeated three times and the final step was washing with water to remove the remains of KVO_3 which was present as impurity. The washed powder was dried at 80 °C for 2 hours and calcined once more at 380 °C for 5 h to receive the final $K_3V_5O_{14}$ catalyst with 100 % purity.

2.2.2 Characterization

X-ray Diffraction (XRD)

The X-ray diffraction (XRD) measurements were performed in Bragg-Brentano geometry on a Bruker AXS D8 Advance II theta/theta diffractometer, applying Ni filtered $Cu\ K\alpha$ radiation and a position sensitive energy dispersive LynxEye silicon strip detector. The catalyst powder was filled into the recess of a cup-shaped catalyst holder, the surface of the powder bed being flush with the catalyst holder edge (front loading). The temperature dependent XRD data were collected on a STOE Theta/theta X-ray diffractometer ($CuK\alpha$ radiation, secondary graphite monochromator, scintillation counter) equipped with an Anton Paar XRK 900 in-situ reactor chamber with the gas feed flowing from the top to the bottom of the chamber. The temperature was measured by two type K thermocouples. While the first one (TC1) was in close contact to the catalyst bed, the second thermocouple (TC2) was situated near the entrance of the gases.

X-ray Fluorescence (XRF)

The amount of potassium and vanadium in the prepared samples was determined by X-ray fluorescence analysis (XRF). The sample and corresponding standards were mixed with lithiumtetraborate flux (FX-X100, Fluxana) and fused in a Vulcan Fusion Machine (HD Electronic & Elektrotechnik GmbH) under formation of flat molten glass discs, which were analyzed by X-Ray fluorescence spectroscopy using the spectrometer Pioneer S4 (Bruker AXS GmbH). The XRF instrument was wavelength dispersive and equipped with a Rh-anode.

BET

The surface area of the samples was analyzed by nitrogen adsorption (Autosorb AS-6B, Quantachrome) after a pretreatment at 150 °C for 1.5 h in vacuum. The specific surface area was determined according to the Brunauer–Emmett–Teller (BET) method using 11 data points in the relative pressure p/p_0 range of 0.05–0.3.

Attenuated total reflectance-Infrared (ATR-IR) Spectroscopy

The ATR-IR spectra were recorded in a range between 5000 and 500 cm^{-1} with a Perkin Elmer PE100 spectrometer equipped with a MIR-TGS detector. An ATR accessory with a Ge-crystal was used. In general, 8 scans were collected for each sample at a resolution of 2 cm^{-1} . Ambient air served as background without using pressing force. The focus is concentrated between 1200 and 600 cm^{-1} .

Differential Scanning Calorimetry (DSC)

Calorimetric experiments were carried out on a Mettler-Toledo HP DSC 827 calorimeter, with Au–AuPd Sensor, in an alumina crucible in a dynamic 21 % O_2 / 79 % Ar (70 ml/min) flow with 10 Kpm heating rate and 5 Kpm cooling rate. Temperatures were calibrated against the melting points of In and Zn.

X-ray Photoelectron Spectroscopy (XPS)

In XPS analysis, samples were investigated as pressed pellets. Spectra were recorded at room temperature, using non-monochromatized Al $K\alpha$ (1486.6 eV) excitation and a hemispherical analyzer (Phoibos 150, SPECS). The binding energy scale was calibrated by the standard Au4f(7/2) and Cu2p(3/2) procedure and was adjusted so that the O1s main peak appears at 530 eV. To calculate the elemental composition, theoretical cross sections from Yeh and Lindau¹⁴ were applied.

UV-Vis spectroscopy

Samples were investigated in a Cary 5000 UV-Vis spectrometer. All data were obtained in % reflectance and then converted to the Kubelka-Munk function. Spectralon was loaded into the reaction chamber to collect a baseline spectrum in the range between 1000 and 200 nm. To elucidate the change of vanadium environment due to adsorption of water, the experiments have been done after one step of pretreatment under the flow of 5 ml/min

O₂/He 21/79 for 15 min at 450 °C and 350 °C for K₂V₈O₂₁ and K₃V₅O₁₄, respectively. The temperature dependent UV-Vis data were collected from a Cary 500 in-situ cell (Agilent) with the flow of gas from the top to the bottom of the reaction chamber. The temperature was raised with a rate of 5 Kpm.

Raman spectroscopy

Raman measurements were conducted applying a 532 nm, 50 mW DPSS Laser (Cobolt 05-01 series) and a TriVista Raman Microscope System (TriVista TR 557, S&I GmbH) equipped with a CCD camera (Spec10: 100BR, Princeton Instruments) applying the 10X Objective and a laser power of 2 mW at catalyst position. For spectrometer frequency calibration a silicon wafer ($520.7 \pm 0.5 \text{ cm}^{-1}$) was applied. The in-situ reaction cell was a CCR 1000 cell from Linkam with the feed flowing from the top to the bottom of the chamber. The temperature dependent experiments have been performed after dehydration under the flow of 5 ml/min O₂/He 21/79 at 450 °C and 350 °C for K₂V₈O₂₁ and K₃V₅O₁₄, respectively. The Linkam cell was modified to accurately measure the temperature close to the surface of the catalyst sample by installing a second thermocouple.

Computational details

The crystal structures of K₂V₈O₂₁ (154164.cif¹⁵) and K₃V₅O₁₄ (248227.cif¹⁶) were obtained from the Inorganic Crystal Structure Database (ICSD, website: <http://icsd.fkf.mpg.de/>). Their space groups are *C2/m* (No. 12) and *P31m* (No. 157), respectively. The number of Raman active phonon modes is determined according to the analysis of Bilbao crystallographic server (website: <http://www.cryst.ehu.es/>).¹⁷⁻²⁰ Phonon calculation was performed in Quantum Espresso 5.4.0²¹ to obtain vibrational frequency, infrared and Raman activity. The input structure was obtained after variable cell relaxation calculation using primitive cell coordinate as the initial guess. It was carried out using local density approximation (LDA) functional and norm-conserving pseudopotentials. The plane wave kinetic energy cut off values of 150 Ry and 600 Ry were adopted for K₂V₈O₂₁ for the wave functions and the charge densities, respectively. For K₃V₅O₁₄ the values of 140 Ry and 560 Ry were applied. The Monkhorst-Pack type of k-point sampling with a 4×4×2 and 2×2×4 were chosen for K₂V₈O₂₁ and K₃V₅O₁₄, correspondingly.²²

2.3 Results

2.3.1 Synthesis

The results of XRD measurements confirm that the prepared $K_2V_8O_{21}$ and $K_3V_5O_{14}$ are phase-pure, see Figure 2.1. V/K molar ratio measured applying XRF gives the number of 3.97 for $K_2V_8O_{21}$ and 1.64 for $K_3V_5O_{14}$ which are comparable with the V/K stoichiometric ratios of 4 and 1.67 in the compounds.

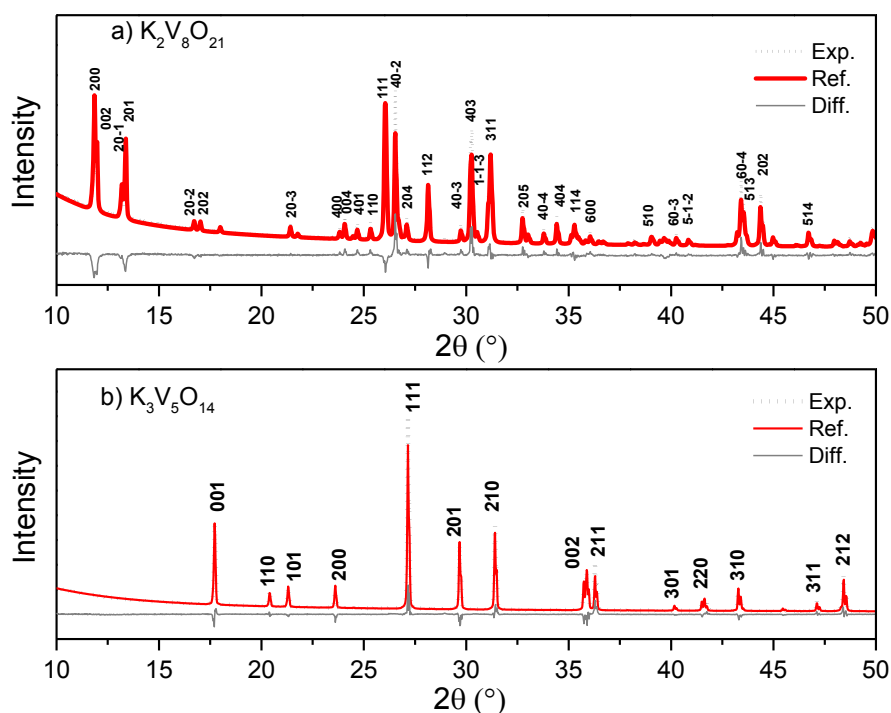


Figure 2.1. XRD patterns and Rietveld refinements of a) $K_2V_8O_{21}$ and b) $K_3V_5O_{14}$.

The crystalline structure of $K_2V_8O_{21}$ belongs to the monoclinic space group $C2/m$ with the unit cell parameters listed in Table 1, being in agreement with literature⁵. In the structure of $K_2V_8O_{21}$, shown in Figure 2.2, VO_6 octahedra and VO_5 pyramids form $[V_8O_{21}]^{2-}$ units running along the b-axis. Three different types of columns can be seen in the structure: Type I columns are two VO_5 pyramids sharing edges. Type II columns consist of four distorted edge-sharing VO_6 octahedra, and type III is a single chain of VO_5 pyramids. The K ions are found in the formed tunnels⁵.

The crystal structure of $K_3V_5O_{14}$ belongs to the $P31m$ space group with the unit cell parameters shown in Table 1. The layered structure of $K_3V_5O_{14}$ consists of TTB-like sheets

corner-sharing VO_4 tetrahedra and VO_5 square pyramids, see Figure 3.⁸ The 14 oxygen atoms form roughly trigonal pyramids around the V1 atoms and square pyramids around the V2 atoms. The pyramids are corner linked with apices pointing in the same direction along the c-axis. Each empty space resulting from the five-ring configuration of vanadium is filled by a potassium atom. The K atom is sitting in the middle of two layers, which fit well on the V_5O_{14} layer, and is surrounded by 10 oxygens, five from the apex oxygens of the polyhedra in the layer below and five from the basal corner of polyhedra in the upper layer.^{10 9}

Table 2.1. Crystal data for prepared $\text{K}_2\text{V}_8\text{O}_{21}$ and $\text{K}_3\text{V}_5\text{O}_{14}$

	$\text{K}_2\text{V}_8\text{O}_{21}$	$\text{K}_3\text{V}_5\text{O}_{14}$
Unit cell parameters (Å)	$a=14.9470$	$a=8.695$
	$b=3.618$	$b=8.697$
	$c=14.783$	$c=4.999$
	$\beta=91.029^\circ$	$\alpha=90.0^\circ$
		$\beta=90.0^\circ$
		$\gamma=120.0^\circ$
Space group	$C2/m$	$P31m$
BET	1.5	1.2
V/K^a	4	1.67
V/K^b	3.97	1.64
V/K^c	4.2	1.2
O/V^a	2.62	2.8
O/V^c	2.9	2.9

a) Theoretical b) XRF c) XPS

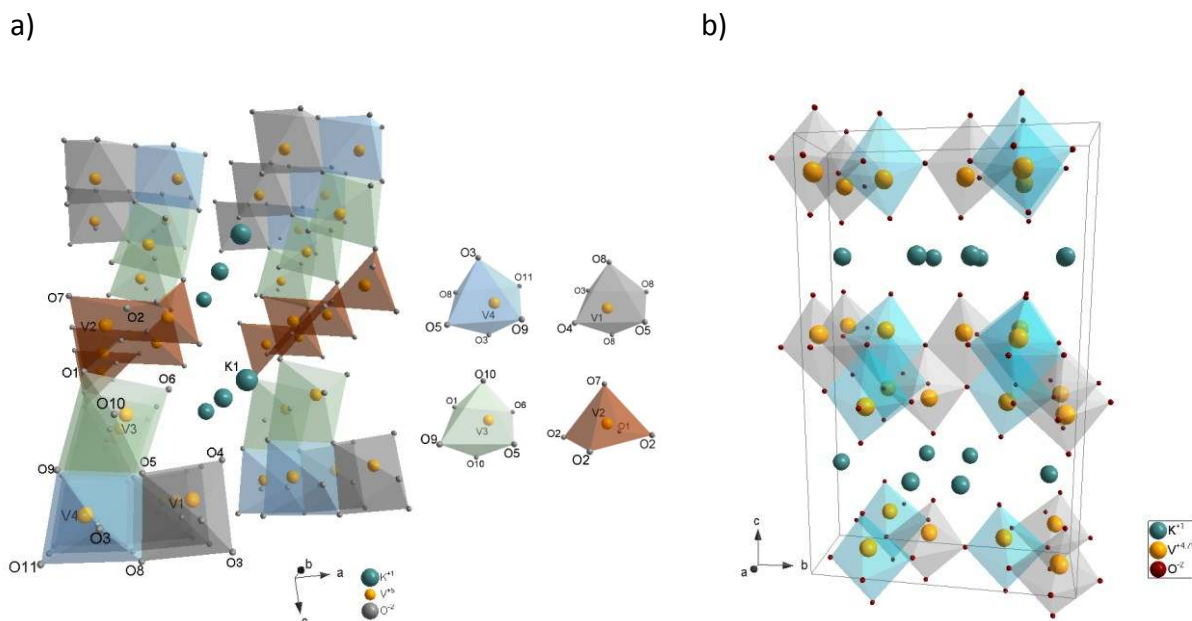


Figure 2.2. Polyhedral diagram of a) $K_2V_8O_{21}$ viewed along the b axis, b) $K_{0.5}V_2O_5$ viewed along the a axis.

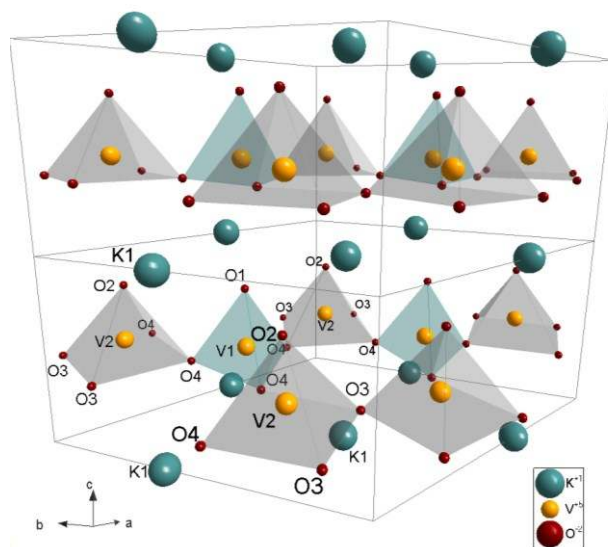


Figure 2.3. Polyhedral diagram of $K_3V_5O_{14}$.

In the XPS spectrum of $K_2V_8O_{21}$ and $K_3V_5O_{14}$, see Figure S 2.1 and S 2.2, all core levels appear to contain one species. The V2p(3/2) is narrow and symmetric, suggesting V^{5+} , in line with the V formal oxidation state of these phases. When the core levels are adjusted according to the O1s binding energy of 530 eV (lattice O of binary V oxides), the V2p(3/2) binding energy is near 517.1 eV, which also fits to V^{5+} . Measuring the separation of the O1s–V2p(3/2) peaks and estimating the V oxidation state based on this²³, also gives oxidation state of +5 for vanadium. The K2p spectra appear also as a single doublet (3/2 and 1/2). The V/K ratio

calculated by XPS analysis for $K_2V_8O_{21}$ is 4.2, close to the nominal value of 4, see Table 1. Thus, this sample has roughly the stoichiometric K content on the surface or very slightly less. The O/V ratio seems to be relatively reasonable for both samples. Regarding $K_3V_5O_{14}$, the V/K ratio of 1.2, calculated by XPS, confirms potassium enrichment on the surface of sample.

Thermal analysis performed by DSC with 10 Kpm heating rate and 5 Kpm cooling rate under O_2/Ar 21/79, see Figure 2.5, confirmed that $K_2V_8O_{21}$ and $K_3V_5O_{14}$ melt at 520 °C and 413 °C, respectively. The narrow melting peaks present in the DSC analysis are further proof for phase purity.

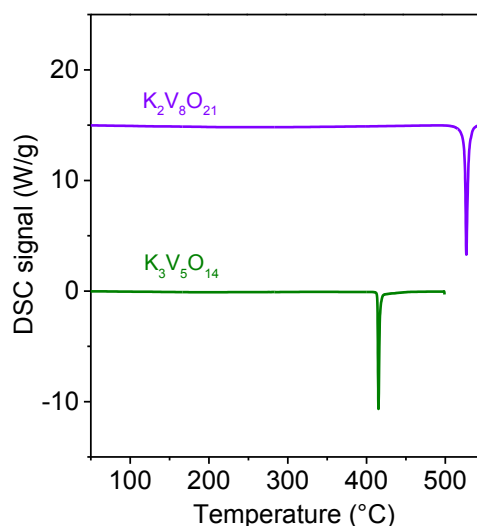


Figure 2.4. DSC of $K_2V_8O_{21}$ and $K_3V_5O_{14}$ under 70 ml/min O_2/Ar 21/79, heating rate: 10 Kpm.

2.3.2 Raman and IR spectra at ambient temperature

According to the analysis of Bilbao crystallographic server (website: <http://www.cryst.ehu.es/>)¹⁷⁻²⁰, $K_2V_8O_{21}$ has 45 IR active phonon modes ($\Gamma_{IR} = 15A_u + 30B_u$) and 45 Raman active phonon modes ($\Gamma_{Raman} = 30A_g + 15B_g$). For $K_3V_5O_{14}$ there are 33 IR active phonon modes ($\Gamma_{IR} = 12A_1 + 21E$) and 33 Raman active phonon modes ($\Gamma_{Raman} = 12A_1 + 21E$). Calculated Raman and IR active modes accompanied by their assignments are listed in Table S 2.3 and Table S 2.4. The optimized primitive cells applied for the calculations are shown in Figure S 2.3.

ATR-IR spectroscopy

The ATR-IR spectrum of $K_2V_8O_{21}$ is depicted in Figure 2.5. Based on DFT calculations, the bands around 1000 cm^{-1} are assigned to V=O stretching in polyhedral structures. Due to presence of different types of polyhedra in the structure of $K_2V_8O_{21}$, which gives rise to the presence of different V-O terminal bonds (V1-O4, V2-O7, V3-O6, V4-O9), this band is split and covers the interval of $940\text{--}1008\text{ cm}^{-1}$. The peaks between $650\text{--}900\text{ cm}^{-1}$ are mainly attributed to stretching vibrations of longer bonds. The bending mode is present at 623 cm^{-1} .

In the ATR-IR spectrum of $K_3V_5O_{14}$, see Figure 2.6, similarities of vibrational modes with those of $K_2V_8O_{21}$ are visible. The peaks at 977 and 956 cm^{-1} , due to stretching modes of V=O short bands, and the peaks in the interval of $850\text{--}950\text{ cm}^{-1}$, assigned to stretching of longer bonds such as V2-O4, are detectable. Moreover, the broad bands below 800 cm^{-1} originating from bending modes are clearly present.

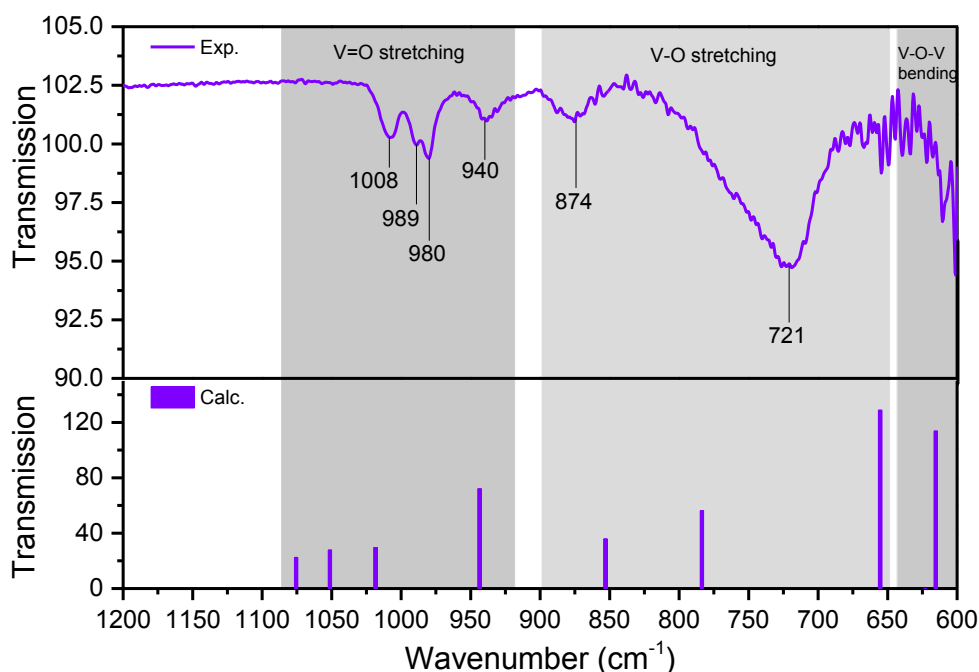


Figure 2.5. Room temperature ATR-IR of $K_2V_8O_{21}$ accompanied by calculated IR active vibrational modes (Calc.). General vibrational assignments from DFT calculations are indicated.

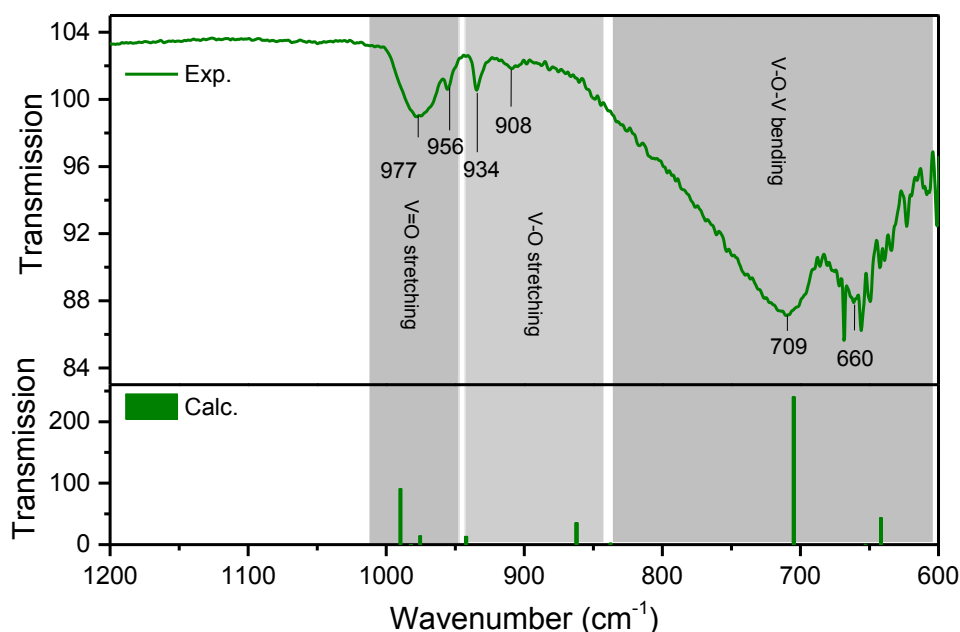


Figure 2.6. Room temperature ATR-IR of $K_3V_5O_{14}$ accompanied by calculated IR active vibrational modes (Calc.). General vibrational assignments from DFT calculations are indicated.

Raman spectroscopy

Figure 2.7 and Figure 2.8 show the Raman spectra of the two phases measured at room temperature. The number of modes predicted by group theory is remarkably higher than experimentally observed ones. This is due to small polarizability derivatives for many Raman active modes. Moreover, there are components, for instance B_g modes and A_g modes, which almost coincide.

The room temperature Raman spectrum of $K_2V_8O_{21}$ has been previously recorded by Krasil'nikov et al. ⁶ In a similar fashion, a relatively intense background is present in the spectrum, see Figure 2.7. As a result of presence of broad peaks in the Raman spectrum, several calculated modes could be assigned to each peak. Due to complexity of the system, it is difficult to assign all the observed bands decidedly.

Herein, DFT calculation, presented in Figure 2.7, results in following assignments which are partly visualized applying Eigenmode plots in Figure S 2.4. The Raman bands at 1007 and 988 cm^{-1} originate from the stretching vibration of V-O short bonds (V1-O4, V2-O7, V3-O6, V4-O9) with the length of 1.58-1.63 Å, which can be considered as V=O vanadyl groups. The

Band at 938 cm^{-1} is assigned to vibration of V-O bands with the length of $\sim 1.6\text{ \AA}$ (V4-O9, V3-O6, V1-O4). The relatively sharp bands between $700\text{--}800\text{ cm}^{-1}$ are characteristic for stretching vibration of V-O bridging bands like V4-O5-V1. The bands in the interval of 200 to 650 \AA are assigned to the bending modes. For instance, the ones at 560 and 623 cm^{-1} are attributed to V4-O8-V1-O3 bending and V1-O3-V4-O8-O11 bending, respectively. The peaks in the low-frequency region originate from displacement of vanadium atoms as in a reported study for other potassium vanadates²⁴. Displacement of potassium itself could also induce extra Raman modes in this low-frequency region. So far, the assignments of vibrational modes of $\text{K}_2\text{V}_8\text{O}_{21}$ in literature⁶ have been done on the basis of empirical relations for relating vanadium-oxygen bond lengths and stretching frequencies²⁵ and the existing assignments of Raman modes for other types of vanadates²⁴.

Considering the structure of $\text{K}_3\text{V}_5\text{O}_{14}$, the V-O short bonds could be compared with the V-O short bonds of V_2O_5 . In both structures, The short V-O bonds within the layer are in the range of $1.5\text{--}1.6\text{ \AA}$ and they are far from the next layer.¹³ For these short bonds, The Raman active stretching $\nu(\text{V-O})$ modes are expected around 978 cm^{-1} .²⁶ In our Raman study, these bands are clearly detected for $\text{K}_3\text{V}_5\text{O}_{14}$. The weakness of the terminal V=O stretching bands ranging from 990 to 1000 cm^{-1} could be due to potassium enrichment on the surface, as demonstrated by XPS analysis. Existence of two crystallographically inequivalent sites of V (V1 and V2) and as a result two different V-O terminal bonds with the calculated distance of 1.67 and 1.65 \AA give rise to more vibrational bands at high frequencies. Next in the frequency scale is the 889 cm^{-1} mode which is assigned to the stretching mode of V1-O4 and V2-O4 bonds. The non-centrosymmetric nature of the V1-O4-V2 bridge results in high intensity of this band in the Raman spectra when compared with V_2O_5 . The bands appearing in the region of $200\text{--}750\text{ cm}^{-1}$ with the relatively strong intensity, based on DFT calculations, are characterized as the bending vibrational modes. For instance, the one at 496 cm^{-1} is due to V1-O4-V2 bending. The Raman bands below 200 cm^{-1} are ascribed to displacements of V and K atoms. Once again due to existence of two crystallographically inequivalent sites for V (V1,V2) in the structure, more features are present in the Raman spectra of prepared samples in comparison with V_2O_5 , which has just a single type of V atom in the structure.

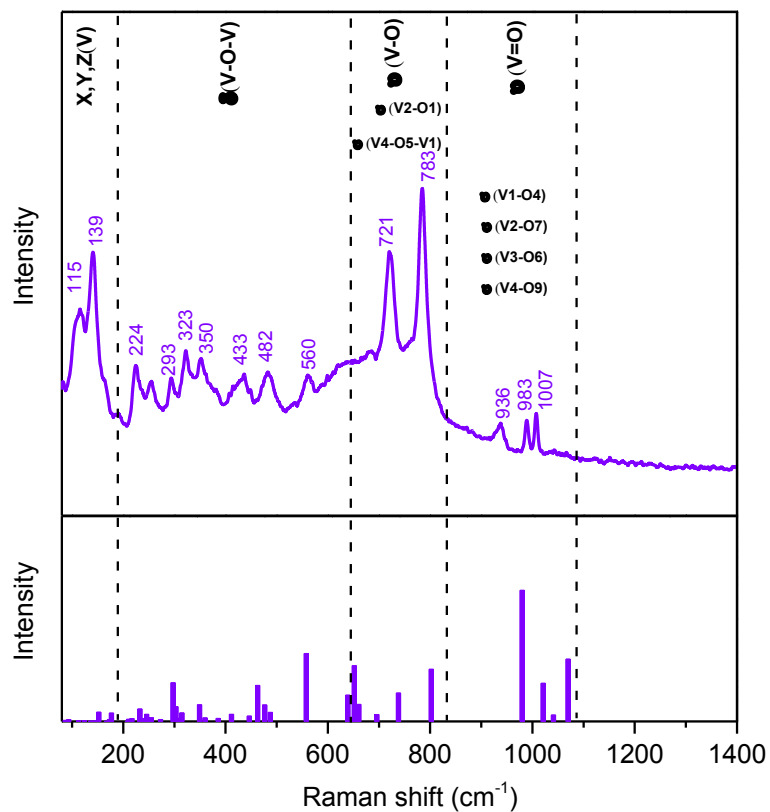


Figure 2.7. The room temperature Raman spectrum of $K_2V_8O_{21}$ accompanied by calculated Raman active vibrational modes (Calc.). General vibrational assignments from DFT calculations are indicated.

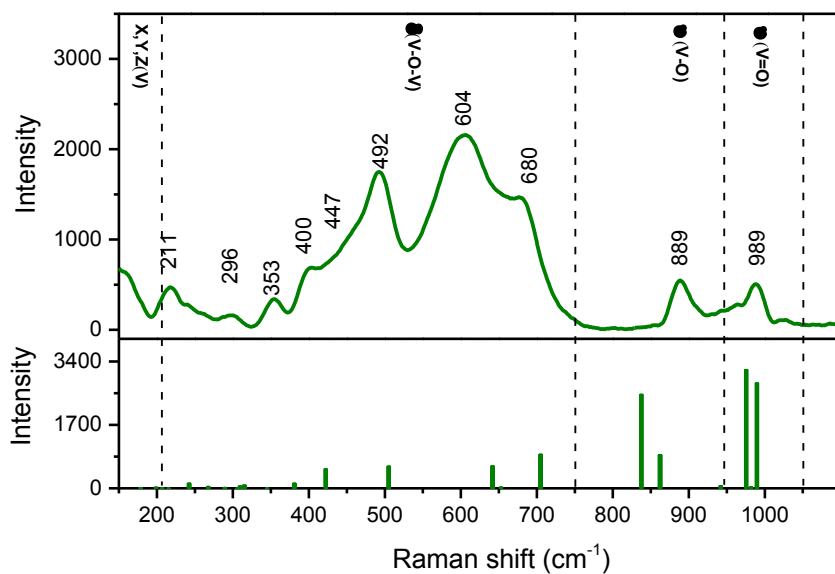


Figure 2.8. Comparison of experimental and calculated Raman spectra of $K_3V_5O_{14}$.

2.3.3 Temperature dependent Raman spectroscopy of $K_2V_8O_{21}$

Figure 2.9 displays the evolution of Raman spectra of $K_2V_8O_{21}$ after dehydration over heating up to the melting point under the flow of 5 ml/min O_2/Ar 21/79. Upon heating, wavelength red shift and noticeable band broadening initiating from thermal expansion are observed. A slight change in the relative intensity of the main bands at 784 and 720 cm^{-1} is also noticeable. The changes in the Raman spectra at temperatures lower than the melting point are usually a result of changes in the strength of existing bonds due to the temperature induced lattice expansion. As it can be seen from the enlarged spectra shown in Figure 2.9b, by increasing the temperature the vibration mode at 1056 cm^{-1} , which was barely visible at room temperature, gets more evident, while the one at 626 cm^{-1} loses intensity. The observed broad band at 1056 cm^{-1} at elevated temperatures is most likely initiating from presence of surface vanadia species.

In the flow of O_2/He 21/79, Figure S 2.7a, and also He, Figure S 2.7b, the spectra was quite stable in 480 °C over the tested period of time, 60 and 24 h for O_2/He 21/79 and He, respectively.

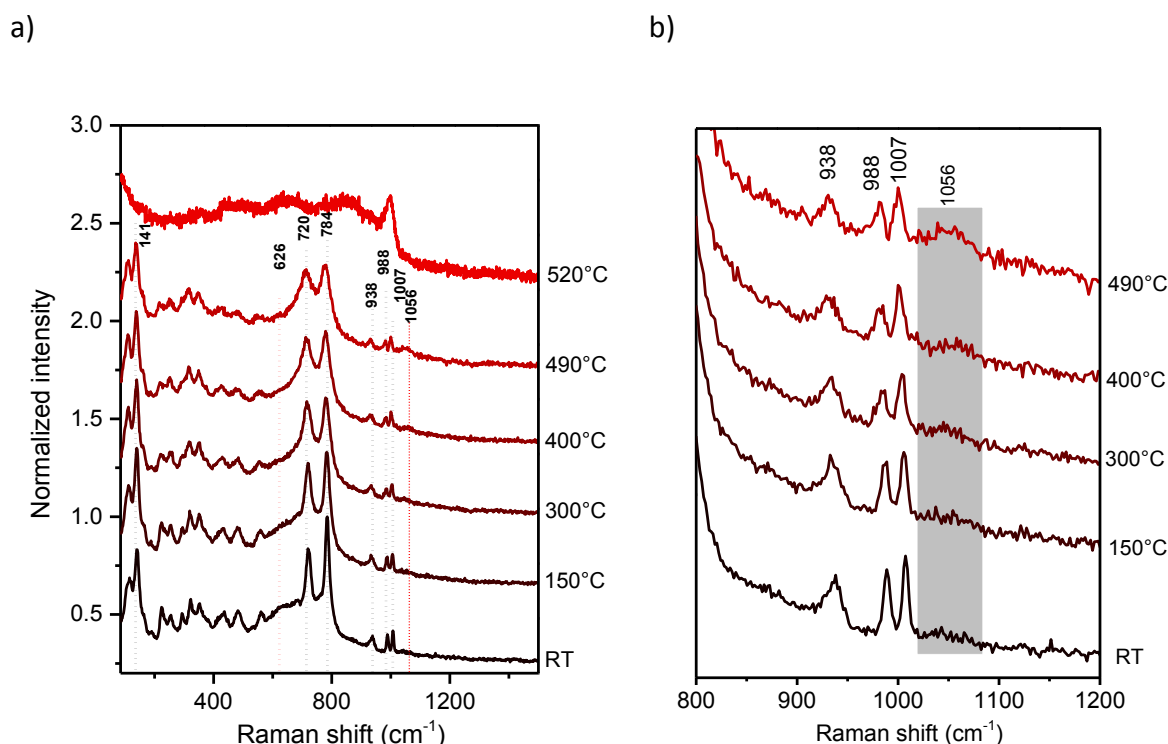


Figure 2.9. Temperature dependent Raman of $K_2V_8O_{21}$ during heating up to the melting point under the flow of 5 ml/min O_2/Ar 21/79, a) spectra from room temperature to 520 °C, normalized to (0-1), b) enlargement of vibrational modes at higher Raman shifts.

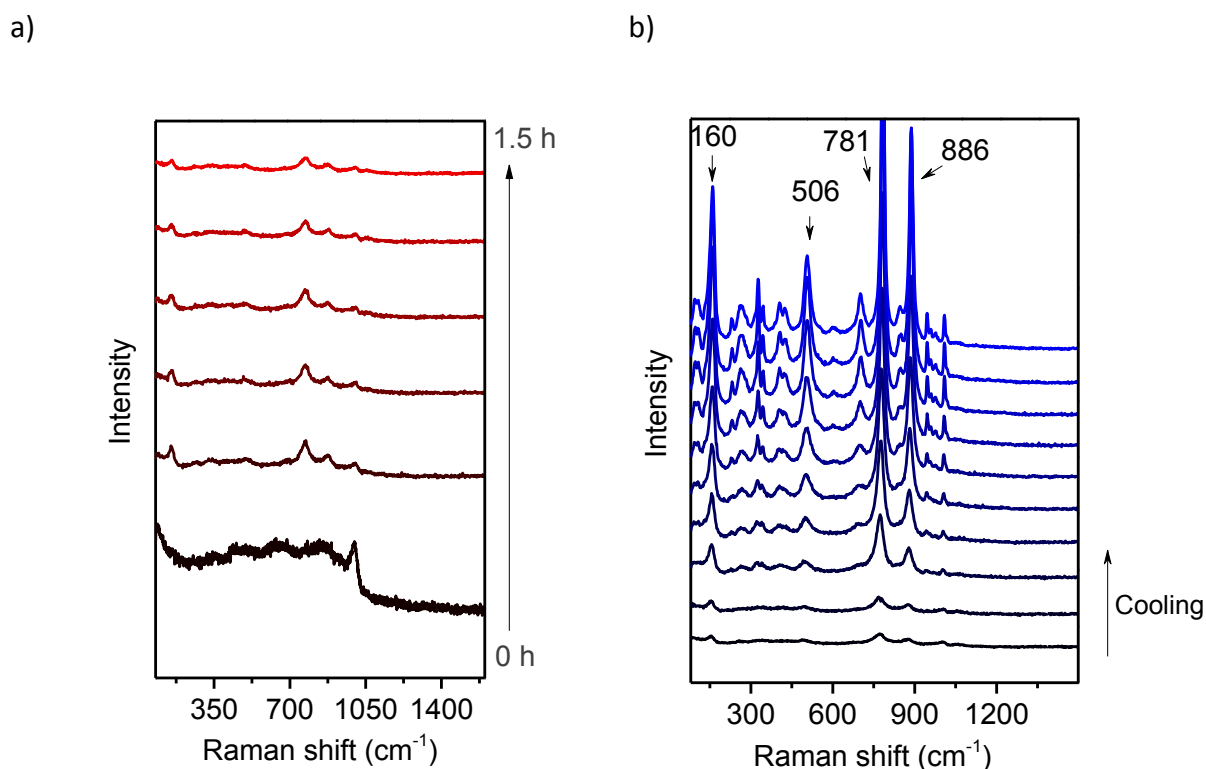


Figure 2.10. Raman spectroscopy of $K_2V_8O_{21}$ after reaching the melting point a) holding in the molten state b) via cooling in the in-situ cell.

By reaching the melting point, a clear loss in intensity of bands is noticeable, see Figure 2.9a. The band at 998 cm^{-1} is the only one which is clearly detectable. The transformation of the molten $K_2V_8O_{21}$ to the $K_{0.5}V_2O_5$ phase in O_2/He 21/79 atmosphere was monitored via in situ Raman spectroscopy as a function of time as shown in Figure 2.10a. Characteristic bands at 160 , 781 , and 886 cm^{-1} related to vibrational modes in $K_{0.5}V_2O_5$ ²⁴ could be clearly observed immediately upon holding in the molten state. $K_2V_8O_{21}$ was quite unstable in the molten state and a fast phase transition was noticeable.

The $K_2V_8O_{21}$ Raman signal is essentially absent in the spectra taken during cooling in the in-situ cell due to complete transformation to the $K_{0.5}V_2O_5$ phase, and the corresponding Raman signals for the $K_{0.5}V_2O_5$ phase are clearly observed via cooling and eventually at room temperature. The intense Raman features at 781 and 886 cm^{-1} , which correspond to the stretching vibrations of strongly asymmetric V-O-V bridges in the double-layer structure of $K_{0.5}V_2O_5$ ²⁴, are distinguishable after reduction of $K_2V_8O_{21}$ and change in arrangement and type of polyhedra via formation of $K_{0.5}V_2O_5$, see Figure 2.2b.

The transformation of the $K_2V_8O_{21}$ to $K_{0.5}V_2O_5$ phase was also confirmed applying XRD analysis of the sample after cooling in the in-situ cell. A comparison of XRD patterns of $K_2V_8O_{21}$ and $K_{0.5}V_2O_5$ which formed after cooling is shown in Figure 2.11. The present shift in the position of peaks in the XRD of the sample after high temperature Raman, when compared with $K_{0.5}V_2O_5$, could be due to presence of variable amount of K in the interlayer or partially hydrated state of a formed potassium vanadate phase.²⁷

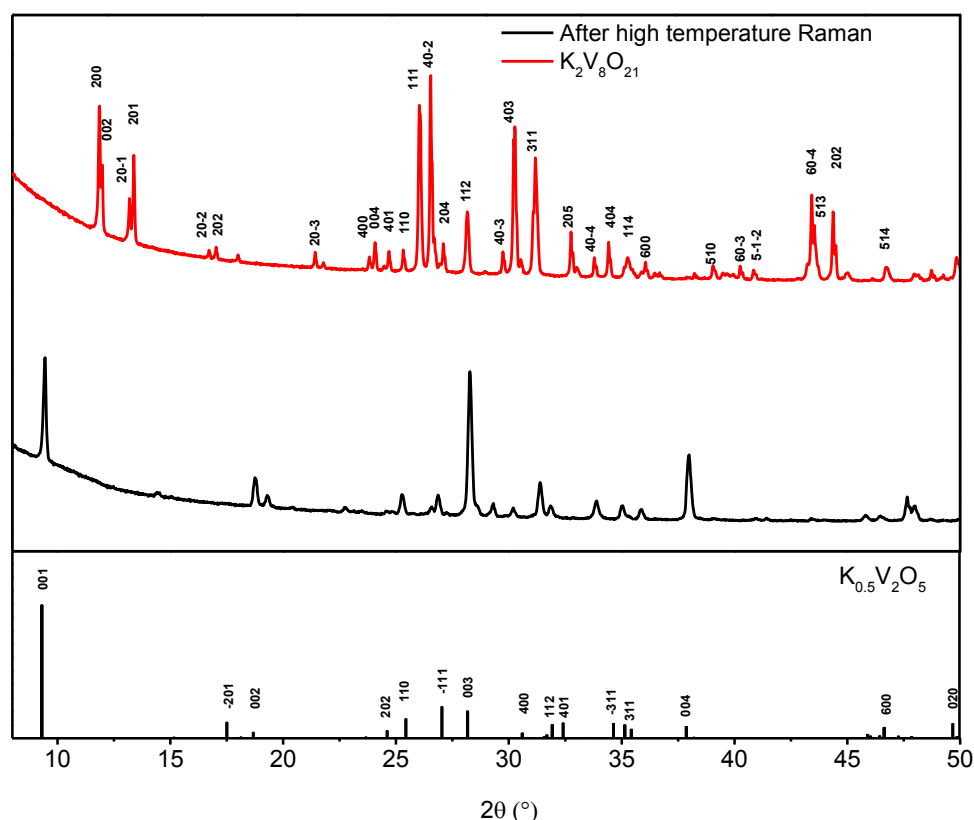


Figure 2.11. Comparison of XRD of $K_2V_8O_{21}$ with the sample after high temperature Raman analysis.

2.3.4 Temperature dependent Raman spectroscopy of $K_3V_5O_{14}$

Figure 2.12 shows the temperature dependent Raman spectra of $K_3V_5O_{14}$ while heating under 21 % O_2 in Ar from room temperature to above the melting point. The spectra at different temperatures were taken after stabilization of the temperature. Due to the high level of beam sensitivity the number of taken spectra was minimized. Considering the increase of the 678 cm^{-1} feature relative to the 607 cm^{-1} one as a function of temperature,

it appears that the structure of $K_3V_5O_{14}$ was altered during the heating before reaching the melting point. The influence of temperature on cross-section via heating, however, cannot be excluded. Beside the mentioned alteration, one extra band at around 1056 cm^{-1} is formed at higher temperatures before reaching the melting point. The mentioned band can be assigned to surface vanadium species.

By crossing the melting point a sudden change in the spectrum was noticeable. The intensity of bands with lower Raman shifts decreases and band broadening is observed. Possible reason for the observations regarding the band broadening could be larger distribution of bond angles and broadening of atomic bond distances, resulting from structural relaxation of $K_3V_5O_{14}$ above the melting point. The Raman spectrum of $K_3V_5O_{14}$ in the molten state, see Figure 2.13, can be understood by considering the destruction of layered structure of the material and bond breaking after the melting point. This, in particular, was investigated for molten V_2O_5 in the literature, where vanadia species with lower coordination number were reported as present species in the molten V_2O_5 .²⁸ In our study, elimination of layered structure of $K_3V_5O_{14}$ via losing the intensity of the bands between $400\text{-}800\text{ cm}^{-1}$, and loss of long range ordering through losing the bands below 200 cm^{-1} is quite remarkable. Creation of more V-O terminal groups in the position of broken bonds can be the reason for the observed dominant bands in the higher wavenumber regime of the Raman spectrum, $900\text{-}1000\text{ cm}^{-1}$, after reaching the melting point. The observed bands in this region merge together, which could be evidence of disordering induced after the melting point. Presence of some bridging bands are also expected after melting, being evidenced by vibrational modes at about 884 cm^{-1} in the spectra taken in the molten state. Although, elongation of terminal bonds after phase transition and as a consequence of structural relaxation is also imaginable, which could contribute to vibrational modes in this region.

The spectrum taken after cooling in the in-situ cell demonstrates recrystallization of $K_3V_5O_{14}$ via formation of all the initial bands observed in the Raman spectra of fresh catalyst, revealing stability of $K_3V_5O_{14}$ in the molten state.

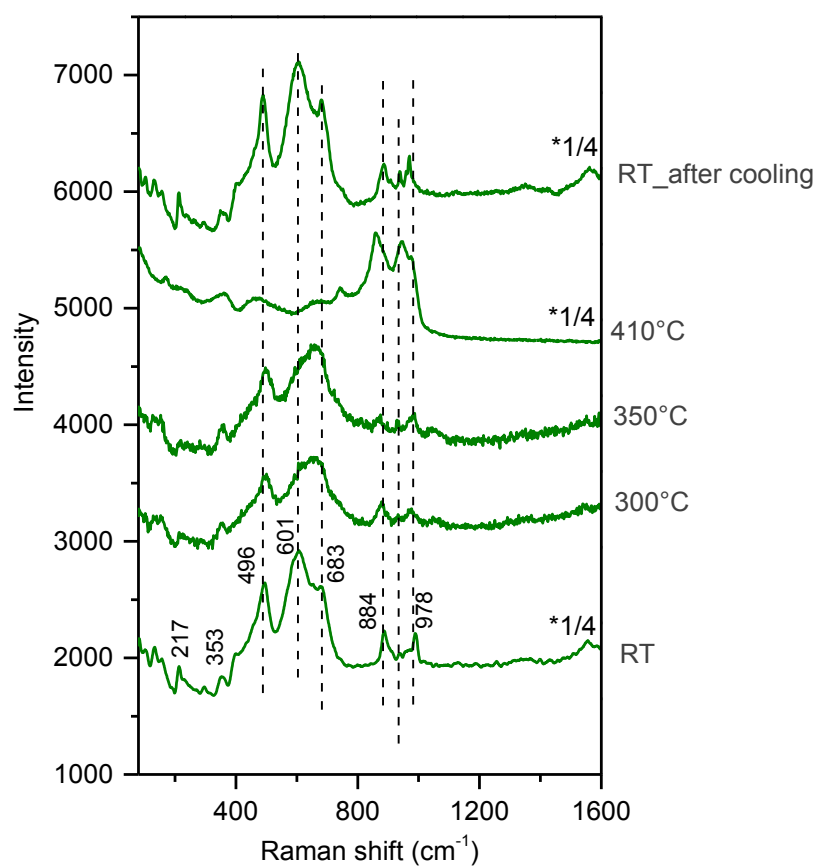


Figure 2.12. Temperature dependent Raman of $K_3V_5O_{14}$ under 5 ml/min 21%O₂ in He.

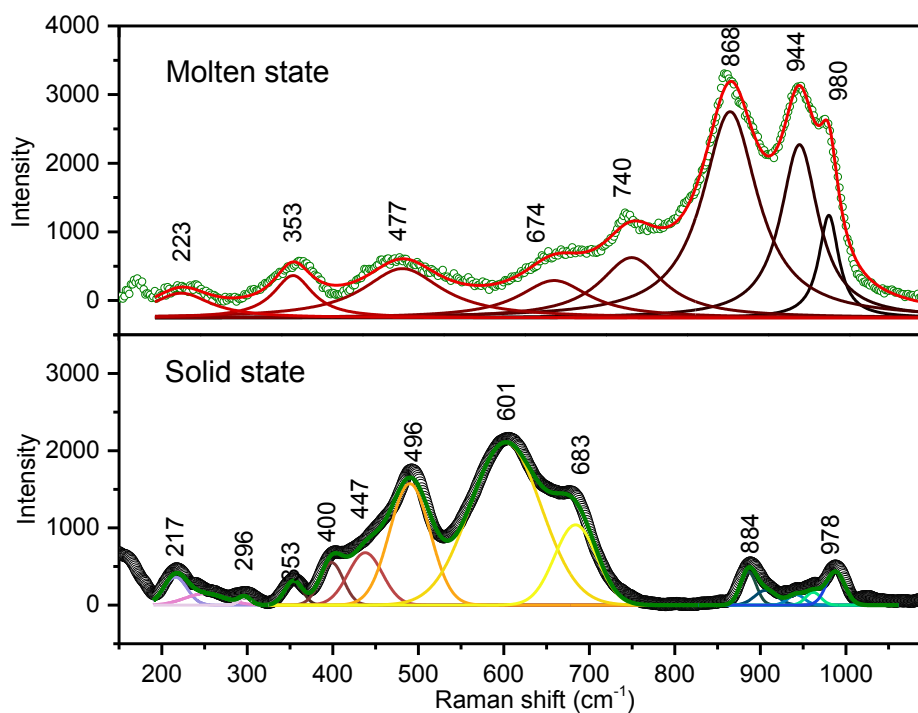


Figure 2.13. Comparison of Raman spectra of $K_3V_5O_{14}$ in the solid and molten states.

2.3.5 Temperature dependent UV-Vis spectroscopy of $K_2V_8O_{21}$

$K_2V_8O_{21}$ was pre-treated under the flow of O_2/He 21/79. The temperature was increased with a 5 K/min ramp rate and the sample was kept for 30 min at 450 °C. The room temperature UV-Vis spectrum of $K_2V_8O_{21}$ in dehydrated state is shown in Figure 2.14.

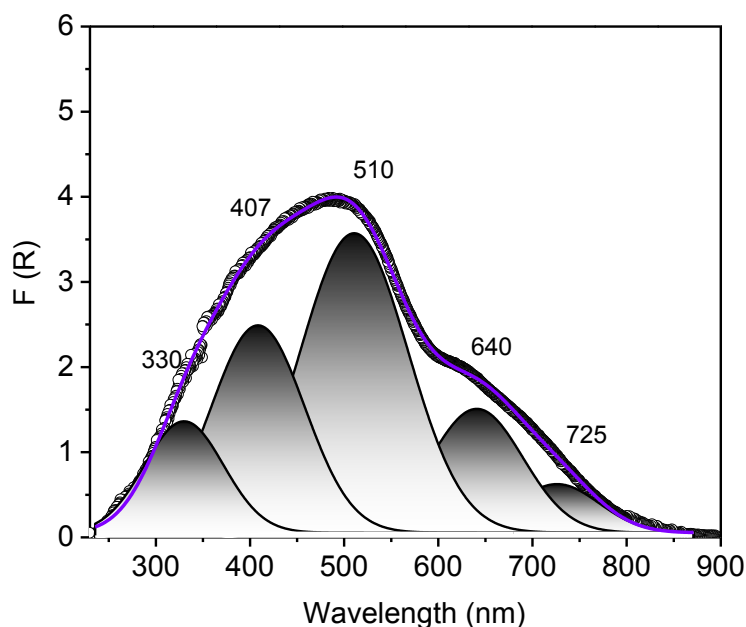


Figure 2.14. UV-Vis spectra of $K_2V_8O_{21}$ in dehydrated state.

Due to the complex structure of $K_2V_8O_{21}$, composing VO_5 and VO_6 , the UV-Vis spectrum depicts broad bands covering the whole UV-Vis region. The absorption band around 330 nm is attributed to the ligand–metal charge transfer of O^{2-} - V^{5+} , and the presence of this band also indicates polymeric V–O–V linkage.²⁹ The one at 407 nm is also initiated by the presence of polymeric species.²⁹ The band around 510 nm can originate from octahedrally environment vanadium.³⁰ The shoulder between 600–800 nm could be assigned to d-d transitions in V^{4+} ³⁰ formed already during preparation. However, some oxygen defects in the structure cannot be excluded.

Figure 2.15a displays the evolution of the absorption spectra of $K_2V_8O_{21}$ after dehydration over heating from room temperature to 500 °C in oxidizing atmosphere. An obvious jump in the adsorption band between 500–800 nm at temperatures higher than 400 °C is visible. This phenomenon happened reversibly via cooling and heating. The broad absorption band

extending to higher wavelength indicates the partial reduction of the $K_2V_8O_{21}$, giving rise to a variety of absorption bands. This is most likely associated with desorption of surface oxygen species and the formation of oxygen vacancies.

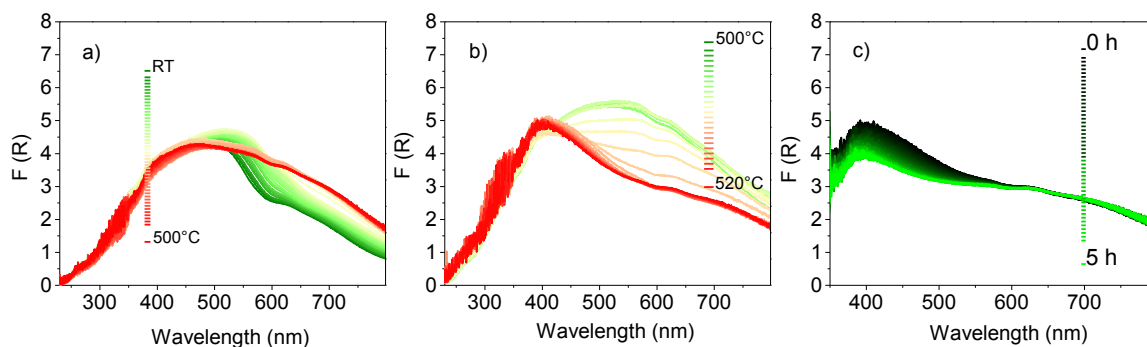


Figure 2.15. Temperature dependent UV-Vis spectra of $K_2V_8O_{21}$ under the flow of O_2/He 21/79, a) temperature dependent UV-Vis spectra of dehydrated sample from room temperature to 500 °C, b) spectra from 500 °C to the melting point, g) spectra taken at 520 °C over 5 h.

Accordingly, $K_2V_8O_{21}$ is not stable at high temperatures as was reported before by other authors.³¹ The data evolution indicates that $K_2V_8O_{21}$ changed under increased temperature. The spectra of the fresh sample after dehydration match six and five coordinated V^{5+} as expected from the structure of the sample, while the final state of the sample after cycles of heating and cooling corresponded to further formation of V^{4+} .

By reaching the melting point there is a distinct decrease in the intensity of the band around 510 nm due to vanadium in octahedral environment, Figure 2.15b. This is a sign of inducing lower coordination number for vanadium in the molten potassium vanadate.

High temperature diffuse reflectance spectra were once monitored between 200 and 800 nm as a function of time at 550 °C, Figure 2.15c. Keeping $K_2V_8O_{21}$ in the molten state demonstrated further evolution of spectra via increasing the relative intensity of the 600-800 nm band to the band at 400 nm. Considering the relative intensity, further reduction of the sample via treatment at this temperature is explainable.

This observation can be described based on the results of the Raman spectra taken in the molten state. Transformation of molten $K_2V_8O_{21}$ to $K_{0.5}V_2O_5$ is most likely the reason for the observed changes in the UV-Vis spectra of $K_2V_8O_{21}$ in the molten state.

2.3.6 Temperature dependent UV-Vis of $K_3V_5O_{14}$

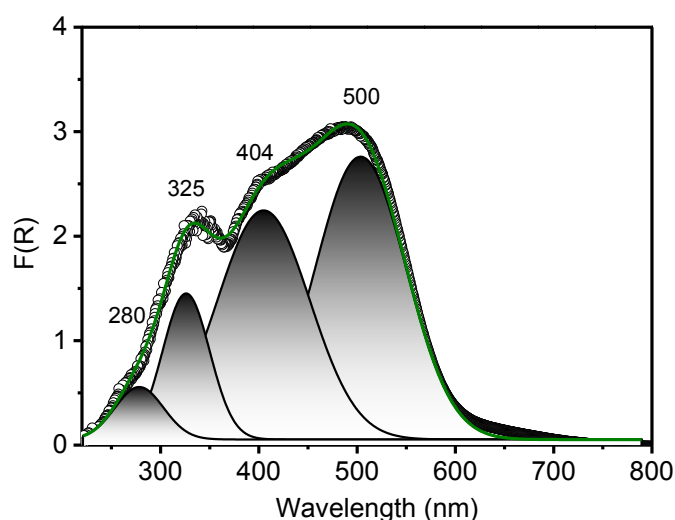


Figure 2.16. UV-Vis spectrum of $K_3V_5O_{14}$ after dehydration.

Figure 2.16 depicts the room temperature UV-Vis spectrum of $K_3V_5O_{14}$ after dehydration in 5 ml/min 21 % O_2 in Ar at 350 °C for 30 minutes. The charge transfer bands at 280 and 325 nm are attributed to vanadium in tetrahedral environment.³⁰ The absorption at 404 nm could be assigned to V-O-V bridging bonds²⁹, and the one at about 500 nm to vanadium in pseudo-octahedral coordination in agreement with the layered structure of $K_3V_5O_{14}$. A slight shoulder regarding the adsorption band in the region of 600-800 nm, related to d-d transitions of V^{4+} ³⁰ or oxygen defects, is also seen. This is most likely due to formation of a tiny amount of reduced vanadium species during synthesis.

Figure 2.17 shows the subsequential set of spectra in Kubelka-Munk units while heating from room temperature to melting point a second time after dehydration. The subsequential data progress is shown from blue to red. Apart from a gradual change of the band gap via heating, a sudden development of the band at 600-800 nm, which was observed for $K_2V_8O_{21}$, is not noticeable here, suggesting that $K_3V_5O_{14}$ remains stable in the solid state under the applied conditions.

By reaching the melting point, the intensity of the spectra between 400-600 nm is decreasing, the decrease being more pronounced for the octahedrally coordinated vanadium at around 500 nm. This observation can be explained by losing the layered structure of $K_3V_5O_{14}$ in the molten state. The decrease in intensity of the band around 400

nm is associated with partial breaking of bridging bands. Unfortunately, due to immediate agglomeration of particles after the melting point, the spectrum was completely lost and it was not possible to follow the melting behavior in detail applying UV-Vis spectroscopy. In-situ Raman, as a method that allows further focusing during experiment, seems to be a better method for this purpose as observed in section 2.3.4. Besides, deposition of a layer of $K_3V_5O_{14}$ on the surface of an inert support could be a solution for this problem, which will be explained in Chapter 3.

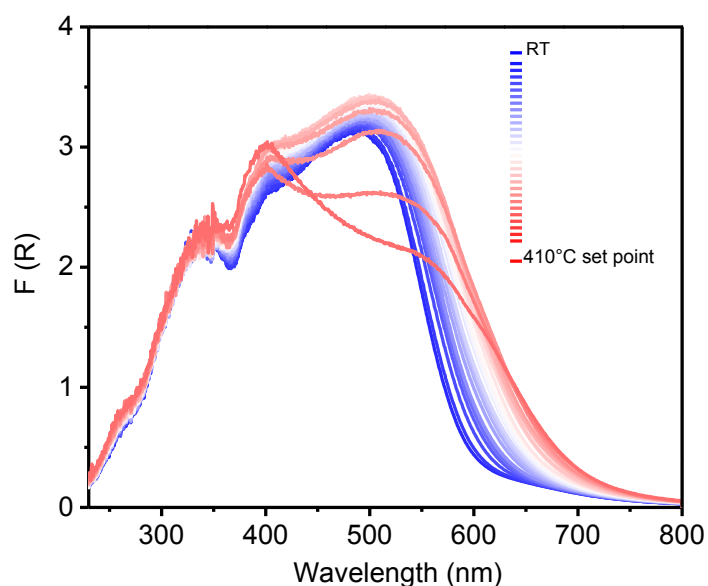


Figure 2.17. Temperature dependent UV-Vis spectroscopy of $K_3V_5O_{14}$ under 5 ml/min 21% O_2 in He.

2.4 Discussion

The conducted study with the focus on temperature dependent Raman and UV-Vis spectroscopy of $K_2V_8O_{21}$ and $K_3V_5O_{14}$ gave an insight into the terms of stability of this material at elevated temperatures. $K_2V_8O_{21}$ at higher temperatures before the melting point shows slight reduction which is revealed by high temperature UV-Vis spectroscopy. This is in agreement with literature reports noticing the formation of V^{4+} after heat treatment above 450 °C.³¹ Partial reduction of $K_2V_8O_{21}$ in the solid state is associated with the alteration of unit cell parameters and perfectly distinguishable color change and also turn of morphology⁶. A previous comparison study applying IR spectroscopy for both $K_2V_8O_{21}$ and partially reduced $K_2V_8O_{21}$ has proven that the reduced state of vanadium bronze has chains

of VO_6 in its crystal structure.⁶ The induced reduction becomes quite pronounced after the melting point under the applied atmosphere. Regarding the Raman spectrum of $\text{K}_2\text{V}_8\text{O}_{21}$ after melting, which corresponds to $\text{K}_{0.5}\text{V}_2\text{O}_5$, layers of VO_6 in the structure, could give rise to the stretching mode of V-O-V bridges observed at 886 cm^{-1} . Moreover, the increase in the intensity of the band at 502 cm^{-1} is associated with stretching vibrations of V-O bonds which get sharper after the polarization of VO_6 .

On the other hand, $\text{K}_3\text{V}_5\text{O}_{14}$ was rather stable and exhibited reversible melting and crystallization. Based on the spectral features of molten $\text{K}_3\text{V}_5\text{O}_{14}$, the local structure of vanadium in the liquid state can be proposed. Units of vanadium with lower coordination number, like tetrahedrally environment vanadium, which are partially corner linked, are conceivable.

Considering the behavior of $\text{K}_3\text{V}_5\text{O}_{14}$ and $\text{K}_2\text{V}_8\text{O}_{21}$ at high temperatures, it is evident that the materials with layered structure like $\text{K}_3\text{V}_5\text{O}_{14}$ or $\text{K}_{0.5}\text{V}_2\text{O}_5$ are more stable. One possible reason for this observation could be that the layered structure can offer a better position for potassium (between two layers) which prevents cleavage of V-O bonds in the structure of potassium vanadates via heating.

2.5 Conclusion

Herein a data set as a finger print for $\text{K}_2\text{V}_8\text{O}_{21}$ and $\text{K}_3\text{V}_5\text{O}_{14}$ has been created. Temperature dependent Raman and UV-Vis spectroscopy provide information for further high temperature application of this material. A partially reduced state of $\text{K}_2\text{V}_8\text{O}_{21}$ is characterized by an increased absorption in the low-frequency region of the UV-Vis spectra, brought about by the explained change of spectra at higher temperatures. This information is not clearly blurred in the Raman spectra of $\text{K}_2\text{V}_8\text{O}_{21}$ taken under increased temperature. $\text{K}_2\text{V}_8\text{O}_{21}$ was not stable in the molten state under the applied conditions (flow of 21 % O_2 in Ar) which could be the reason for the necessity of high oxygen pressure for preparation of this phase at high temperatures. Transformation of molten $\text{K}_2\text{V}_8\text{O}_{21}$ to $\text{K}_{0.5}\text{V}_2\text{O}_5$ was clearly detectable in the high temperature Raman cell.

$\text{K}_3\text{V}_5\text{O}_{14}$, in contrast, was quite stable in both solid and molten state under the flow of 21 % O_2 in Ar. An induced lower coordination number after phase transition from solid to liquid

and partially breaking of bridging bonds is imaginable taking all the results regarding temperature dependent Raman, temperature dependent UV-Vis spectroscopy and band assignment obtained by PFD calculations into consideration. Owing lower coordination number for vanadium sites makes the $K_3V_5O_{14}$, which is stable in the molten state, interesting for catalysis related application with respect to preparation of supported liquid phase catalysts.

Acknowledgments

This research was conducted in the framework of the BasCat, collaboration between BASF SE, TU Berlin, FHI, and the cluster of excellence “Unified Concepts in Catalysis” (UniCat, www.unicat.tu-berlin.de). We thank Maike Hashagen, Jasmin Allan and Dr. Olaf Timpe for technical assistance.

2.6 Bibliography

1. F. Cavani, N. Ballarini and A. Cericola, *Catalysis Today*, 2007, **127**, 113-131.
2. T. Blasco and J. M. L. Nieto, *Appl Catal A Gen*, 1997, **157**, 117-142.
3. R. Grabowski, B. Grzybowska, K. Samson, J. Słoczyński, J. Stoch and K. Wcisło, *Appl Catal A Gen*, 1995, **125**, 129-144.
4. B. Grzybowska, P. Mekšs, R. Grabowski, K. Wcisło, Y. Barbaux and L. Gengembre, in *Studies in Surface Science and Catalysis*, eds. V. C. Corberán and S. V. Bellón, Elsevier, 1994, vol. Volume 82, pp. 151-158.
5. A. P. Tyutyunnik, V. G. Zubkov, V. N. Krasil'nikov, G. Svensson and M. J. Sayagues, *Solid State Sciences*, 2005, **7**, 37-43.
6. V. N. Krasil'nikov, L. A. Pereleyeva, I. V. Baklanova, L. Y. Buldakova and M. Y. Yanchenko, *Russ J Inorg Chem*, 2009, **54**, 1537-1542.
7. E. Ni, S. Goto, Z. Quan and N. Sonoyama, *Electrochemistry*, 2015, **83**, 902-908.
8. Y. J. Ho, K. Sang-Hwan and P. S. Halasyamani, *Inorg Chem*, 2010, **49**, 6986-6993.
9. S. P. Huang, D. S. Wu, J. Shen, W. D. Cheng, Y. Z. Lan, F. F. Li, H. Zhang and Y. J. Gong, *J. Phys.-Condes. Matter*, 2006, **18**, 5535-5544.
10. G. Li, G. Su, X. Zhuang, Z. Li and Y. He, *Optical Materials*, 2004, **27**, 539-542.
11. H. T. Evans and A. M. Brusewitz, *Acta Chemica Scandinavica*, 1994, **48**, 533-536.
12. A. M. Bystroem and H. T. j. Evans, *Acta Chemica Scandinavica*, 1959, **13**, 377-394.
13. A. M. Bystrom and H. T. Evans, *Acta Chemica Scandinavica*, 1959, **13**, 377-378.
14. J. J. Yeh and I. Lindau, *Atomic Data and Nuclear Data Tables*, 1985, **32**, 1-155.
15. A. P. Tyutyunnik, V. G. Zubkov, V. N. Krasil'nikov, G. Svensson and M. J. Sayagués, *Solid State Sci*, 2005, **7**, 37-43.
16. J. Yeon, S.-H. Kim and P. S. Halasyamani, *Inorganic Chemistry*, 2010, **49**, 6986-6993.

17. E. Kroumova, M. I. Aroyo, J. M. Perez-Mato, A. Kirov, C. Capillas, S. Ivantchev and H. Wondratschek, *Phase Transit*, 2003, **76**, 155-170.
18. M. I. Aroyo, J. M. Perez-Mato, D. Orobengoa, E. Tasci, G. de la Flor and A. Kirov, *Bulgarian Chemical Communications*, 2011, **43**, 183-197.
19. I. Aroyo Mois, M. Perez-Mato Juan, C. Capillas, E. Kroumova, S. Ivantchev, G. Madariaga, A. Kirov and H. Wondratschek, in *Zeitschrift für Kristallographie - Crystalline Materials*, 2006, vol. 221, p. 15.
20. M. I. Aroyo, A. Kirov, C. Capillas, J. M. Perez-Mato and H. Wondratschek, *Acta Crystallographica Section A*, 2006, **62**, 115-128.
21. G. Paolo, B. Stefano, B. Nicola, C. Matteo, C. Roberto, C. Carlo, C. Davide, L. C. Guido, C. Matteo, D. Ismaila, C. Andrea Dal, G. Stefano de, F. Stefano, F. Guido, G. Ralph, G. Uwe, G. Christos, K. Anton, L. Michele, M.-S. Layla, M. Nicola, M. Francesco, M. Riccardo, P. Stefano, P. Alfredo, P. Lorenzo, S. Carlo, S. Sandro, S. Gabriele, P. S. Ari, S. Alexander, U. Paolo and M. W. Renata, *Journal of Physics: Condensed Matter*, 2009, **21**, 395502.
22. H. J. Monkhorst and J. D. Pack, *Physical Review B*, 1976, **13**, 5188-5192.
23. G. W. Coulston, E. A. Thompson and N. Herron, *Journal of Catalysis*, 1996, **163**, 122-129.
24. R. Baddour-Hadjean, A. Boudaoud, S. Bach, N. Emery and J. P. Pereira-Ramos, *Inorg Chem*, 2014, **53**, 1764-1772.
25. F. D. Hardcastle and I. E. Wachs, *The Journal of Physical Chemistry*, 1991, **95**, 5031-5041.
26. R. Baddour-Hadjean, J. P. Pereira-Ramos, C. Navone and M. Smirnov, *Chemistry of Materials*, 2008, **20**, 1916-1923.
27. Y. Oka, T. Yao and N. Yamamoto, *J Mater Chem*, 1995, **5**, 1423-1426.
28. S. i. Takeda, M. Inui, Y. Kawakita, K. Maruyama, S. Tamaki, K. Sugiyama and Y. Waseda, *Physica B: Condensed Matter*, 1995, **213**, 499-501.
29. G. Centi, S. Perathoner, F. Trifiró, A. Aboukais, C. F. Aïssi and M. Guelton, *Journal of Physical Chemistry*, 1992, **96**, 2617-2629.
30. G. Catana, R. R. Rao, B. M. Weckhuysen, P. Van Der Voort, E. Vansant and R. A. Schoonheydt, *The Journal of Physical Chemistry B*, 1998, **102**, 8005-8012.
31. V. N. Krasil'nikov, L. A. Perelyaeva, I. V. Baklanova, L. Y. Buldakova and M. Y. Yanchenko, *Russ J Inorg Chem+*, 2009, **54**, 1537-1542.

2.7 Appendix

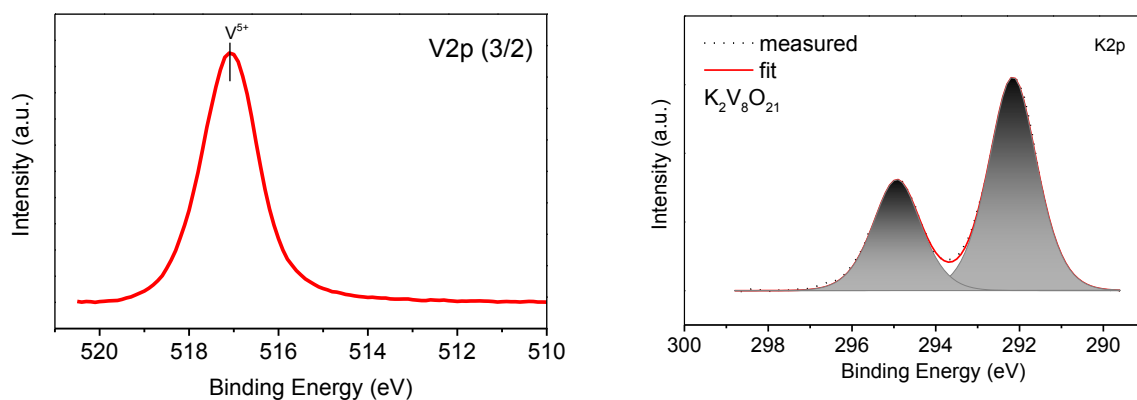


Figure S 2.1. $V2p(3/2)$ and $K2p$ core level XPS spectra of $K_2V_8O_{21}$.

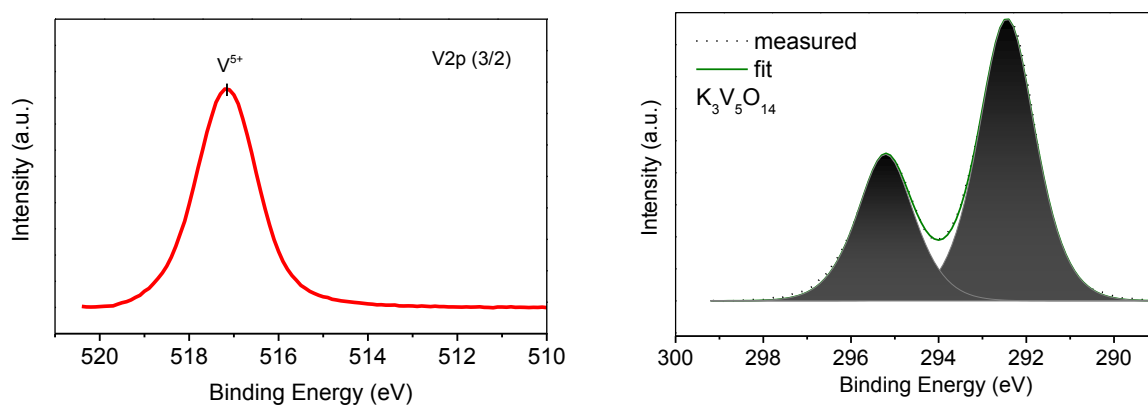


Figure S 2.2. $V2p(3/2)$ and $K2p$ core level XPS spectra of $K_3V_5O_{14}$.

V3-O1 (Å)	1.968	1.881
V3-O5 (Å)	1.932	1.962
V3-O6 (Å)	1.633	1.647
V3-O9 (Å)	2.672	2.398
V3-O10 (Å)	1.879, 1.879	1.841, 1.841
V4-O3 (Å)	1.885, 1.885	1.879, 1.879
V4-O5 (Å)	2.107	1.978
V4-O8 (Å)	2.217	2.167
V4-O9 (Å)	1.619	1.666
V4-O11 (Å)	1.786	1.793

Table S 2.2. Comparison of lattice parameters and bond lengths of $K_3V_5O_{14}$ from crystal database and calculated ones.

$K_3V_5O_{14}$	Crystal database	Calculated	Ref. ¹
a (Å)	8.697	8.674	
b (Å)	8.697	8.674	
c (Å)	4.943	4.494	
α (deg.)	90.0	90.0	
β (deg.)	90.0	90.0	
γ (deg.)	120.0	120.0	
V1-O1 (Å)	1.618	1.667	1.622
V1-O4 (Å)	1.739	1.751	1.653
V2-O2 (Å)	1.606	1.651	1.549
V2-O3 (Å)	1.824	1.818	1.858
V2-O4 (Å)	1.917	1.896	1.932

Table S 2.3. Vibrational modes assignments for $K_2V_8O_{21}$ according to phonon calculation.

Phonon modes No.	Symmetry	Calculated vibrational frequency (scaled)	IR/Raman active	Selected Assignments
4	A _u	16	I	
5	B _u	18	I	
6	B _g	53	R	
7	A _u	69	I	
8	B _u	77	I	
9	A _g	86	R	
10	B _u	88	I	
11	A _g	94	R	
12	B _g	97	R	
13	A _u	113	I	
14	A _g	116	R	
15	B _u	120	I	
16	A _g	124	R	
17	B _u	134	I	
18	B _g	137	R	
19	B _u	143	I	
20	A _g	143	R	
21	B _g	148	R	Displacement of all atoms (including K)
22	B _u	150	I	
23	A _u	152	I	
24	A _g	158	R	
25	A _g	167	R	
26	B _g	173	R	
27	B _u	177	I	
28	A _u	186	I	
29	A _u	198	I	
30	B _u	203	I	

Chapter 2

31	A_g	203	R
32	A_u	208	I
33	B_g	211	R
34	B_u	217	I
35	A_g	217	R
36	B_u	228	I
37	A_u	233	I
38	B_g	234	R
39	A_u	241	I
40	B_g	241	R
41	A_g	242	R
42	B_u	246	I
43	A_u	247	I
44	A_g	251	R
45	B_u	255	I
46	A_u	270	I
47	B_g	271	R
48	A_g	273	R
49	B_u	277	I
50	A_u	295	I
51	B_u	298	I
52	A_g	303	R
53	A_g	311	R
54	B_u	315	I
55	B_g	320	R
56	B_g	327	R
57	A_g	343	R
58	B_u	349	I
59	A_g	360	R
60	A_g	386	R
61	B_u	391	I
62	A_g	412	R

63	A_g	436	R	
64	B_u	447	I	
65	B_u	460	I	
66	A_g	462	R	
67	A_u	463	I	
68	A_g	477	R	
69	B_g	477	R	
70	B_u	487	I	
71	B_u	534	I	
72	B_u	537	I	
73	B_g	558	R	V4-O8-V1-O3 bending
74	A_u	573	I	
75	A_u	615	I	
76	A_g	623	R	V1-O3-V4-O8-O11 bending
77	A_u	639	I	
78	B_u	652	I	
79	B_g	655	R	V1-O5 stretching, V4-O11 stretching
80	A_g	661	R	
81	B_g	696	R	
82	A_g	738	R	V4-O5-V1 stretching
83	B_u	784	I	V2-O1-V3 stretching
84	A_g	802	R	V2-O1 stretching (major) V3-O6 stretching (minor)
85	B_u	853	I	V4-O11 stretching V1-O5 stretching
86	B_u	944	I	V2-O7 stretching , V1-O4 stretching, V4-O9 stretching,V3-O6 stretching
87	A_g	980	R	V4-O9 stretching V3-O6 stretching V1-O4 stretching
88	A_g	1018	R	V2-O7 stretching

				V1-O4 stretching V4-O9 stretching V3-O6 stretching.
89	B _u	1021	I	V3-O6 stretching V4-O9 stretching V2-O7 stretching
90	A _g	1041	R	V2-O7 stretching V3-O6 stretching
91	B _u	1051	I	V2-O7 stretching V1-O4 stretching V4-O9 stretching V3-O6 stretching
92	A _g	1070	R	V1-O4 stretching (major) V4-O9 stretching (minor)
93	B _u	1076	I	V2-O7 stretching (major), V1-O4 stretching (major), V4-O9 stretching (minor), V3-O6 stretching (minor)

Table S 2.4. Vibrational modes assignments of $K_3V_5O_{14}$ according to phonon calculation (acoustic modes not included).

Phonon No.	modes	Symmetry	Calculated vibrational frequency (scaled)	IR/Raman active	Selected Assignments
4, 5		E	57	I+R	
6		A ₁	58	I+R	
7		A ₂	63		
8, 9		E	81	I+R	
10		A ₂	92		
11, 12		E	96	I+R	
13, 14		E	104	I+R	
15		A ₁	105	I+R	
16		A ₁	114	I+R	

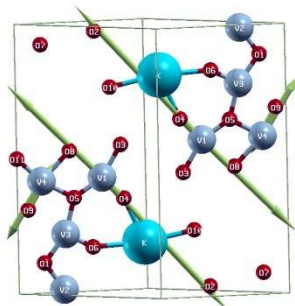
Chapter 2

17	A_2	118		
18, 19	E	128	I+R	
20, 21	E	139	I+R	
22, 23	E	149	I+R	
24	A_2	154		
25, 26	E	179	I+R	
27	A_1	199	I+R	
28, 29	E	207	I+R	
30	A_1	215	I+R	
31, 32	E	242	I+R	
33, 34	E	268	I+R	
35, 36	E	289	I+R	
37	A_1	306	I+R	
38	A_2	307		
39, 40	E	309	I+R	
41, 42	E	315	I+R	
43	A_1	345	I+R	
44, 45	E	381	I+R	
46	A_1	422	I+R	
47	A_2	437		
48, 49	E	505	I+R	V1-O4-V2 bending (mode: 48) V1-O4-V2 bending (mode: 49)
50	A_2	571		

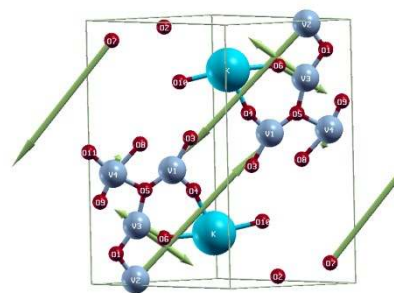
51, 52	E	642	I+R	O3-V2-O3 bending, V2-O3-V2 bending (mode: 51) O3-V2-O3 bending, V2-O3-V2 bending (mode: 52)
53	A ₁	653	I+R	
54, 55	E	705	I+R	O3-V2-O4 bending, V2-O4-V1 bending (mode: 54) O3-V2-O4 bending, V2-O4-V1 bending (mode: 55)
56	A ₂	765		
57	A ₁	838	I+R	VO ₄ tetrahedral bending, bending of V2 in V2-O3 ring
58, 59	E	862	I+R	O4-V2-O4 stretching, O4-V1-O4 stretching (mode: 58) O4-V2-O4 stretching, O4-V1-O4 stretching (mode: 59)
60, 61	E	942	I+R	VO ₄ tetrahedral and VO ₅ square pyramids stretching (mode: 60) VO ₄ tetrahedral and VO ₅ square pyramids stretching (mode: 61)
62	A ₁	975	I+R	V1-O1, V2-O2 stretching
63	A ₂	980		
64, 65	E	982	I+R	

66	A_1	990	I+R	V1-O1, V2-O2 stretching
-----------	-------	-----	-----	-------------------------

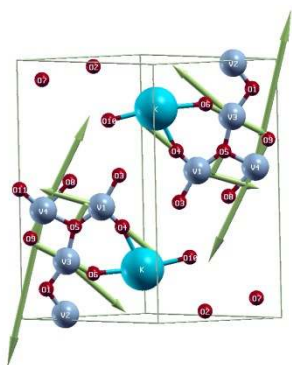
1070 cm^{-1} (mode 92), V1-O4 stretching (major), V4-O9 stretching (minor).



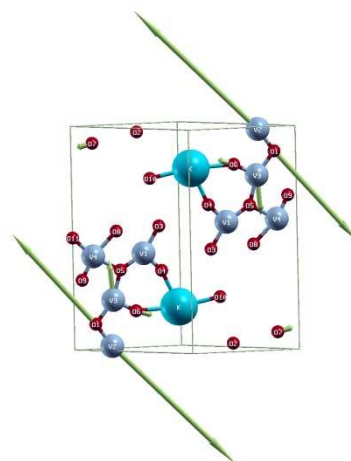
1041 cm^{-1} (mode 90), V2-O7 stretching, V3-O6 stretching



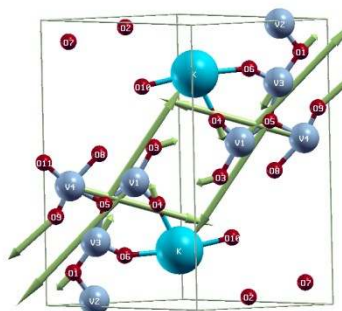
980 cm^{-1} (mode: 87): V4-O9 stretching, V3-O6 stretching, V1-O4 stretching



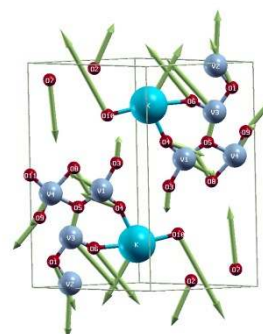
802 cm^{-1} (mode: 84): V2-O1 stretching (major), V3-O6 stretching (minor).



738 cm^{-1} (mode: 82): V1-O5 stretching, V4-



148 cm^{-1} (mode: 21): displacement of all



O9 stretching.	atoms (including K).
----------------	----------------------

Figure S 2.4. Eigenmode plots for six of the distinguished peaks in the Raman spectrum of $K_2V_8O_{21}$. Atom displacements are indicated by arrows.


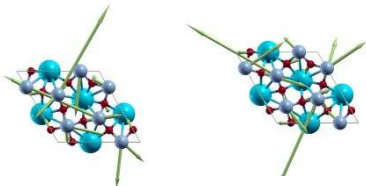
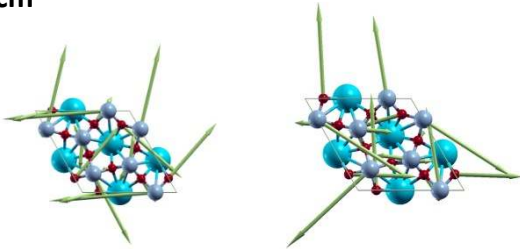
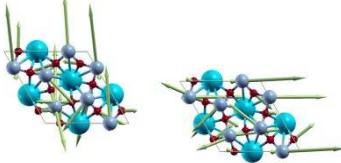
975 cm^{-1}  V1-O1, V2-O2 stretching (mode 62)	862 cm^{-1}  O4-V2-O4 stretching, O4-V1-O4 stretching (mode: 58) O4-V2-O4 stretching, O4-V1-O4 stretching (mode: 59)
642 cm^{-1}  O3-V2-O3 bending, V2-O3-V2 bending (mode: 51) O3-V2-O3 bending, V2-O3-V2 bending (mode: 52)	505 cm^{-1}  V1-O4-V2 bending (mode 48 & 49)

Figure S 2.5. Eigenmode plots for four of the distinguished peaks in the Raman spectrum of $K_3V_5O_{14}$ according to phonon calculation. Atom displacements are indicated by arrows. (Grey: vanadium, blue: potassium, red: oxygen)

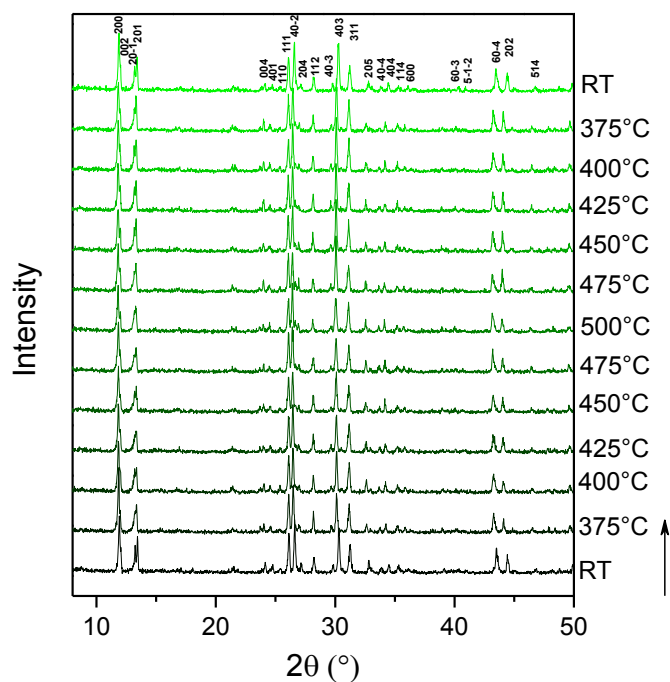


Figure S 2.6. Temperature dependent XRD under 10 ml/min O_2 in Ar (21/79). Heating rate: 10 Kpm, cooling rate: 5 Kpm.

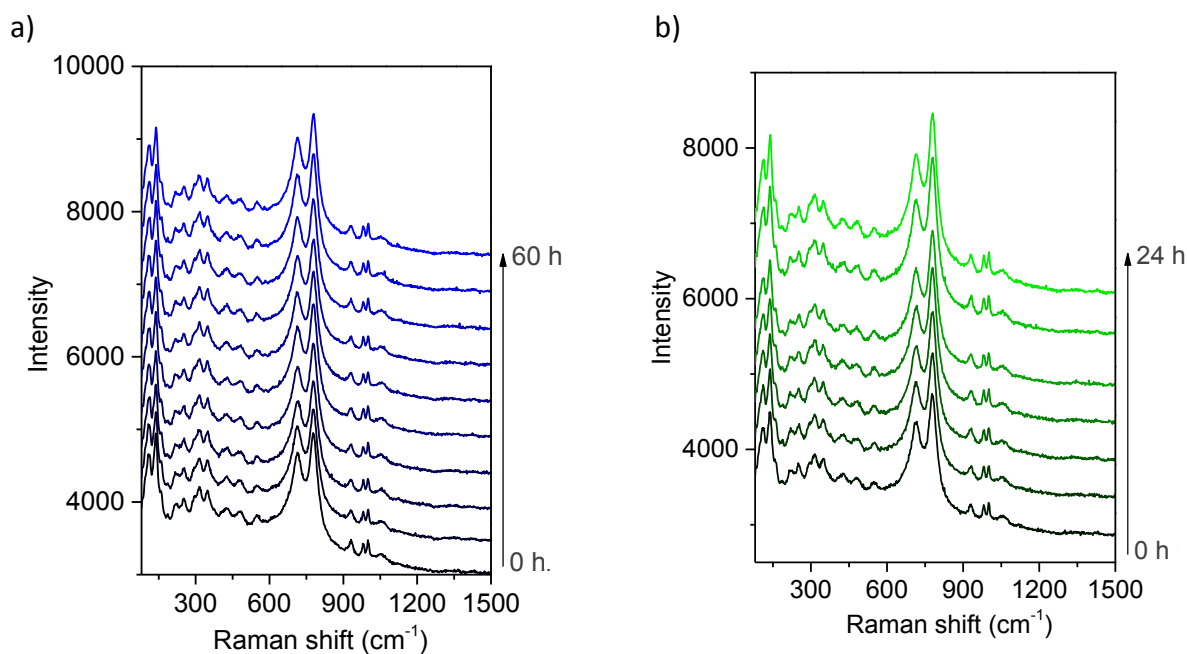


Figure S 2.7. a) Raman spectra taken at 480 °C under the flow of O_2/He 21/79 over 60 h, b) Raman spectra taken at 480 °C under the flow of Helium over 24 h.

3 Supported liquid phase catalysts; the influence of local geometric structure on selectivity in propane oxidation to propene

3.1 Introduction

Currently, olefins are produced applying well-established technologies like steam cracking, fluid-catalytic cracking, and catalytic dehydrogenation. Nevertheless, oxidative dehydrogenation of propane to propene (ODP) has been extensively investigated over the last decades with the aim to develop a process in which propene is produced independent of other olefins, and to overcome the thermodynamic limitations and catalyst deactivation.¹ Much of the attention has been devoted to vanadium containing systems due to their superior performance.¹⁻⁴ The main focus was on structural-activity relationships applying highly crystalline phases. However, surface termination of crystalline phases,⁵ different structural defects that can appear close to the surface of complex mixed oxide⁶, and as an extreme case, formation of a thin amorphous phase on the surface of crystalline phase⁷, which is of more relevance than the bulk of the catalysts, should be taken into the consideration. Therefore, by applying the concept of supported liquid phase catalyst (SLP) for ODP reaction as a model catalyst, it was studied whether the structurally equilibrated species in a liquid, being an amorphous phase, fulfill the required characteristics acting for selective alkane activation in comparison to the more rigid structural arrangements of metal oxide species⁸ at the surface of the model monolayer catalysts. Amakawa et al.⁸ proposed

that the frustrated surface species with high potential energy are apparently more active for activation of alkanes. Accordingly, strain at the anchoring bonds on the surface of support was proposed to be a decisive factor for activity. No straightforward relation between the structure of the active surface species and the selectivity of the catalysts has been identified so far. In an attempt to verify the concept of frustrated active sites, the properties of the supported liquid-phase catalysts were explored. In the liquefied active layer the metal oxide species should occur in relaxed configuration.

A classic example for SLP catalysts is the sulfuric acid catalyst that has been introduced by BASF hundred years ago. It is still the standard catalyst for production of sulfuric acid today. The catalyst is composed of V_2O_5 promoted with alkali sulfates on a porous inert carrier, patented as German Patent 291792. The alkali sulfates form a molten phase under the reaction conditions for which the melting point correlates with the onset of activity.⁹⁻¹⁴

A few studies have been already performed applying SLP catalysts for oxidative dehydrogenation reactions.^{15, 16} Kumar et al. applied supported molten alkali metal chlorides in the oxidative dehydrogenation of light alkanes and attributed its high selectivity to the formation of a molten phase under the reaction conditions.^{16, 17} However, chloride salts will result in an instability of the catalyst.^{15, 16, 18, 19}

The objective of this work is to investigate catalytic systems applying silica-supported mixtures of vanadium pentoxide and potassium carbonate which result in formation of different potassium vanadates on the surface of the support. Potassium vanadates have been chosen as a model system in the present investigation due to the appropriate melting point of these solids, which allows investigating their catalytic performance both in solid and liquid states. The melting point was varied by changing the V:K ratio. Silica (Aerosil 300) was used as support. The catalytic data were measured below and above the melting point to investigate the influence of phase transition from solid to liquid on the performance of the supported catalysts. The V/Aerosil and K/Aerosil catalysts prepared in the same way, monolayer V_xO_y/SiO_2 and crystalline $K_3V_5O_{14}$ were studied as references. The catalysts have been characterized applying XRF, XRD, DSC, SEM, EDX, Raman and XPS. The conceivable reasons for observing different behaviors of catalyst in the solid and molten states were investigated by implementing high-temperature XPS, and in-situ characterization applying Raman and UV-Vis spectroscopy while simultaneously monitoring the gas-phase. This study

focuses on investigating the influence of local geometric structure and collective electronic properties on the selectivity of propane oxidation to propene.

3.2 Experimental

3.2.1 Preparation

K_2CO_3 (Merck), V_2O_5 (BASF), Aerosil 300 (Dequssa), were dried before using. Thermal spreading was applied for preparation of supported catalysts. To do so, the water slurries of K_2CO_3 , V_2O_5 and Aerosil with a systematic variation of potassium and vanadium content were prepared. The ratio of K:V has been varied based on the phase diagram of $K_2O - V_2O_5$.²⁰ The mole percentage of K_2CO_3 at the intervals of 20-40, which gives melting points between 400-500 °C, was the region of interest. The alkali contents higher than 40 % were not used due to corrosion problems. The nominal loading of 10 wt % was selected based on the results of screening step for finding an optimum loading which provides both acceptable activity and detectable melting signal in Differential Scanning Calorimetry (DSC). The pure V/Aerosil and K/Aerosil catalysts have been prepared as references. The slurry was spray dried in a Büchi mini spray dryer with the inlet temperature of 200 °C and the outlet temperature of 130 °C. The obtained powder was calcined at a temperature above the expected melting point of the coated phase, 620 °C for SLP catalysts, in 100 ml/min 21 % O_2 /79 % Ar for 16 hours in a rotating quartz tube. The applied heating rate was 10 Kpm.

$K_3V_5O_{14}$ and $K_2V_8O_{21}$ were also prepared to be used as the reference materials. The applied synthesis method and the detailed characterizations were discussed in chapter 2.

In the following sections, the prepared supported catalysts will be referred as xKV, where x represents the experimental atomic percentage of K in the coating.

3.2.2 Characterization

X-ray Fluorescence (XRF)

The amount of potassium, vanadium and silicon in the prepared catalysts was determined by X-ray fluorescence analysis (XRF). The catalysts and the corresponding standards were mixed with lithiumtetraborate flux (FX-X100, Fluxana) and fused in a Vulcan Fusion Machine (HD Electronic & Elektrotechnik GmbH) under formation of flat molten glass discs, which

were analyzed by X-Ray Fluorescence spectroscopy applying the spectrometer Pioneer S4 (Bruker AXS GmbH). The XRF instrument was wavelength dispersive and equipped with a Rh-anode.

X-ray Diffraction (XRD)

The X-ray diffraction (XRD) measurements were performed in Bragg-Brentano geometry on a Bruker AXS D8 Advance II theta/theta diffractometer, applying Ni filtered Cu K α radiation and a position sensitive energy dispersive LynxEye silicon strip detector. The catalyst powder was filled into the recess of a cup-shaped catalyst holder, the surface of the powder bed being flush with the catalyst holder edge (front loading). The temperature dependent XRD data were collected on a STOE Theta/theta X-ray diffractometer (CuK α radiation, secondary graphite monochromator, scintillation counter) equipped with an Anton Paar XRK 900 in-situ reactor chamber with the gas feed flowing from the top to the bottom of the chamber. The temperature was measured by two type K thermocouples. While the first one (TC1) was in close contact to the catalyst bed, the second thermocouple (TC2) was situated near the entrance of the gases.

BET

Surface areas of the catalysts were analyzed by nitrogen adsorption (Autosorb AS-6B, Quantachrome) after a pretreatment at 150 °C for 1 h in vacuum. The specific surface areas were determined according to the Brunauer–Emmett–Teller (BET) method using 11 data points in the relative pressure p/p_0 range of 0.05–0.3.

Differential Scanning Calorimetry (DSC)

Calorimetric experiments were carried out on a Mettler-Toledo HP DSC 827 calorimeter, equipped with an Au–AuPd Sensor, in an Alumina crucible in a dynamic 21 % O₂/ 79 % Ar (70 ml/min) flow with 10 Kpm heating rate and 5 Kpm cooling rate. Temperatures were calibrated against the melting points of In and Zn.

Scanning Electron Microscopy (SEM) and Energy-Dispersive X-ray Spectroscopy (EDX)

The SEM images were captured on a Hitachi S-4800 Field Emission Scanning Electron Microscope, working in the kV range 0.1 to 30. Morphology studies were undertaken at a voltage of 1.5 kV and a relatively close working distance of 3 mm. The Energy Dispersive X-ray Analysis Data were detected with Bruker EDX System using a SDD (silicon drift detector). The working distance for detecting x-rays is, in this case, optimized to 10 mm.

X-ray Photoelectron Spectroscopy (XPS)

Samples were investigated as pressed pellets. Spectra were recorded at room temperature, using non-monochromatized Al K α (1486.6 eV) excitation and a hemispherical analyzer (Phoibos 150, SPECS). The correction for charging effects was carried out by internal referencing to the Si2p peak of SiO₂ to 103.3 eV. The level of charging was in the range of 3.9-4.9 eV. To calculate the elemental composition, theoretical cross sections from Yeh and Lindau²¹ have been applied. Additional experiments were performed to assess the surface state and composition at various temperatures. Since V was expected to undergo reduction in UHV during heating, very small amount of O₂ (2x10⁻⁸ mbar) was dosed into the UHV chamber during the experiment to at least partially counteract the reduction. Since the magnitude of charging was changing during high temperature measurements, the referencing to Si2p did not work very well. For V2p, instead, the O1s spectrum was fitted, which was recorded together with V2p in one scan, to extract the O1s binding energy of the K_xV_yO_z, under the assumption that this should be at 530 eV. Then the V2p was shifted accordingly, and these V2p(3/2) spectra were plotted.

Raman spectroscopy

Raman measurements were conducted applying a 532 nm, 50 mW DPSS Laser (Cobolt 05-01 series) and a TriVista Raman Microscope System (TriVista TR 557, S&I GmbH) equipped with a CCD camera (Spec10: 100BR, Princeton Instruments) applying the 10X Objective and laser power of 2 mW at catalyst position. For calibrating the frequency of spectrometer a silicon wafer (520.7 \pm 0.5 cm⁻¹) was utilized. The in-situ reaction cell was a CCR 1000 cell from Linkam with the feed flowing from the top to the bottom of the chamber. The gas feed was mixed by means of Bronkhorst mass flow controllers, using helium as inert balance gas. The effluent gas composition was monitored with a micro-GC (Agilent) connected to the out let of the cell. The Linkam cell was modified to accurately measure the temperature close to the surface of the catalyst sample by installing a second thermocouple.

UV-Vis spectroscopy

UV-Visible diffuse reflectance spectra were measured on a Cary 5000 spectrometer (Agilent) equipped with a Harrick Praying Mantis™ diffuse reflectance attachment (DRP-P72) and a reaction chamber (HVC-VUV). All data were obtained in reflectance percentage and then converted to the Kubelka-Munk function. Spectralon was loaded into the reaction chamber

to collect a baseline spectrum in the range between 1000 and 200 nm. To elucidate the change of vanadium environment due to adsorption of water, the experiments have been performed after one step of pretreatment under the flow of synthetic air at 350 °C for half an hour. The reaction gas feed was mixed using mass flow controllers (Bronkhorst), using helium as inert balance gas. The effluent product gas composition was monitored with a micro-GC (Agilent). The temperature was raised stepwise with a rate of 5 Kpm and the spectra and catalytic data were collected after stabilization of the temperature. Once the catalyst reached the desired temperature, spectra were collected every 3 minutes until changes were no longer observed.

Activity test

The catalytic activities of the xKV catalysts were tested in the oxidative dehydrogenation of propane in an eight-fold parallel reactor set-up (Integrated Lab Solutions, Berlin, Germany). The prepared catalysts were first pressed, then crushed in a mortar, and finely sieved to have a particle size of 250 - 355 µm. The temperature range applied for the reaction was between 375 °C to 500 °C. Two different feed compositions of C₃H₈, O₂, and N₂ in a molar ratio of 10:5:85 and 7.5:7.5:85 have been applied. Reactants and products were analyzed by online gas chromatography (Agilent 7890). The conversion and selectivity were calculated based on the number of carbon atoms and the products found. The propane conversions on pure Aerosil support and K/Aerosil were below 3 % up to 500 °C reaction temperature.

3.3 Results

3.3.1 Physical and chemical properties of the prepared catalysts

Table 3.1. Physical and chemical properties of prepared catalysts

Catalyst number	ID	Temp. of calc. (°C)	Analytical atomic ratio (K:V)	Analytical loading ^a (wt %)	S _{BET} (m ² /g)	Melting point ^c , T _m (°C)	XRD expected phases ^{d 20}	XRD observed phases
22117	100K	700	100:0	9	11	-		
22233	35KV	620	35:65	8.8	45	405	K ₂ V ₈ O ₂₁ , K ₂ V ₂ O ₆	K ₃ V ₅ O ₁₄
22226	27KV	620	27:73	8.8	38	403, 452, 520	K ₂ V ₈ O ₂₁ , K ₂ V ₂ O ₆	K ₃ V ₅ O ₁₄ + unknown ^b
22512	22KV	620	22:78	8.6	23	468, 520	K ₂ V ₈ O ₂₁ , K ₂ V ₂ O ₆	unknown ^b

22665	100V	700	0:100	9.5	44	-	V ₂ O ₅	V ₂ O ₅
-------	------	-----	-------	-----	----	---	-------------------------------	-------------------------------

^a Analyzed by XRF, based on V₂O₅+K₂O

^b Similar to K₂V₆O₁₆·1.5 H₂O

^c Determined by DSC

^d Based on the phase diagram

The vanadium and alkali content in the catalysts were determined by XRF. The results are presented in Table 3.1. The loading of the catalysts is calculated based on the sum of the mass of K₂O and V₂O₅ in the final catalysts. Both the addition of vanadium and doping with the alkali metals result in a lowering of the surface area of Aerosil 300 (311 m²/g).

The results of XRD analysis of the freshly prepared catalysts are shown in Figure 3.1, and the observed crystalline phases are summarized in Table 3.1. As it was expected from the phase diagram, crystalline V₂O₅ was not observed by XRD on the catalysts surface. Instead, different alkali vanadates developed on the surface of the support. According to the phase diagram, the presence of K₂V₂O₆ and K₂V₈O₂₁ is expected for catalysts that contain 20-40 mole% K₂O. The phases observed by XRD over the supported catalysts 35KV, 27KV, and 22KV that contain K₂O in the range of 40-20 mole% differ from the published phase diagram. This indicates that either the thermodynamic equilibrium was not reached in the applied catalyst synthesis or the support has an impact on the phase formation. The broad band at 22° 2θ corresponds to amorphous silica. An unknown phase was detected in the catalysts 27KV and 22KV. The XRD pattern of the unknown phase resembles the pattern of K₂V₆O₁₆·1.5H₂O (hexavanadate).²² The difference could be due to presence of various amount of water in the phase formed after melting. For the catalyst 35KV, K₃V₅O₁₄ is the only phase detected by XRD beyond the amorphous support.

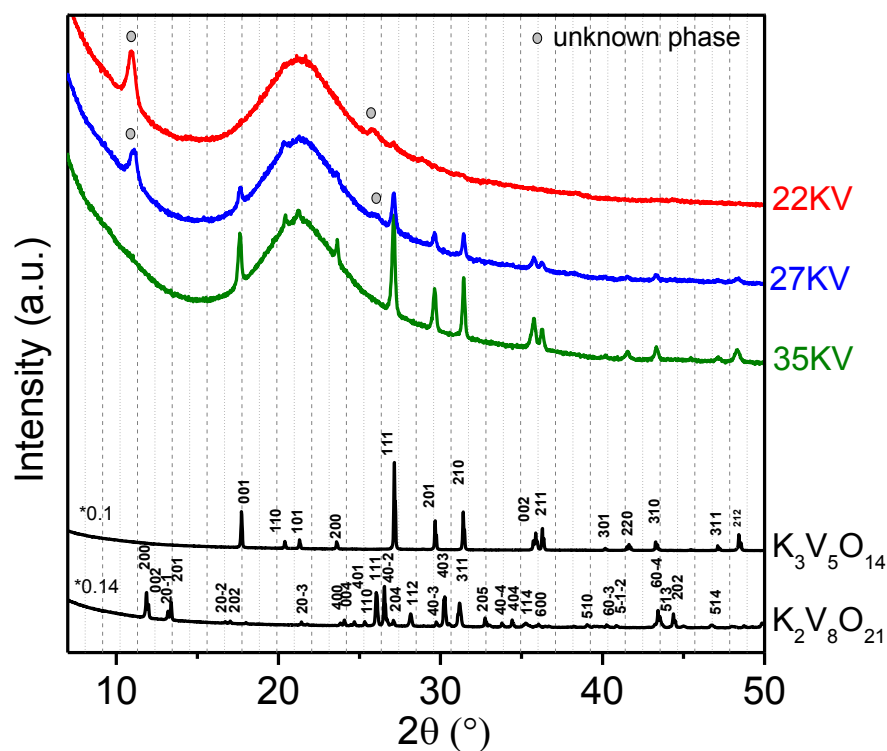


Figure 3.1. XRD patterns of xKV catalysts recorded at room temperature after synthesis (The patterns are offset for clarity).

Figure 3.2 compares the Raman spectra of the fresh catalysts. Presence of unknown phase hinders the detailed assignment of the corresponding Raman modes, but the catalysts showing similar XRD patterns present also similar Raman features. For $K_3V_5O_{14}$, and $K_2V_8O_{21}$ containing catalysts, these phases have been prepared to be used as reference phases. The Raman spectrum of $K_3V_5O_{14}$, shown in Figure 3.2, was measured for the first time in this work. Detailed assignments of the present vibrational modes applying DFT calculations for both $K_3V_5O_{14}$, and $K_2V_8O_{21}$ are given in Chapter 2.

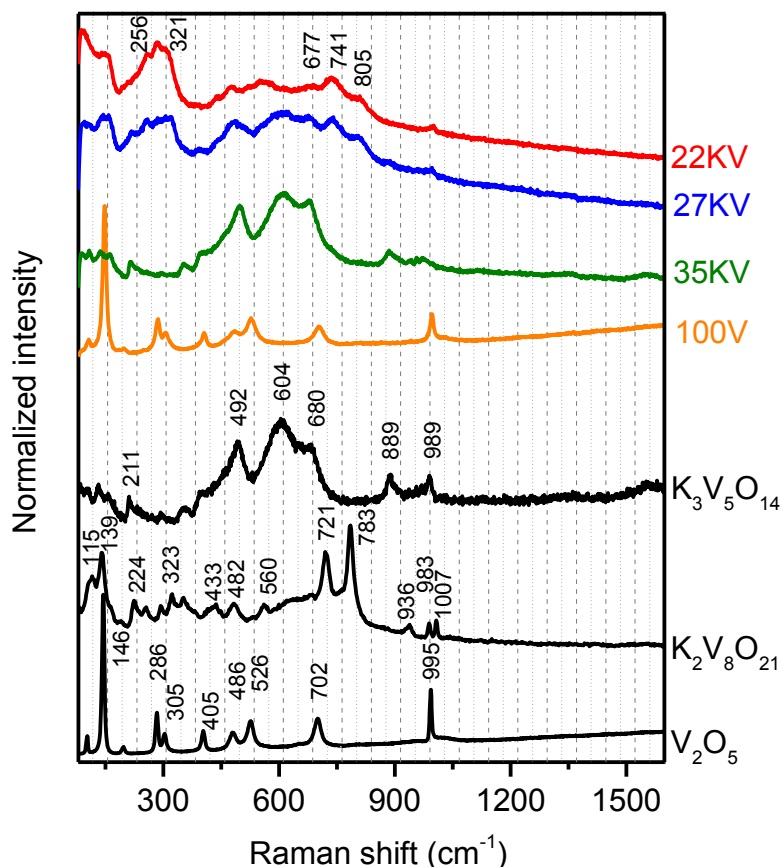
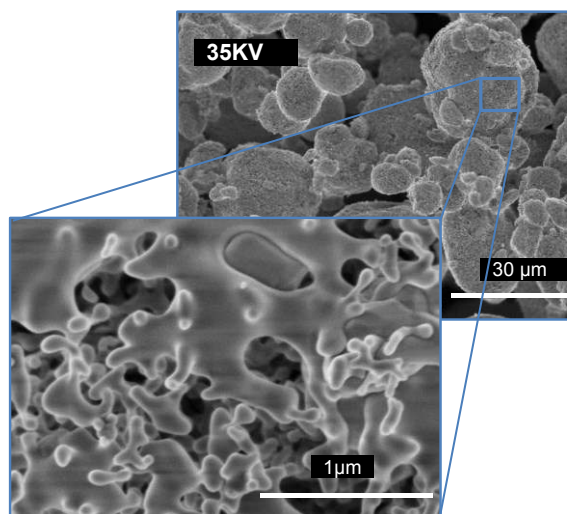


Figure 3.2. Raman spectra of the freshly prepared catalysts recorded at room temperature.

The Raman spectrum of the catalyst 35KV is dominated by the vibrational modes of K₃V₅O₁₄, confirming the existence of K₃V₅O₁₄ as the only detectable crystalline phase observed by Raman spectroscopy on the surface of support in agreement with the XRD data. However, the relative intensity of the bands at 680 and 604 cm⁻¹ deviates slightly from the reference K₃V₅O₁₄. The impact of the support may be one possible explanation for this observation. Catalyst 27KV shows the Raman modes of K₃V₅O₁₄. In addition, the peaks at 256, 321, 677, 741, 805 cm⁻¹ are attributed to K₂V₆O₁₆·1.5H₂O²³ like phase. Concerning catalyst 22KV, contributions of the Raman modes of K₂V₈O₂₁ at 139 cm⁻¹, 721 cm⁻¹ and 783 cm⁻¹ accompanied with similar bands to K₂V₆O₁₆·1.5H₂O²³ are noticeable. The Raman spectrum of the catalyst 100V is dominated by the Raman features of V₂O₅ as expected. The vanadyl bond of vanadium monolayer catalysts gives rise to the Raman band at 1027-1040 cm⁻¹.⁴ This band is not detectable in our catalysts, approving transformation of vanadium to potassium vanadate phases.

a)



b)

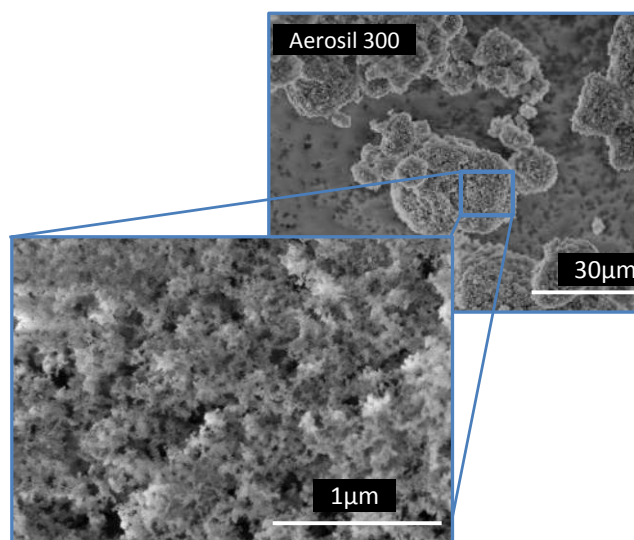


Figure 3.3. SEM images of a) as-prepared catalyst 35KV, and b) Aerosil support.

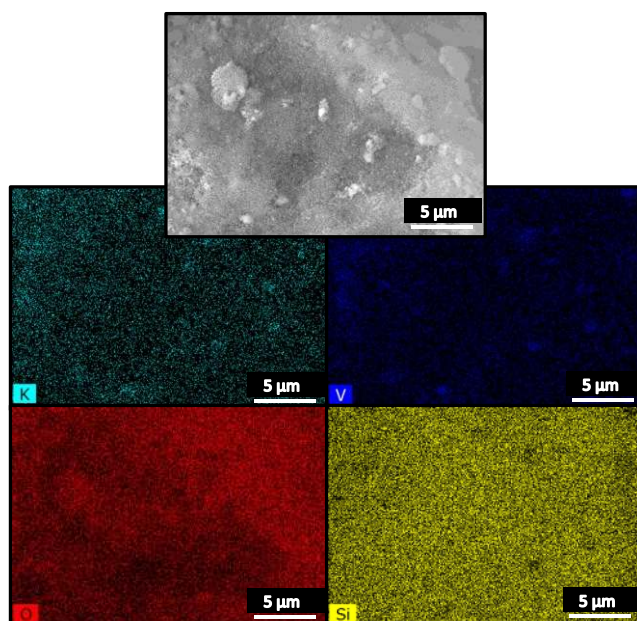


Figure 3.4. SEM image and elemental mappings of catalyst 35KV.

The morphology of 35KV catalyst was analyzed applying SEM, shown in Figure 3.3. It is apparent that the spherical particles of pure Aerosil are still discernible after synthesis and a layer of potassium vanadate phase covers the support. Comparing the Aerosil with 35KV with the higher resolutions in Figure 3.3 shows that the primary particles are linked together after deposition of the coating. To explore the dispersion of K and V species in the catalyst

35KV, and also to verify the elemental composition, EDX analysis was carried out. EDX maps of 35KV catalyst are depicted in Figure 3.4. Only K, V, Si elements were detected, confirming the absence of any impurities in the catalyst. The V/K ratio of 1.9 determined by EDX, being slightly higher than the value calculated from XPS, but in accordance with XRF, amounting to 1.86. The EDX map presents that K and V were well distributed on the surface of the Aerosil support. This is a further evidence for the successful synthesis of the SLP catalysts.

3.3.2 DSC analysis

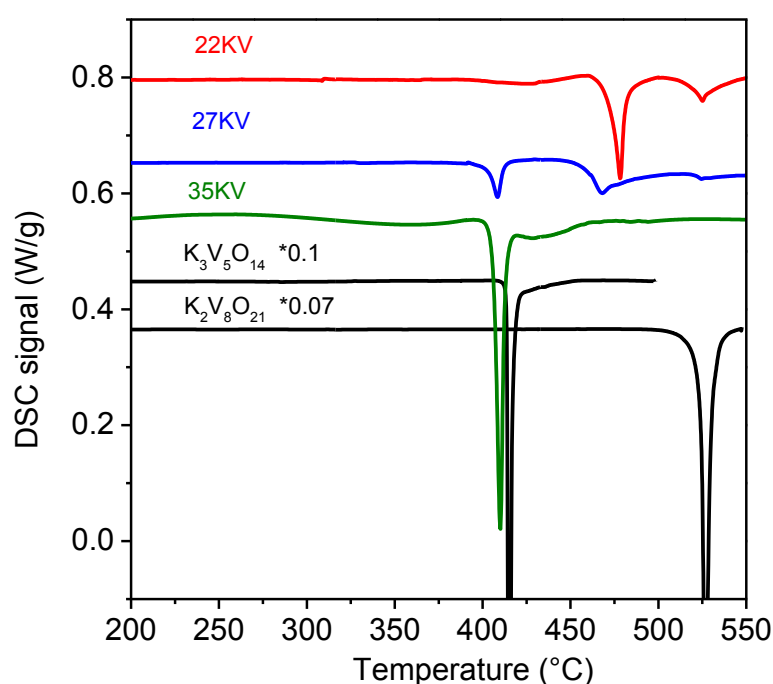


Figure 3.5. DSC profiles of the xKV catalysts with the heating rate of 10Kpm under 70 ml/min flow of 21 % O₂/ 79 % Ar. DSC of K₃V₅O₁₄ and K₂V₈O₂₁ are also included for comparison.

The DSC analysis (Figure 3.5) is in good agreement with the published phase diagram. To make sure that the endothermic events are reversible, three cycles of heating and cooling have been applied for all DSC analyses (see supporting information Figure S3.1). The onsets of the endothermic events observed in DSC analysis are listed in Table 3.1. Based on these results three main endothermic peaks at about 405 °C, 450 °C and 520 °C are detectable. Depending on the composition of the coating, either one or a combination of two of the endothermic events is noticeable. Catalyst 22KV is characterized by one clear endothermic event in the DSC profile at approximately 468 °C, but a weak endothermic signal is also noticeable at 520 °C. The supported K-V oxide mixture of catalyst 27KV shows two

endothermic events at approximately 405 °C and 452 °C, and a small contribution from melting peak at 520 °C. In the temperature window studied for the oxidative dehydrogenation of propane (375-500 °C), the supported mixture of the two catalysts is most likely not completely in molten state, since both catalysts display the endothermic peak at 520 °C in the DSC profiles. A lower melting point of 405 °C for catalyst 35KV was detected by DSC analysis. It is expected that only in the catalyst 35KV the supported mixture is completely molten at a reaction temperature of higher than 405 °C in ODP. For the other catalysts mixtures of liquid and solid phases are expected.

To explore the phase transitions in more details and confirm liquefaction, XRD has been performed at different temperatures under the flow of 21O₂/79He, see Figure 3.6. Based on XRD of catalyst 35KV, K₃V₅O₁₄ vanishes above the melting point (405 °C based on DSC), and crystallizes again at lower temperatures, showing evident hysteresis. Furthermore, a contribution of a new peak at 11.3° between 350 °C to 425 °C, most likely due to the formation of a minor amount of hexavanadate like phase, is noticeable. The shoulder in the DSC analysis of catalyst 35KV after melting peak of K₃V₅O₁₄ is most likely related to the melting of hexavanadate-like phase. In the temperature dependent XRD of sample 27KV, melting of hexavanadate-like phase above 450 °C is clearly detectable, being in accordance with DSC results. Due to the lower detection sensitivity of in-situ XRD, the minor phases detected by room temperature XRD, such as K₃V₅O₁₄ for catalyst 27KV or K₂V₈O₂₁ in catalyst 22KV, are not detectable at elevated temperatures. In accordance with the XRD results, the first melting signal in the DSC experiment is related to K₃V₅O₁₄, the second one originates from melting of a hexavanadate-like phase. The melting signal at 520 °C should be due to the melting of K₂V₈O₂₁ as indicated by DSC of the pure K₂V₈O₂₁ reference compound (see chapter 2).

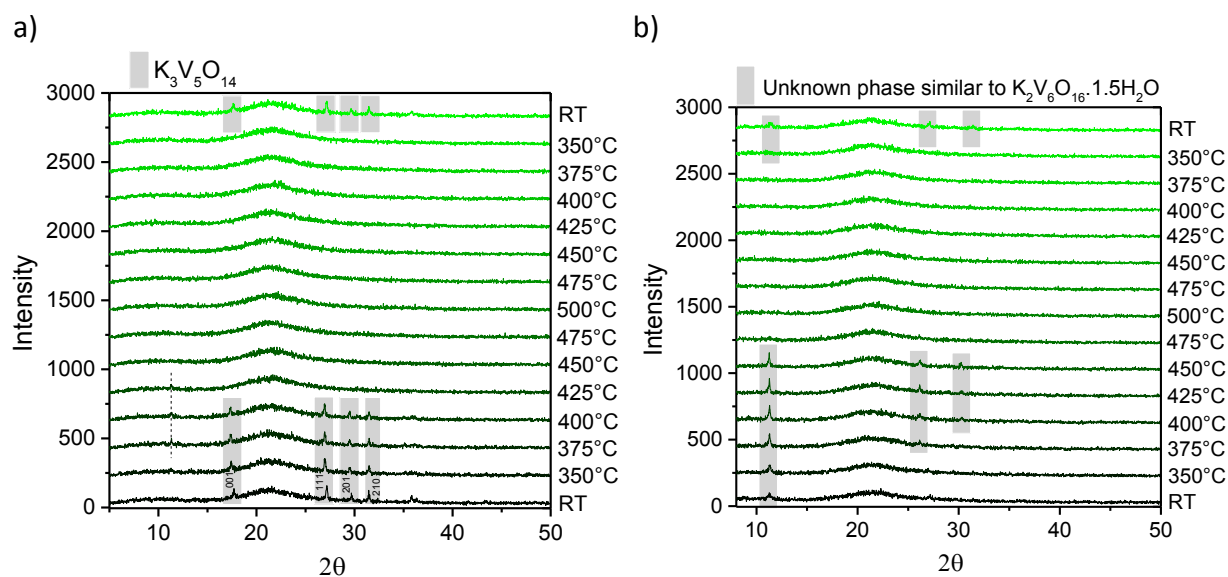


Figure 3.6. XRD patterns of catalysts a) 35KV, b) 27KV, under the flow of 10 ml/min 21 % O_2 / 79 % Ar recorded at different temperatures (heating rate of 10Kpm and cooling rate of 5Kpm).

For reference, phase pure $K_3V_5O_{14}$ and $K_2V_8O_{21}$ were prepared (chapter 2). These pure phases were used to calibrate the DSC measurements. Analysis of the enthalpy of melting in DSC profiles of $K_3V_5O_{14}$ and $K_2V_8O_{21}$ and xKV catalysts provides a rough estimation of the percentage of each phase in the coating (the degree of crystallinity of present phases, however, may cause uncertainty in the results). To do so, the area under the peaks has been compared taking the loading of catalysts into the consideration. To calculate the amount of hexavanadate like phase the sum of the percentage of $K_3V_5O_{14}$ and $K_2V_8O_{21}$ has been subtracted from 100 %, which gives indeed a rough estimation. The results indicate that the majority of K and V (98 wt %) in the coating of 35KV are participating in the formation of $K_3V_5O_{14}$ and about 2 wt % contribution from hexavanadate like phase is estimated. A mixture of hexavanadate like phase and $K_3V_5O_{14}$ is present on the surface of 27KV, hexavanadate like phase being the major one owing about 83 wt % concentration. For catalyst 22KV hexavanadate like phase is the dominant one accompanied by a minor amount, 0.1 wt %, of $K_2V_8O_{21}$.

Table 3.2. Calculated Percentage of potassium vanadates in the coating of xKV catalysts by comparison of area of endothermic peak corresponding to melting of $K_3V_5O_{14}$ and $K_2V_8O_{21}$ in DSC heating curves of compounds with that of xKV catalysts. The amount of hexavanadate like phase has been calculated by subtraction of percentage of $K_3V_5O_{14}$ and $K_2V_8O_{21}$ in the coating from 100.

Catalyst ID	Percentage of $K_3V_5O_{14}$ in the coating (wt %)	Percentage of hexavanadate like phase in the coating (wt %)	Percentage of $K_2V_8O_{21}$ in the coating (wt %)
35KV	98	2	0
27KV	17	82.99	~0.01
22KV	~0	99.9	~0.1

3.3.3 XPS analysis

The purpose of this part of characterization was to apply a quantitative spectroscopic technique to measure the elemental composition near the surface of the catalysts and determine whether there is a correlation between surface composition and catalytic performance.

Table 3.3 compiles the quantitative information obtained from XPS analysis. All catalysts contain the expected main elements (O, Si, V, and K), and carbon contaminations.

Table 3.3. Surface-near molar ratios of as prepared xKV catalysts according to XPS.

ID	V/Si	O/(V+Si)	C/Si	K/Si	V/K
35KV	0.026	2.04	0.045	0.020	1.33
27KV	0.04	2.05	0.081	0.021	1.9
22KV	0.049	2.01	0.14	0.016	3.15

When comparing the surface to the nominal bulk K/Si ratio, the values are close to each other, and the surface K concentration scales well with nominal bulk K content for 22KV and 27KV. By increasing the K content (catalysts 35KV), the surface ratio of K/Si become a bit smaller than the bulk values. The V-to-Si ratio increases with the increase of the V loading. However, when we plot the observed surface-near V/Si ratio as a function of the analytical bulk V/Si ratio (Figure 3.7b), it can be seen that the surface ratios are lower. This suggests that KV_xO_y in these catalysts is covered (e.g., by C or K). The different behaviors of K and V

suggest that K covers the surface of the catalysts. The lower V/K ratios, shown in Figure 3.7c also express the same.

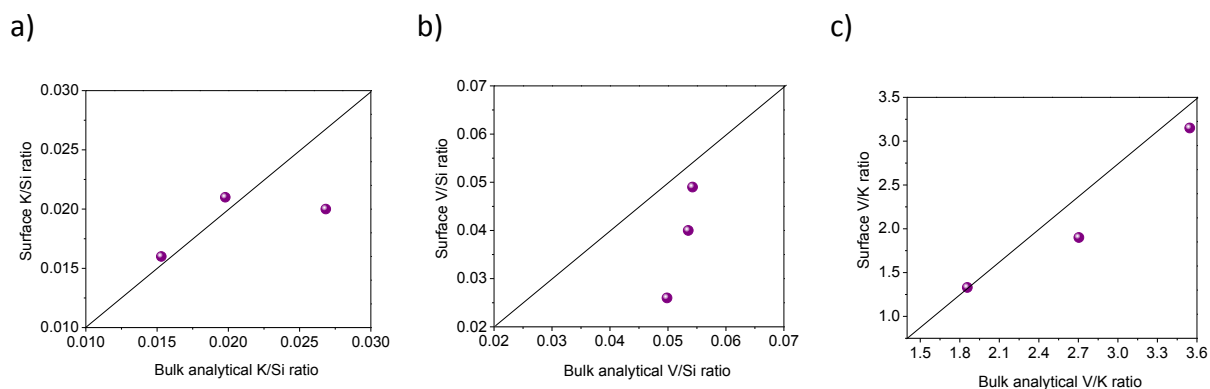


Figure 3.7. Surface-near a) K/Si, b) V/Si, and c) V/K ratios as a function of the analytical bulk values determined by XRF.

The observed $O/(V+Si)$ ratio scatter around 2, near the expected ratio of slightly larger than 2. The detected binding energy of $V2p(3/2)$ at $517.3 (\pm 0.25)$ eV is characteristic of V^{5+} (Ref: 517.1 ± 0.1 eV).

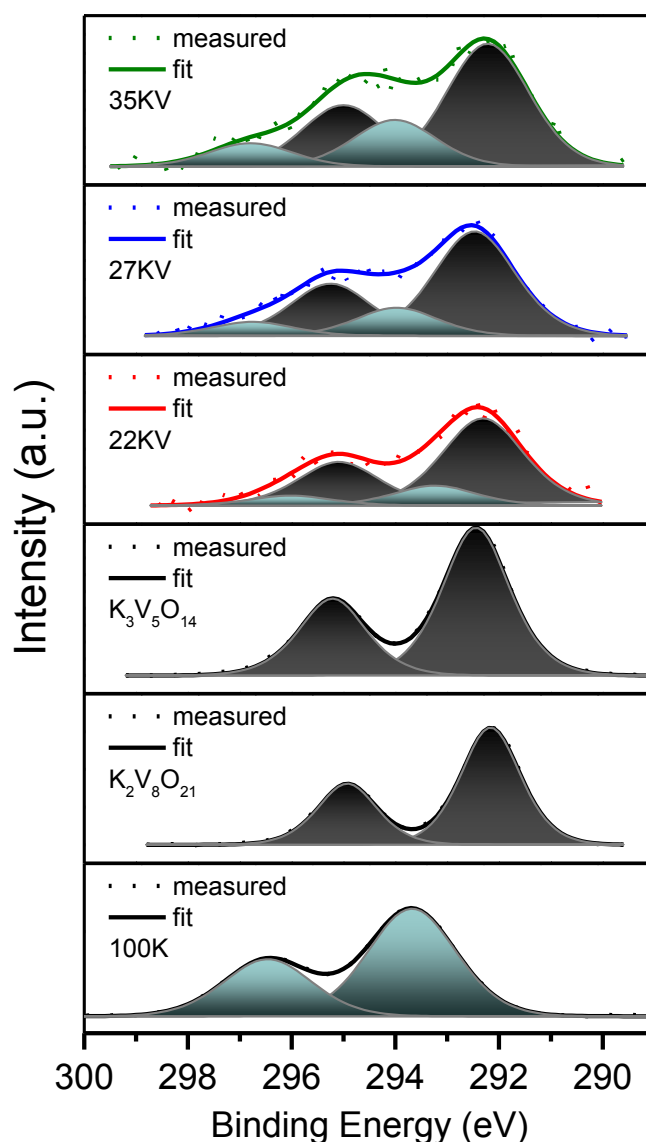


Figure 3.8. Deconvolution of K2p spectra applying four peaks.

K2p spectra of xKV catalysts, $K_3V_5O_{14}$, $K_2V_8O_{21}$ and 100K are depicted in Figure 3.8. Since not only the intensity but also the shape of the K2p spectra changes, see Figure 3.8, a two-component (4 peaks) fit has been applied for xKV catalysts. Note that 2p levels are doublets. The 2 peaks (3/2 and 1/2) of K2p for the same species are 2.77 eV apart. Catalyst 35KV has clearly two K species, and with decreasing the bulk K content in the catalysts series, the relative abundance of one of the components decreases. Both of these species are ionic K. Based on obtained binding energies from K2p spectrum of $K_3V_5O_{14}$ (292.4 and 295.2 eV), $K_2V_8O_{21}$ (292.2 and 294.9 eV) and 100K (293.7 and 296.5 eV) served as references, the main contribution is from potassium in the structure of potassium vanadates and the

second/smaller component is initiating from surface species like in 100K which could, also, be in the form of potassium silicates.

3.3.4 Catalytic activity test

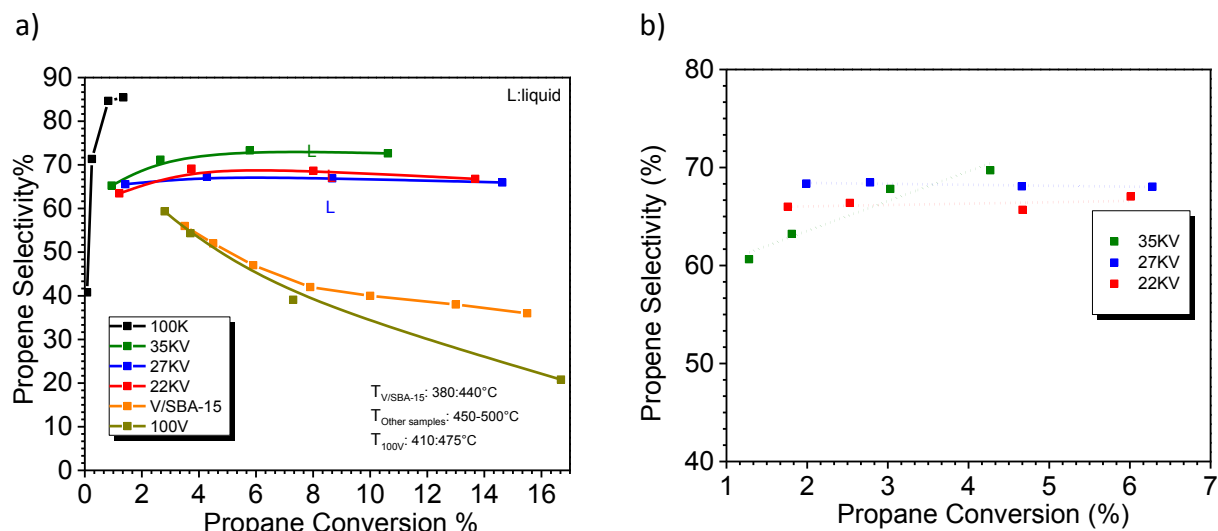


Figure 3.9. a) Selectivity versus conversion in oxidative dehydrogenation of propane, feed composition $C_3H_8:O_2:N_2$ 10:5:85, $W/F=1.8$ gs/ml, $m_{cat}=300$ mg b) Contact time variation at 475 °C, feed composition $C_3H_8:O_2:N_2$ 10:5:85 %, $W/F=0.9-1.2-1.8-2.25$ gs/ml, $m_{cat}=300$ mg.

A comparison of the performance of all prepared catalysts in the ODP feed of $C_3H_8:O_2:N_2$ 10:5:85 is illustrated in Figure 3.9a. The better performance of SLP catalysts regarding selectivity, in comparison to V monolayer on SBA-15²⁴ and V_2O_5 /Aerosil, is noticeable. The selectivity remains roughly constant with increasing conversion when the active surface is partially molten (22KV and 27KV) or completely molten (35KV). Catalyst 100K which was prepared to use as the reference shows very low activity, demonstrating the negligible contribution of potassium to the activity of the explored catalysts.

In order to investigate the behavior of the catalysts regarding selectivity with increasing conversion, the contact time (g.s/ml) has been varied at constant temperature (475 °C) using the feed composition of $C_3H_8:O_2:N_2$ 10:5:85 %, see Figure 3.9b. 22KV and 27KV give stable selectivity with increasing conversion. This behavior was previously observed for supported molten alkali chloride catalysts²⁵ tested in the ODP reaction. Therefore, the explored SLP catalysts show an essential difference in terms of conversion selectivity plots. They reveal either constant selectivity with increasing conversion or in the case of catalyst 35KV there is even an increase in selectivity with increasing conversion.

To investigate the influence of phase transitions on the performance of the catalysts, a second run of reactivity tests has been conducted after the first run described above. Taking the super-cooling effect into the consideration a complete cooling of the reactors before starting the second cycle is required. For the second run a reaction feed of $C_3H_8:O_2:N_2$ 7.5:7.5:85 % has been introduced into the reactors. Here a second aim was to prevent the probable reduction of vanadium above the melting point by increasing the partial pressure of O_2 .

Figure 3.10a presents the conversion of propane over 22KV, 27KV and 35KV catalysts in the temperature range between 375 and 500 °C with the reaction feed of $C_3H_8:O_2:N_2$ 7.5:7.5:85 %. The catalysts show an interesting behavior with increasing temperature. The conversion drops down suddenly in the temperature range in which the melting signal is observed in the DSC analysis. As it is evidenced by performance, see Figure 3.10a, the temperature, at which the drop happens, shifts to lower temperature with decreasing the melting point of the oxide mixture.

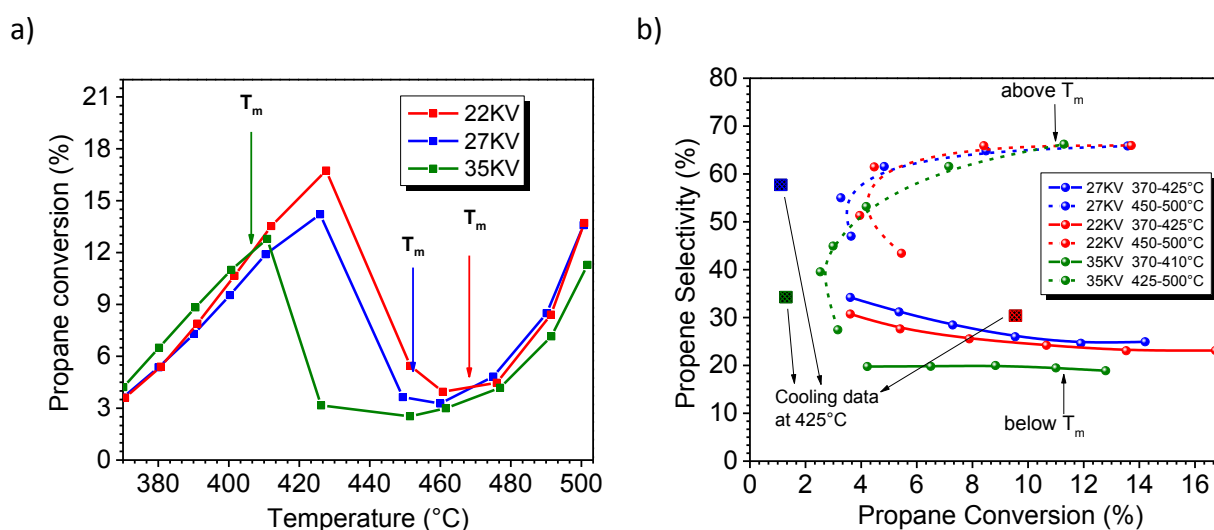


Figure 3.10. a) Conversion of propane in the oxidative dehydrogenation of propane with increasing temperature, and b) propene selectivity as a function of propane conversion in the temperature range below and above the conversion drop over the catalysts indicated in the legend; feed composition $C_3H_8:O_2:N_2$ 7.5:7.5:85 %, contact time: 1.8 gs/ml, mass of catalyst: 300 mg.

When the reaction temperature is increased further, the conversion increases again, due to the temperature and perhaps because of homogenization of the supported liquid phase. Therefore, similar conversions are achieved at higher temperatures. In Figure 3.10b the selectivity to propene is compared at the same conversion achieved in the two different

temperature regions before and after the drop of conversion for the catalysts. About 30 % increase in selectivity towards propene at the comparable propane conversions is noticeable after phase transition from solid to liquid or close to the melting point.

As it is illustrated in Figure 3.10b, two distinct regions can be observed in the S-X plots for catalysts 22KV and 27KV above the melting point. The selectivity is increasing by increasing the temperature up to 475 °C and then leveled off at higher temperatures. In the case of catalyst 35KV, however, there is an instant increase in selectivity by increasing conversion. That could be attributed to the amorphicity which was induced during the first run of reaction which can result in broader melting temperature region.

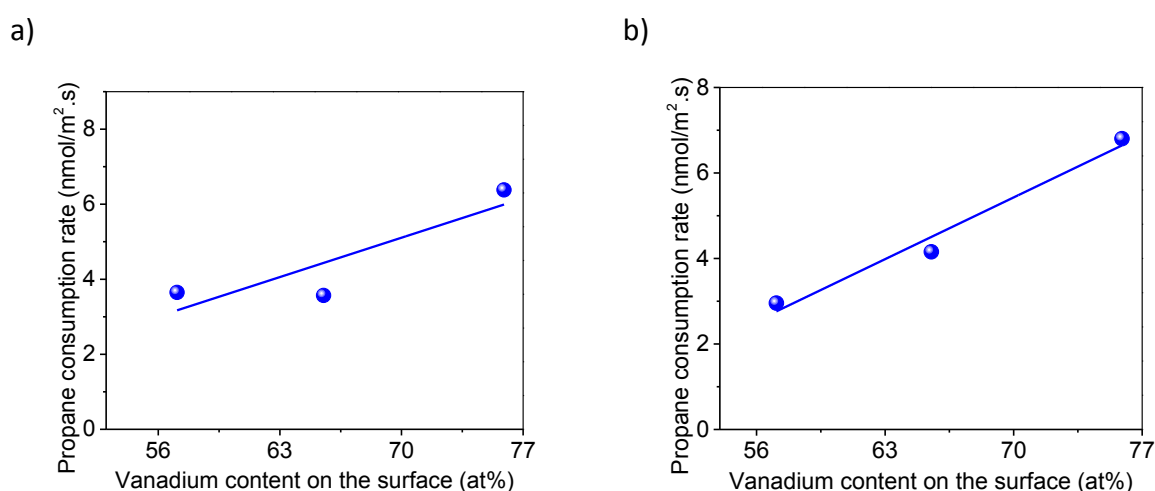


Figure 3.11. Propane consumption rates in the ODP feed of C₃H₈:O₂:N₂ 7.5:7.5:85% and contact time of 1.8 g.s/ml, as a function of vanadium content on the surface determined by XPS a) at 390 °C b) at 490 °C.

Before the melting point, propane consumption rates show a direct correlation to vanadium content on the surface. Rates normalized to surface area exhibit also the same trend above the melting point, see Figure 3.11. The observed trends reveal that the activity is associated with the accessible vanadium.

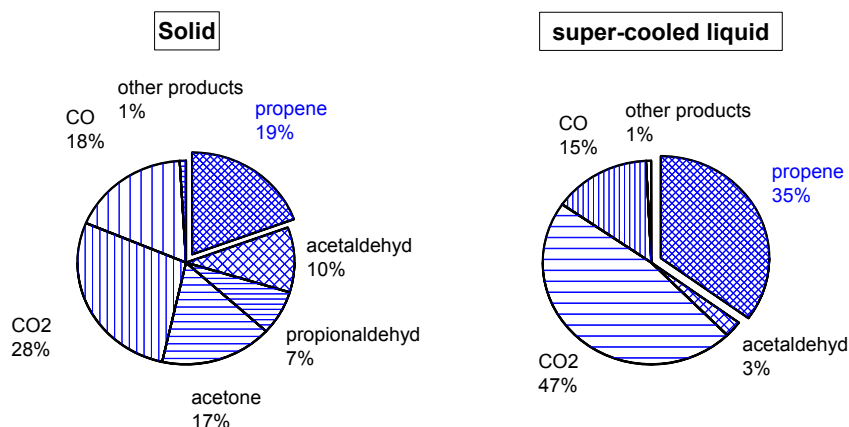


Figure 3.12. Comparison of Product distribution for solid and super-cooled liquid. Feed: $\text{C}_3\text{H}_8:\text{O}_2:\text{N}_2$ 7.5:7.5:85%, Conversion: 0.3-0.4%, T: 370 °C, CT_{solid} : 0.3 g.s/ml, $\text{CT}_{\text{liquid}}$: 6.6 g.s/ml.

To distinguish between the effect of temperature and influence of phase transition itself one additional experiment has been performed. For that, the reactors have been cooled down to 425 °C after taking the data at 500 °C. At this step due to super-cooling, see the cooling curves in supporting information Figure S3.1, the coating of 22KV and 27KV is expected to be still partially in the molten state. The reactivity data taken in this state are presented in Figure 3.10b. The super-cooled state is reflected in the reactivity data of catalyst 27KV and to minor extend in the performance of 22KV. That is most likely due to the instability of catalyst 22KV under the reaction conditions and formation of a new solid phase which will be discussed in the next section. For catalyst 35KV due to the very low temperature needed to reach the super-cooled state and very low activity under these conditions, the study of the super-cooled state was not possible in this experiment. Instead of that the performance of 35KV via cooling at 425 °C is shown. As it is evidenced by cooling data, relatively high selectivity for sample 27KV and 35KV at 425 °C, in the range of observed selectivity for molten states is obtained.

To exclude the contribution of both temperature and conversion a new experiment was designed for catalysts 35KV which has one single melting point at 405 °C. For this, the catalysts are investigated in the solid and super cooled state at a temperature of 370 °C applying different contact times (different amount of sample) to have comparable conversions in the solid and liquid states. The product distribution is shown in Figure 3.12. As it is evidenced, by working in the comparable conversion and fixed temperature of 370 °C

still a higher propene selectivity is achieved for the molten layer. In the solid state, however, when working in low conversion (0.4 %) higher selectivity to oxygenates has been achieved.

To examine the influence of the partial pressure of the reactants on the performance of the catalyst, a kinetic study has been conducted below and above the expected melting point of potassium vanadate for catalyst 35KV which expect to have a completely molten layer. To prevent possible alteration of the catalyst, the kinetic study has been performed in a low conversion regime applying 100mg catalyst 35KV and 0.6 g.s/ml contact time. The solid state of the catalyst has been studied at 380 °C and the molten state at 480 °C. To determine the apparent reaction orders concerning propane and oxygen, the partial pressure of propane and oxygen have been varied between 5.5 to 9.5 %, while the partial pressure of the second component was fixed at 7.5 % in the feed. An increase in the apparent reaction order for both propane and oxygen has been observed above the melting point of the coating, see Table 3.4. In the solid state, the reaction orders of 0.5 for propane and 0.12 for oxygen were obtained. Then, above the melting point, the reaction orders for propane and oxygen increased to 0.9 and 0.63, respectively, reflecting a higher partial pressure dependency when the active component is molten. The high reaction order for O₂ suggests that re-oxidation of the catalyst is kinetically relevant in the molten state.

Table 3.4. Kinetic data below (380 °C) and above (480 °C) the melting point for catalyst 35KV, mass of catalyst: 100 mg, CT: 0.6 gs/ml.

T	n_{C3H8}	n_{O2}	E_a (KJ/mol)
380 °C	0.5+-0.01	0.16+-0.04	120+-5
480 °C	0.95+-0.05	0.57+-0.05	125+-5

The activation energies before and after reaching the melting point were also determined applying the Arrhenius plot. The obtained activation energies of 120+-5 KJ/mole for the solid state and 125+-5 KJ/mole for the liquid state may be interpreted in terms of similar active sites and reaction mechanism in the solid and liquid states. The obtained numbers are in accordance with the literature reported data for activation energy on the supported vanadium based catalyst.²⁶

3.3.5 Characterization of spent catalysts

The chemical composition of the spent catalysts (time on stream one month) was determined by XRF. The results are presented in Table 3.5. The loading of the catalysts is again calculated based on the sum of the mass of K_2O and V_2O_5 in the spent catalysts. Evidently, there is a negligible change in the composition of the catalysts. An obvious decrease in BET surface area has been observed for all spent catalysts except of 22KV which showed the same number as before. The decrease in surface area is more pronounced for the catalyst with the lower melting point, 35KV. One possible explanation is the etching of the silica support due to high potassium content.

Table 3.5. Physical properties of spent xKV catalysts, after being one month under ODP reaction conditions.

Catalyst ID	After ODP reaction				
	S (m ² /g)	Metal ratio ^a (K:V)	Oxide loading ^a (wt %)	Crystalline phases	Melting points (°C)
35KV	16	36:64	9.4	$K_3V_5O_{14}$	401
27KV	16	28:72	9.4	$K_3V_5O_{14}$, unknown phase ^b , $K_{0.5}V_2O_5$	401, 450, 465, 530
22KV	23	22:78	9.2	$K_3V_5O_{14}$, $K_{0.5}V_2O_5$	405, 460, 430

^a Determined by XRF

^b Similar to $K_2V_6O_{16} \cdot 1.5 H_2O$

The spent catalysts were also characterized applying XRD and Raman to investigate probable structural changes during the reaction. The XRD patterns of spent catalysts, depicted in Figure 3.13, demonstrate the stability of catalyst 35KV in terms of present crystalline phase on the surface of the support. The only alteration that can be noticed in the XRD of this catalyst is a change in the shape of background corresponding to the silica support. The support seems to be partially crystalized after the reaction, evidenced by the development of the silica-related reflection (cristobalite like phase) at about 21.5 cm^{-1} . Regarding catalyst 27KV and 22KV instability in phase composition was observed, the alteration being more pronounced for catalyst 22KV. Spent 27KV demonstrates the presence of $K_{0.5}V_2O_5$ besides observed phases for the fresh catalyst, while for catalyst 22KV segregation to $K_3V_5O_{14}$ and $K_{0.5}V_2O_5$ was observed. The explored phase changes are also evidenced by Raman (Figure 3.14) and DSC (Figure 3.15) analysis of spent catalysts. A list of observed phases accompanied by the melting points is given in Table 3.5.

The Raman spectrum of spent 35KV is still dominated by Raman modes of $K_3V_5O_{14}$ which was existing also in the fresh catalyst. In the Raman spectrum of spent 27KV, the extra bands of $K_{0.5}V_2O_5$ ²⁷ at 881, 786, 505, 168 cm^{-1} are detectable. For spent 22KV, which reveals inhomogeneity, the spectra taken at two different positions are depicted in Figure 3.14. The spectrum from the first position is prevailed by vibrational modes of $K_3V_5O_{14}$, while the second position displays the Raman modes of $K_{0.5}V_2O_5$.

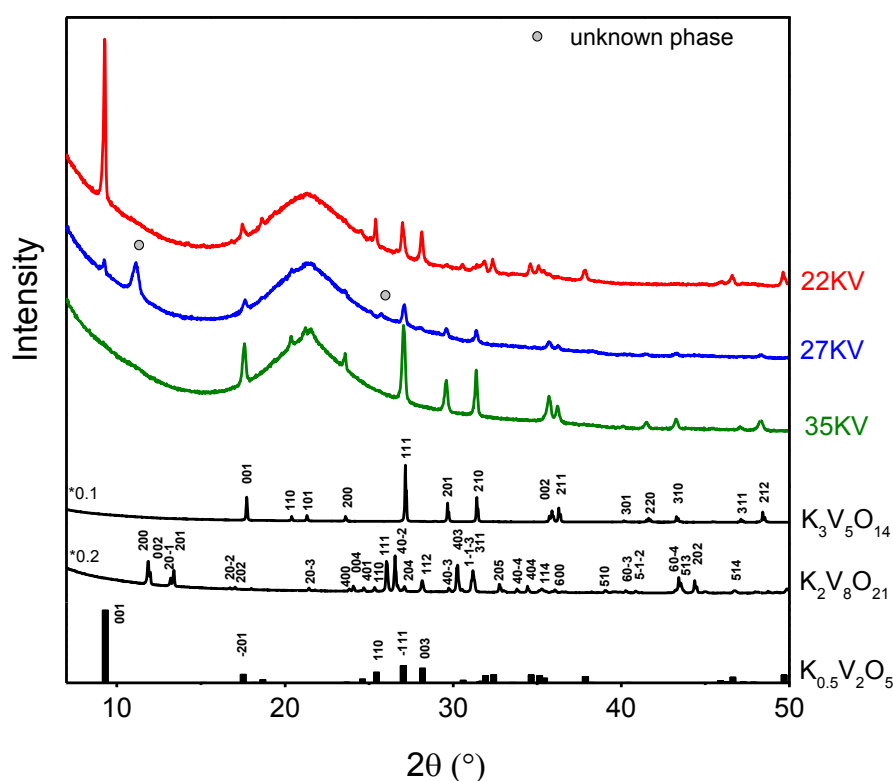


Figure 3.13. XRD patterns of spent xKV catalysts, one month time on stream.

In the DSC profiles of spent catalysts, depicted in Figure 3.15, all the endothermic events of fresh catalysts are still present, after being one month under reaction conditions of ODP. However, the peak at 450 $^\circ\text{C}$ is now broadened, expressing the induced amorphicity after cycles of heating and cooling. One additional endothermic peak at about 405 $^\circ\text{C}$, corresponding to the melting of $K_3V_5O_{14}$, is noticeable in spent 22KV, being in agreement with the results of XRD and Raman.

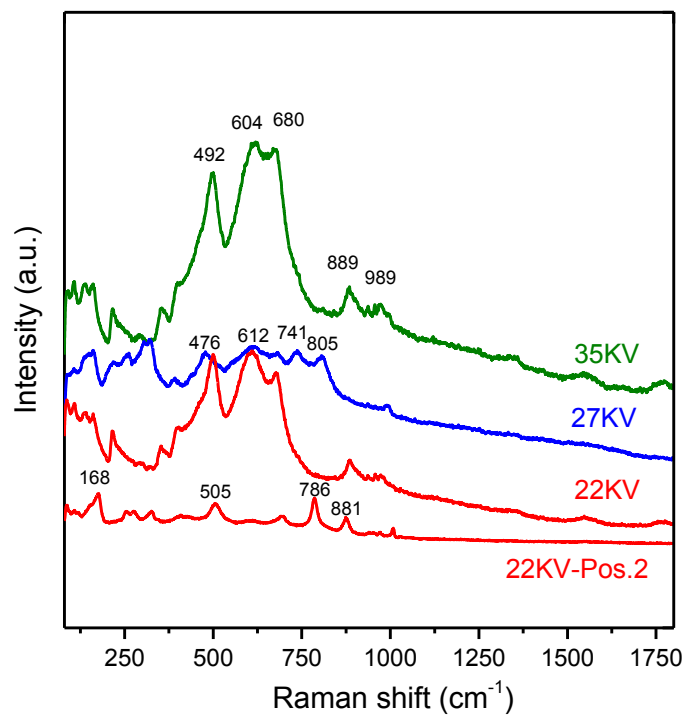


Figure 3.14. Raman spectroscopy of spent xKV catalysts at room temperature after one month time on stream.

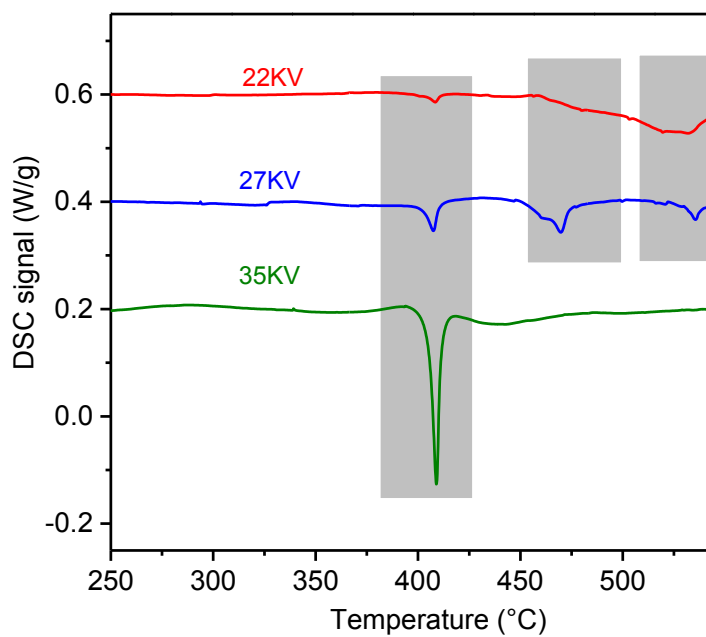


Figure 3.15. DSC profiles of spent xKV catalysts after one month time on stream, heating rate: 10Kpm, under the flow of 70 ml/min 21 % O₂/ 79 % Ar.

To study whether the homogeneity of 35KV is also maintained in the nano-structure, SEM-EDX was performed. Figure 3.16 depicts the SEM images of spent 35KV catalyst. The EDX results of the spent 35KV, visualizing the distribution of K and V in the catalysts, are shown in Figure 3.17. The results are a hint of slight agglomerated and sintered catalyst particles after catalysis, more likely due to several cycles of liquefaction and crystallization.

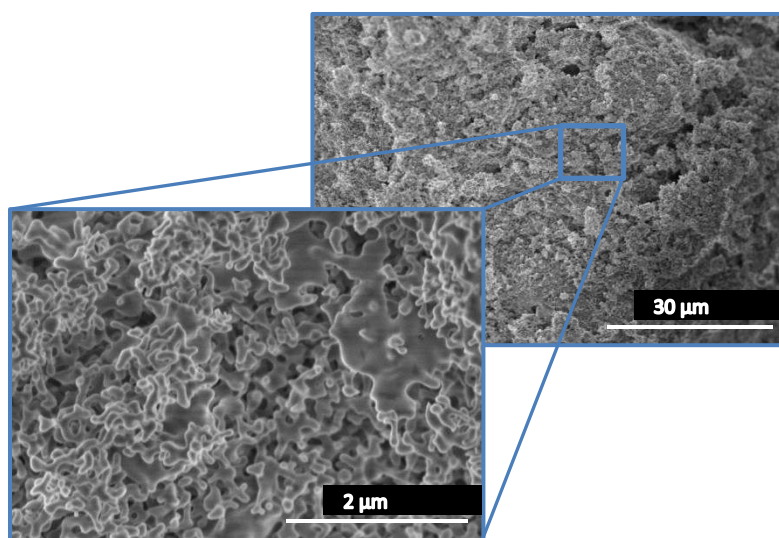


Figure 3.16. SEM of spent catalyst 35KV after one month time on stream.

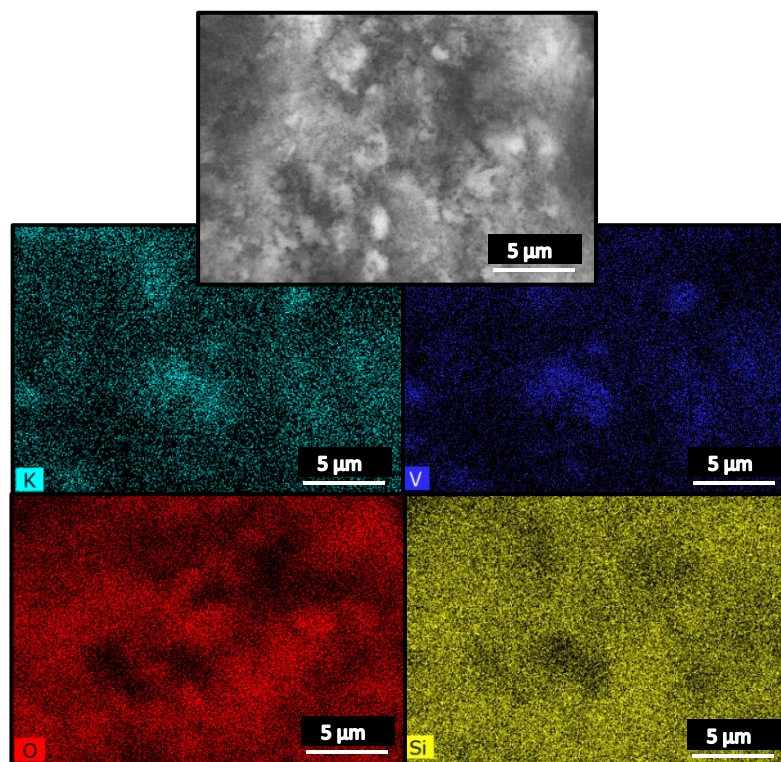


Figure 3.17. SEM image and elemental mappings of spent catalyst 35KV, after one month time on stream.

3.4 In-situ characterizations

Catalyst 35KV remained unchanged with respect to phase composition and morphology over a long time on stream and several heating and cooling cycles. The solid-liquid transformation occurring at the reaction temperatures was studied by high temperature XPS, in-situ Raman, and in-situ UV-Vis spectroscopy. For this purpose catalyst 35KV which has one single melting peak and shows stability has been selected as a simple model catalyst to be investigated in more details.

3.4.1 High temperature XPS

One feasible explanation for increasing the selectivity to propene after melting could be the coverage of active vanadium oxide species by segregation of potassium at the surface of the catalyst during melting or at temperatures close to the melting point. XPS measurements at elevated temperatures were required to investigate this phenomenon further.

Figure 3.18 depicts the V2p and K2p spectra of the catalyst. Vanadium underwent small reduction during the experiment, which is assumed beam induced. The K2p spectra show the two K species, corresponding to potassium silicate and $K_3V_5O_{14}$, as in the fresh catalyst.

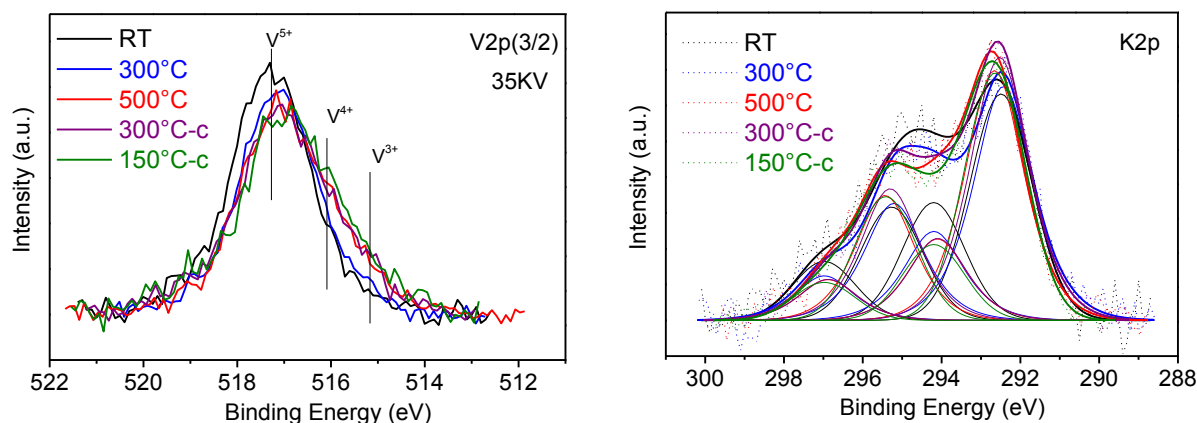


Figure 3.18. V2p(3/2) and K2p core level XPS spectra of catalyst 35KV via heating and cooling.

Table 3.6. The surface-near elemental ratios during heating in XPS cell (small amount of O_2 (2×10^{-8} mbar) was dosed into the UHV chamber during the experiment)

Temperature	V/Si	O/(V+Si)	C/Si	K/Si	V/K
RT					1.22
300 °C	0.0245	2.12	0.04	0.020	1.25
500 °C	0.024	2.0	0.041	0.019	1.25
300 °C_c	0.025	2.05	0.044	0.020	1.25
150 °C_c	0.026	2.03	0.044	0.020	1.32

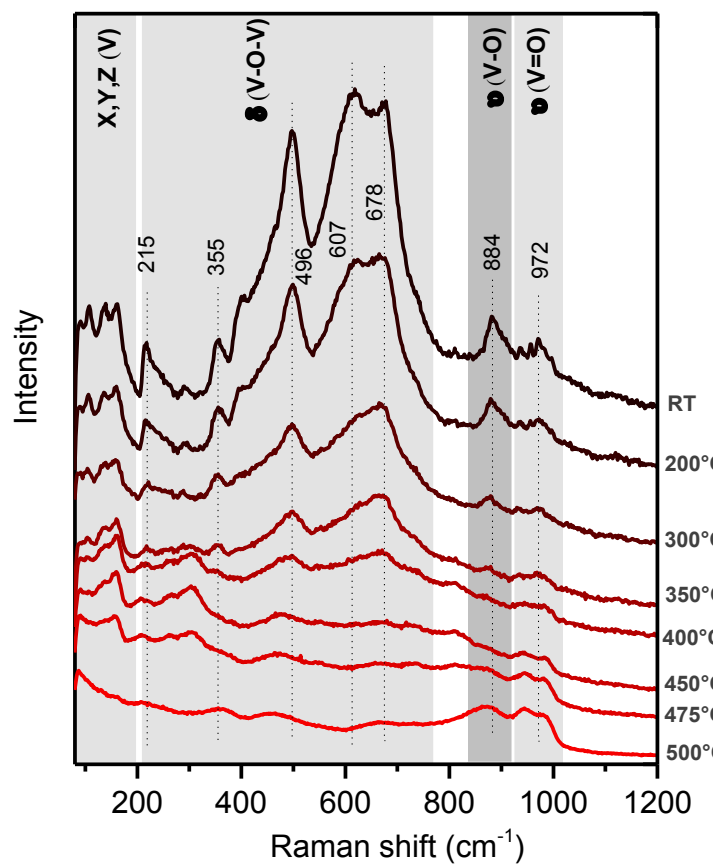
_c: during cooling

Table 3.6 compiles the surface-near elemental ratios during the heating experiment. The surface V/K ratio for the catalyst at room temperature was 1.22, which is lower than the stoichiometric value of 1.67 for $K_3V_5O_{14}$, evidencing potassium enrichment on the surface of the freshly prepared catalyst. The elemental ratios do not change after melting. Therefore, based on high temperature XPS, K segregation upon melting cannot be confirmed. It should be noted that, if the particles are smaller than 2-3 nm, or the active material forms a film on the silica support, any significant change cannot be observed in the surface-near concentration, since the particles are then smaller than the information depth of the experiment.

3.4.2 In-situ Raman

Figure 3.19a shows the in-situ Raman spectra of catalyst 35KV while heating under the ODP reaction conditions from room temperature to 500 °C. The catalytic performance measured by micro-GC at 500 °C for monitoring whether the catalyst is under working conditions (X: 2 %, S: 47 %). All the observed alterations in the Raman spectra of phase pure $K_3V_5O_{14}$ which was measured under the flow of 21 % O_2 in He, are present once again in the spectral features of the supported catalyst. These alterations are described in details in Chapter 2. Shortly, change of relative intensity of bands at 678 cm^{-1} and 611 cm^{-1} and band broadening are observed below the melting point. Temperature dependent intensity of $K_3V_5O_{14}$ vibrational modes during the in-situ experimentation of the catalyst 35KV under the ODP reaction is depicted in Figure 3.20. Starting from 300 °C, which is close to the Tamman temperature, decrease in the intensity of bands is noticeable. The spectra of the catalyst between Tamman temperature and melting point (405 °C) remain mostly unchanged. The Raman spectrum of catalyst in the molten state is compared with that of solid state in Figure 3.21. The spectrum in the molten state is dominated by broad vibrational bands between 800 to 1000 cm^{-1} . As it can be seen from Picture 3.20, the intensity of bands in this region is increasing after melting. These bands are assigned to V-O stretching vibrational in short vanadyl bands at around 980 cm^{-1} and bridging bonds at about 868 cm^{-1} . A comparison of the Raman spectrum of catalyst 35KV at 500 °C with the Raman spectrum of $K_3V_5O_{14}$ in the molten state is shown in Figure 3.22. It is visible that the spectrum of catalyst 35KV is dominated by the Raman modes of $K_3V_5O_{14}$ in the molten state. Catalyst 35KV shows all the Raman features of the fresh catalyst after cooling down to room temperature in the in-situ cell, see Figure 3.19b.

a)



b)

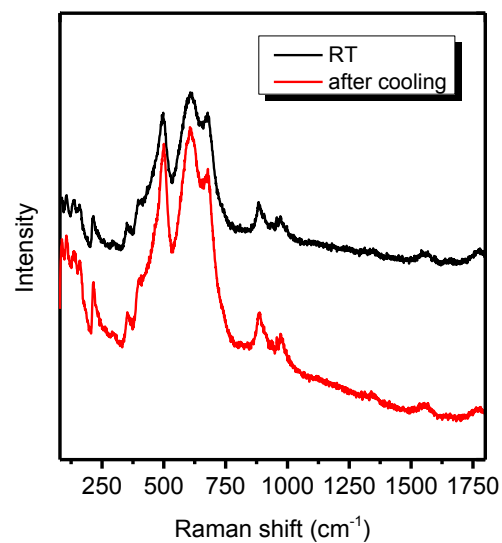


Figure 3.19. In-situ Raman of catalyst 35KV under reaction conditions; feed: $\text{C}_3\text{H}_8:\text{O}_2:\text{He}=7.5:7.5:85$; flow rate 5.5 ml/min; mass of catalyst:40 mg a) Raman spectra via heating, b) comparison of Raman spectra after cooling in-situ cell with fresh catalyst.

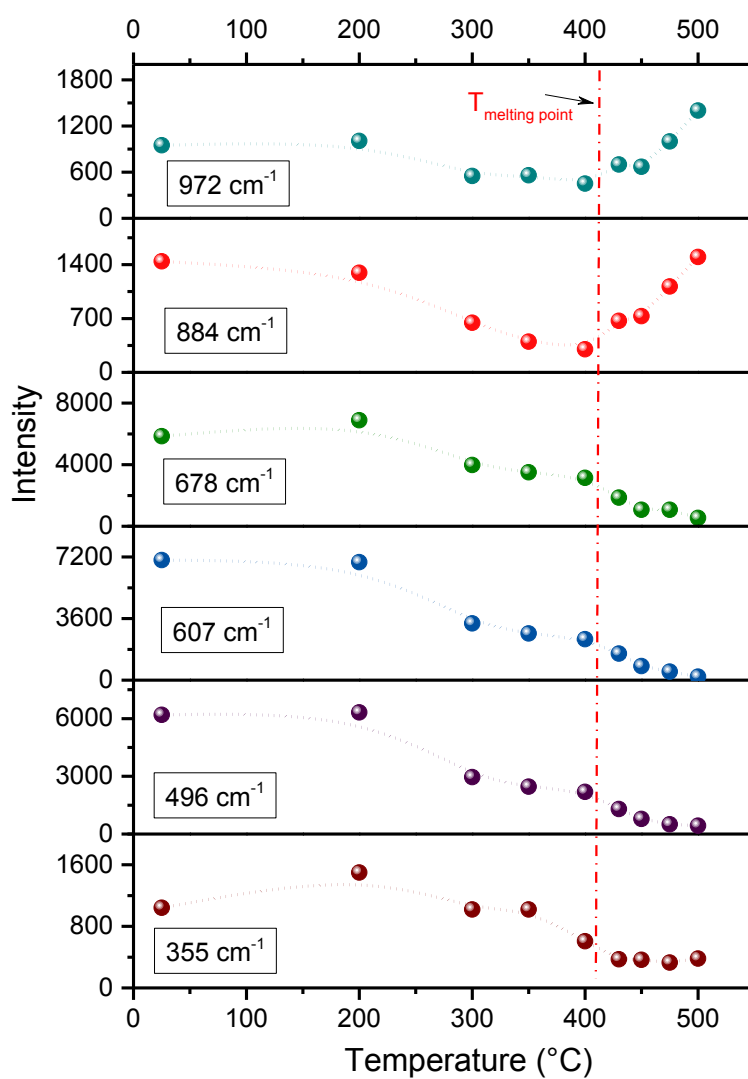


Figure 3.20. Temperature dependent intensity of $K_3V_5O_{14}$ vibrational modes during in-situ experiment of catalysts 35KV under the ODP reaction feed, feed: $C_3H_8:O_2:He$ -7.5:7.5:85; flow rate 5.5 ml/min; mass of catalyst:40 mg.

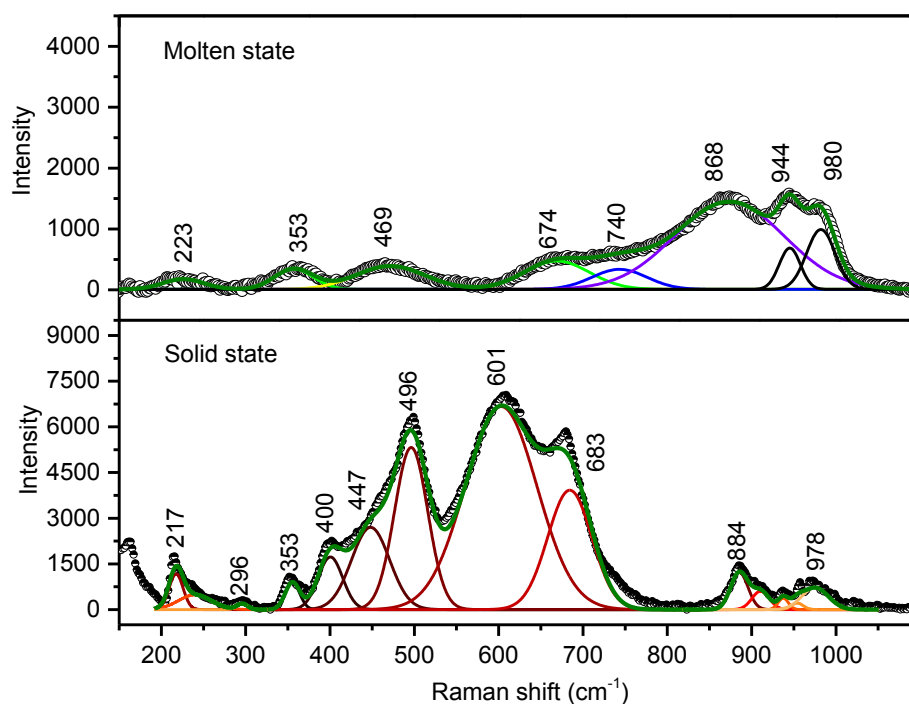


Figure 3.21. Comparison of Raman spectra of 35KV at room temperature with that of 500 °C (molten state) taken under reaction conditions, feed: C₃H₈:O₂:He-7.5:7.5:85; flow rate 5.5 ml/min; mass of catalyst:40 mg.

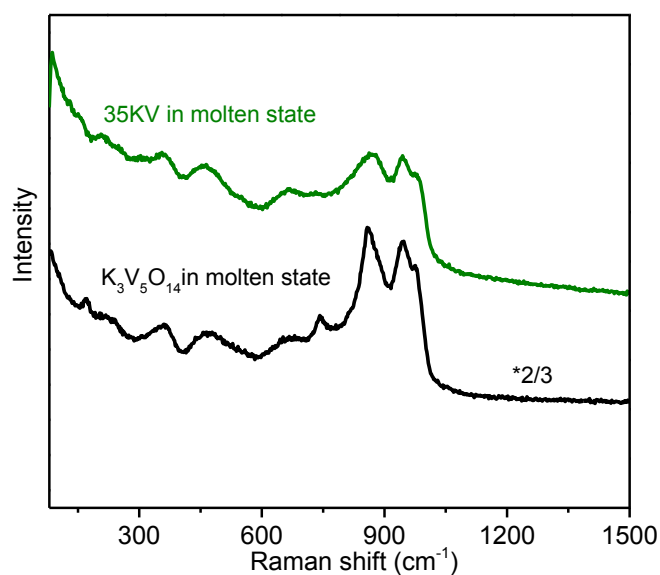
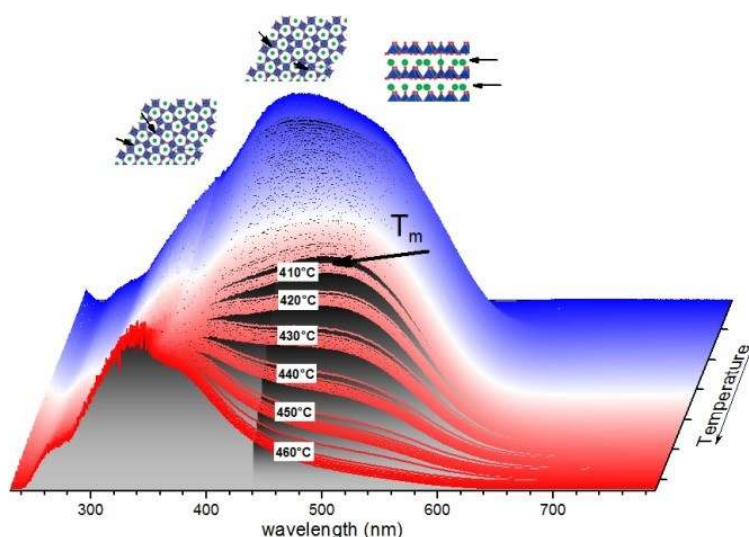


Figure 3.22. Comparison of Raman spectra of K3V5O15 measured in the molten state with that of catalyst 35KV measured after melting under the ODP reaction conditions (feed: C₃H₈:O₂:He-7.5:7.5:85; flow rate 5.5 ml/min; mass of catalyst:40 mg).

3.4.3 In-situ UV-Vis spectroscopy

The room-temperature UV-Vis spectrum of catalyst 35KV is dominated by the spectral features of $K_3V_5O_{14}$. This is consistent with the results of XRD, as $K_3V_5O_{14}$ was the only phase detected beside amorphous SiO_2 . The electronic structure of $K_3V_5O_{14}$ is unknown. Therefore, detailed assignment of the bands in the solid state is not possible. A rough assignment of bands is done in Chapter 2. Nearly no absorption band in the region of 600-800 nm, related to d-d transitions of V^{4+} ²⁸, is seen. Since the d-d transitions are 10-30 times weaker than charge transfer transitions²⁹, they may be covered by the intense charge transfer absorption bands. But, as the results of XPS also confirmed the presence of V^{5+} , contributions of V^{4+} could be excluded.

a)



b)

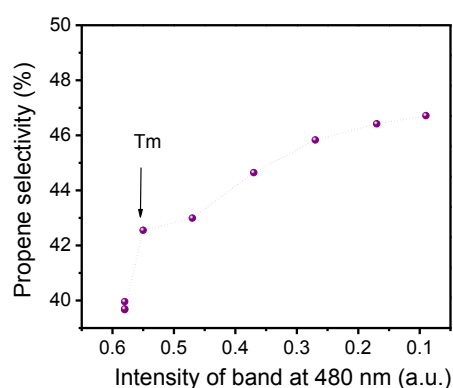


Figure 3.23. In-situ UV-Vis spectroscopy of catalyst 35KV under the ODP reaction conditions, feed: $C_3H_8:O_2:He$ 7.5:7.5:85; flow rate 2 ml/min; mass of catalyst:10 mg a) UV-Vis spectra via heating b) Correlation of the reaction data taken from in-situ UV-Vis cell and intensity of UV-Vis spectra at 480 nm.

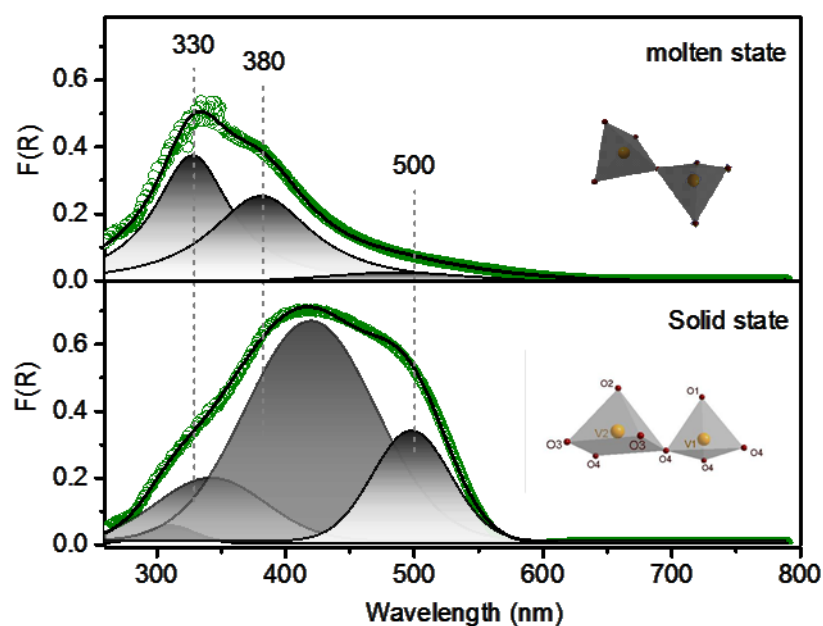


Figure 3.24. Deconvolutions of UV-Vis spectra in the solid and molten states under ODP reaction conditions.

Structural transformations in terms of the coordination of vanadium atoms in the catalyst below and above the melting point were monitored by in-situ UV-Vis spectroscopy. Catalytic and spectroscopic results simultaneously recorded in the UV-Vis cell are shown in Figure 3.23. To facilitate comparison of the spectrum at room temperature with that in the molten state, the observed bands are deconvoluted for both states in Figure 3.24. With increasing temperature and crossing the melting point a component at 500 nm in the spectrum of the catalyst disappears. The one at 330 nm remains almost constant. The changes in the spectra are explained by conversion from five-fold to four-fold coordinated vanadium due to decomposition of the layered structure and partial breaking of bridging V-O-V bonds during melting, in agreement with Raman spectra. Based on the results of UV-Vis spectroscopy it is evident that a change in the coordination environment of vanadium after reaching the melting point is correlated to the observed changes in the catalytic performance in terms of selectivity (see Figure 3.23b).

The d-d transitions of the reduced vanadia cations are barely detectable, suggesting that vanadium remains fully oxidized under the applied conditions. It is worth to mention that

$K_3V_5O_{14}$ showed reversible melting and crystallization during in-situ UV-Vis spectroscopy (see supporting information Figure S3.2 for the cooling cycle).

3.5 Discussion

The XRD patterns of the prepared catalysts did not show any peak related to V_2O_5 , but different potassium vanadate species. However, the detection limit of XRD is not enough for detecting nano-crystalline V_2O_5 . Based on Raman spectroscopy V_2O_5 nano-crystals can be clearly excluded. We do not detect any sign of dispersed vanadium oxide species due to the absence of the Raman band at about 1015-1045 cm^{-1} .

As evidenced by DSC results, $K_3V_5O_{14}$ melts in the air between 405 to 413 °C both as the pure substance and supported on silica. Comparison of enthalpy of melting for pure $K_3V_5O_{14}$ and supported one indicated that the major part of Vanadium is in the potassium vanadate structure, in agreement with the Raman spectrum. Temperature dependent XRD and DSC confirm that a supported liquid phase is formed at temperatures above 400 °C for catalyst 35KV. Regarding catalyst 27KV contribution of the small portion of solid phase beside the molten layer above 450 °C is expected. Catalyst 22KV, due to the clear phase change in the spent catalyst is difficult to discuss here as the model catalyst. The latter two catalysts show irreversible structural changes during catalysis. Only catalyst 35KV is characterized by a reversible behavior. Therefore the following discussion of the influence of phase transition on catalytic properties is limited to catalyst 35KV.

The catalytic test in a fixed bed reactor exhibits an increase in selectivity towards propene by 30-40 % after phase transition from solid to liquid at comparable conversion (approximately 10-15 %). Since the relatively high content of alkali is applied for preparation of the catalysts, the change in the performance is attributed to structural changes rather than suppression of surface acidity.³⁰ Therefore, the low selectivity of propene at temperatures below the melting point is attributed to the presence of crystalline potassium vanadate, which resembles the crystal structure of V_2O_5 .

The decrease in activity above the melting point could be related to a decrease in the surface area. In addition, as demonstrated by Amakawa et al.⁸ strain at the anchoring bonds can induce higher activity for supported catalysts. In accordance with that, lower activity of

molten layer could be due to the presence of equilibrated species in comparison to the more rigid structure of solids.

Interestingly, the catalyst 35KV that contains the active surface layer in the form of a complete liquid film under reaction conditions shows a constant or slightly increased selectivity to propene with increasing conversion (Figure 3.9 curve marked with L). The selectivity is higher than silica supported vanadium monolayer catalysts.

Since propane can undergo consecutive reactions, decrease in selectivity to propene with increasing conversion is expected. It has been proposed in the literature that the molten layer may play the role of a radical initiator.³¹ If so, then the catalyst will generate the alkyl fragments that are then transformed to olefins in the gas phase. In order to get higher selectivity re-adsorption of the formed radicals needs to be suppressed. However, the similar apparent activation energies measured in solid and molten states do not support significant changes in the reaction mechanism.

Increasing selectivity with increasing temperature, at comparable conversion, has been reported for supported vanadia catalysts.³² Consecutive reaction of propene to total combustion products is more favorable at lower temperatures. The reason is attributed to the higher activation energy needed for activation of propane compared to propene. Therefore, the contribution of the higher temperature to the superior selectivity of the catalyst should be taken into account. In this respect, investigation of the SLP catalyst in the super-cooled state would be informative for distinguishing the influence of temperature and the effect of liquefaction. However, the local structure of liquid in terms of short-range ordering could also change by temperature. An increase in density and more ordered liquid at lower temperatures has been demonstrated previously for Zr-Pd eutectic system.³³

The V/K ratio of 1.33 determined by XPS analysis of catalyst 35KV indicates a slight enrichment of potassium on the surface. The ratio does not change significantly with increasing the temperature verifying that K is not lost. It should be emphasized that increasing the mobility of potassium after the melting point can also influence the selectivity. XPS analysis is not helpful in this respect, since a thin layer is formed on the surface with a thickness lower than the information depth.

One experimentally supported reason for the higher selectivity of the molten layer is regarding the observed kinetic effects. Based on previous studies, comparison of O_2 and N_2O as oxidants in ODP reaction has demonstrated that slower re-oxidation of active site can end up with higher selectivity. The observed decrease in selectivity by increasing activity was also inferior when N_2O applied as the oxidant.³⁴ Considering the explained observation, the superior selectivity of the liquid layer could be related to the slower re-oxidation rate calculated for the liquid state.

Structural transformations in terms of coordination of vanadium atoms in the catalyst above the melting point were monitored by in-situ UV-Vis spectroscopy and Raman spectroscopy. The comparison studies demonstrate that the structural properties of supported metal oxides, having 2D or 3D species, dominate their catalytic performance.^{1, 3, 4, 35-41} Besides, It should be emphasized that the site isolation principle⁴², which could also happen after melting by breaking of bridging bonds, as it is evidenced in this study by in-situ UV-Vis spectroscopy, could also play a role for SLP catalysts. In-situ studies under the operation of the catalysts by UV-Vis spectroscopy revealed an increase in selectivity to propene at constant propane conversion by changing the coordination environment of vanadium from the pentagonal pyramidal (or pseudo-octahedral) into the tetrahedral coordination due to the transformation of a supported solid into a supported liquid phase. Tetrahedral coordination of vanadium in the melt is confirmed by losing the intensity of the band at the higher wavelength in UV-Vis spectra and vanishing the vibrational modes of V-O long bands in Raman spectra taken in the molten state. Vanadium tetrahedra which are partially corner linked could be proposed as possible units in the molten potassium vanadate. Transformation of vanadium from the pseudo-octahedral environment to tetrahedral environment after reaching the melting point was previously reported for V_2O_5 .⁴³ In that study, pair distribution function determined applying x-ray and neutron diffraction data has been applied for proposing possible clusters in molten V_2O_5 . The unselective behavior of potassium vanadates is most likely due to the presence of V-O-V chains. The phase transition from solid to liquid can break up the V-O-V chains, observed in in-situ Raman, consequently creating smaller and especially isolated V-O domains on the surface.

3.6 Conclusion

The influence of phase transition from solid to liquid on the performance of supported potassium vanadates in terms of decrease in activity but increase in selectivity at comparable conversions has been demonstrated. On the basis of data from this study, it can be concluded that both polymeric vanadates and monomeric vanadyls are active although the monomeric structure which grows up after the melting point is more selective. The experiments indicate that the transformation of a supported phase from solid to liquid has a positive impact on the catalytic performance in terms of selectivity to propene due to structural changes in the local coordination around the vanadium atom highlighting the potential of SLP catalysts in selective oxidation of alkanes. Lower strain, which is expected after the liquefaction, a decline in coordination number demonstrated by UV-Vis spectroscopy and Raman, and consequently, slower re-oxidation rate, calculated by kinetic investigations, are proposed as the key factors in high selectivity of the liquid layer.

The performed study could be used as a concept for applying a rather new area of catalysts, so called SLP catalysts, in oxidative dehydrogenation of lower alkanes.

Acknowledgments

This research was conducted in the framework of the BasCat, collaboration between BASF SE, TU Berlin, FHI, and the cluster of excellence “Unified Concepts in Catalysis” (UniCat, www.unicat.tu-berlin.de). We thank Maike Hashagen, Jasmin Allan and Dr. Olaf Timpe for technical assistance.

3.7 Bibliography

1. F. Cavani, N. Ballarini and A. Cericola, *Catalysis Today*, 2007, **127**, 113-131.
2. T. Blasco and J. M. L. Nieto, *Appl Catal A Gen*, 1997, **157**, 117-142.
3. G. C. Bond and S. F. Tahir, *Applied Catalysis*, 1991, **71**, 1-31.
4. C. A. Carrero, R. Schloegl, I. E. Wachs and R. Schomaecker, *ACS Catalysis*, 2014, **4**, 3357-3380.
5. X. Li, T. Lunkenbein, V. Pfeifer, M. Jastak, P. K. Nielsen, F. Girgsdies, A. Knop-Gericke, F. Rosowski, R. Schlögl and A. Trunschke, *Angewandte Chemie International Edition*, 2016, **55**, 4092-4096.
6. L. Masliuk, M. Heggen, J. Noack, F. Girgsdies, A. Trunschke, K. E. Hermann, M. G. Willinger, R. Schlögl and T. Lunkenbein, *To be submitted*.
7. H. Bluhm, M. Hävecker, E. Kleimenov, A. Knop-Gericke, A. Liskowski, R. Schlögl and D. S. Su, *Top Catal*, 2003, **23**, 99-107.
8. K. Amakawa, L. L. Sun, C. S. Guo, M. Havecker, P. Kube, I. E. Wachs, S. Lwin, A. I. Frenkel, A. Patlolla, K. Hermann, R. Schloegl and A. Trunschke, *Angewandte Chemie-International Edition*, 2013, **52**, 13553-13557.
9. S. Boghosian, F. Borup and A. Chrissanthopoulos, *Catal Lett*, 1997, **48**, 145-150.
10. G. E. Folkmann, K. M. Eriksen, R. Fehrmann, M. Gaune-Escard, G. Hatem, O. B. Lapina and V. Terskikh, *The Journal of Physical Chemistry B*, 1998, **102**, 24-28.
11. G. E. Folkmann, G. Hatem, R. Fehrmann, M. Gaune-Escard and N. J. Bjerrum, *Inorg Chem*, 1991, **30**, 4057-4061.
12. O. B. Lapina, B. S. Bal'zhinimaev, S. Boghosian, K. M. Eriksen and R. Fehrmann, *Catalysis Today*, 1999, **51**, 469-479.
13. K. Nielsen, R. Fehrmann and K. M. Eriksen, *Inorg Chem*, 1993, **32**, 4825-4828.
14. V. I. Pârvulescu, C. Paun, V. Pârvulescu, M. Alifanti, I. Giakoumelou, S. Boghosian, S. B. Rasmussen, K. M. Eriksen and R. Fehrmann, *Journal of Catalysis*, 2004, **225**, 24-36.
15. B. Tope, Y. Zhu and J. A. Lercher, *Catalysis Today*, 2007, **123**, 113-121.
16. C. P. Kumar, S. Gaab, T. E. Muller and J. A. Lercher, *Top Catal*, 2008, **50**, 156-167.
17. B. Tope, Y. Zhu and J. A. Lercher, *Catalysis Today*, 2007, **123**, 113-121.
18. J. B. Branco, G. Lopes and A. C. Ferreira, *Catal Commun*, 2011, **12**, 1425-1427.
19. N. Hiyoshi and T. Ikeda, *Fuel Process. Technol.*, 2015, **133**, 29-34.
20. F. Holtzberg, A. Reisman, M. Berry and M. Berkenblit, *Journal of the American Chemical Society*, 1956, **78**, 1536-1540.
21. J. J. Yeh and I. Lindau, *Atomic Data and Nuclear Data Tables*, 1985, **32**, 1-155.
22. X. G. Kong, Z. L. Guo, P. H. Wen, J. F. Huang, L. Y. Cao, L. X. Yin, J. Y. Li and Q. Feng, *Crystengcomm*, 2015, **17**, 3777-3782.
23. L. F. Bai, Y. Xue, J. J. Zhang, B. C. Pan and C. Z. Wu, *Eur J Inorg Chem*, 2013, **2013**, 3497-3505.
24. P. Kube, B. Frank, S. Wrabetz, J. Kröhnert, M. Hävecker, J. Velasco-Vélez, J. Noack, R. Schlögl and A. Trunschke, *ChemCatChem*, 2017, **9**, 573-585.
25. C. P. Kumar, S. Gaab, T. E. Müller and J. A. Lercher, *Top Catal*, 2008, **50**, 156-167.
26. P. Gruene, T. Wolfram, K. Pelzer, R. Schlögl and A. Trunschke, *Catalysis Today*, 2010, **157**, 137-142.

27. R. Baddour-Hadjean, A. Boudaoud, S. Bach, N. Emery and J. P. Pereira-Ramos, *Inorg Chem*, 2014, **53**, 1764-1772.
28. G. Catana, R. R. Rao, B. M. Weckhuysen, P. Van Der Voort, E. Vansant and R. A. Schoonheydt, *The Journal of Physical Chemistry B*, 1998, **102**, 8005-8012.
29. C. M. Chanquia, A. L. Canepa, E. L. Winkler, E. Rodriguez-Castellon, S. G. Casuscelli and G. A. Eimer, *Mater Chem Phys*, 2016, **175**, 172-179.
30. F. Amano, T. Yamaguchi and T. Tanaka, *Catalysis Today*, 2007, **120**, 126-132.
31. C. A. Gärtner, A. C. van Veen and J. A. Lercher, *ChemCatChem*, 2013, **5**, 3196-3217.
32. A. Dinse, B. Frank, C. Hess, D. Habel and R. Schomäcker, *J. Mol. Catal. A Chem.*, 2008, **289**, 28-37.
33. N. A. Mauro, W. Fu, J. C. Bendert, Y. Q. Cheng, E. Ma and K. F. Kelton, *The Journal of Chemical Physics*, 2012, **137**, 044501.
34. X. Rozanska, E. V. Kondratenko and J. Sauer, *Journal of Catalysis*, 2008, **256**, 84-94.
35. J. T. Grant, C. A. Carrero, A. M. Love, R. Verel and I. Hermans, *Acs Catalysis*, 2015, **5**, 5787-5793.
36. I. E. Wachs, *Catalysis Today*, 2005, **100**, 79-94.
37. H. Eckert and I. E. Wachs, *MRS Proceedings*, 2011, **111**.
38. H. Eckert and I. E. Wachs, *The Journal of Physical Chemistry*, 1989, **93**, 6796-6805.
39. T. Tanaka, H. Yamashita, R. Tsuchitani, T. Funabiki and S. Yoshida, *Journal of the Chemical Society, Faraday Transactions 1: Physical Chemistry in Condensed Phases*, 1988, **84**, 2987-2999.
40. I. E. Wachs, J.-M. Jehng, G. Deo, B. M. Weckhuysen, V. V. Gulians, J. B. Benziger and S. Sundaresan, *Journal of Catalysis*, 1997, **170**, 75-88.
41. C. Zhao and I. E. Wachs, *Catalysis Today*, 2006, **118**, 332-343.
42. R. K. Grasselli, *Top Catal*, 2001, **15**, 93-101.
43. S. i. Takeda, M. Inui, Y. Kawakita, K. Maruyama, S. Tamaki, K. Sugiyama and Y. Waseda, *Physica B: Condensed Matter*, 1995, **213**, 499-501.

3.8 Appendix

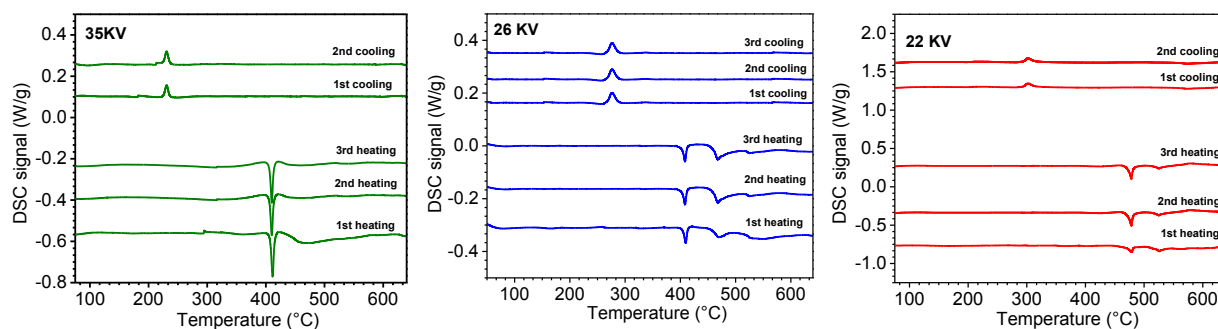


Figure S 3.1. Differential scanning calorimetry (DSC) of Aerosil supported catalysts at heating rate of 10Kpm and cooling rate of 5Kpm.

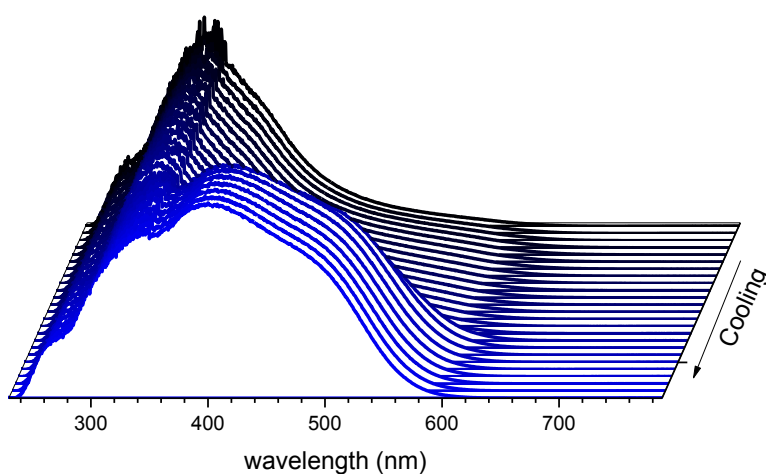


Figure S 3.2. In-situ UV-Vis spectroscopy of catalyst 35KV via cooling under the ODP reaction conditions, feed: C₃H₈:O₂:He 7.5:7.5:85; flow rate 2 ml/min; mass of catalyst:10 mg.

4 In-situ formation of potassium doped vanadium monolayer on silica applying thermal spreading method

4.1 Introduction

Preparation of supported vanadia monolayer catalysts has been the scope of various studies,^{1, 2} with the aim of preventing the presence of crystalline V_2O_5 , to suppress deep oxidation of alkanes. Several preparation methods such as impregnation, grafting, chemical vapor deposition, co-precipitation and thermal spreading have been applied to reach the monolayer coverage.¹⁻³ Beside preparation techniques, adding alkaline-earth metal ions was also shown to be beneficial for dispersing the polymeric species.^{4, 5} Introducing alkali in the supported vanadia causes structural changes via elongation and as a result weakening of terminal V=O bonds.⁶⁻¹³ The effect of additives in terms of increasing basicity of active center has been also discussed before.^{9, 14, 15} It is more difficult to adsorb an olefin (as a base) on a basic surface than an acidic one.¹⁶ The environment of the metal oxygen bond can change the degree of polarization and consequently the oxygen will exhibit either more electrophilic or more nucleophilic properties. Nucleophilic oxygen will favor dehydrogenation reactions by forming OH groups.¹⁷ In general, for the active center to be more selective higher electron density would be necessary. Theoretical calculations demonstrated that the potassium cation can not only transfer its electron to neighboring oxygen anions but also to the vanadyl group which cause it to be one of the best additives.¹⁶

Consequently, alkali doping is known to be acting in favor of selectivity. Supported potassium vanadate phases, however, might be present in addition to dispersed vanadium oxide species.^{5, 18}

In this study, therefore, we follow a bottom-up approach starting with synthesizing potassium vanadate phases supported on silica. This research study is intended to study the catalytic properties of these phases when dispersed on a support.

In the literature, the K/V ratio was varied more freely for alumina (K/V: 0-0.25)¹⁹ or titania (K/V: 0-1.5)^{5, 20} supported catalysts. In the case of silica supported catalysts, however, lower content of potassium (K/V: 0.1) was applied.^{21, 16, 22}

In the present work, the phase diagram of $K_2O-V_2O_5$ ²³ has been used to find the proper composition of catalysts. The samples with a K content from zero to 18 atomic percent in the coating will be discussed here. Applying higher K content which results in presence of molten phase under the reaction conditions were investigated in a separate study (see Chapter 3). The catalysts were characterized applying XRF, XRD, DSC, SEM, EDX and XPS. Temperature dependent XPS and XRD, and in-situ characterizations applying Raman, and UV-Vis spectroscopy with simultaneous gas-phase monitoring were performed to analyze the impact of the presence of crystalline phases on catalytic properties in the oxidative dehydrogenation of propane.

4.2 Experimental

4.2.1 Preparation

Catalysts with varying K/V ratio in the coating and nominal loading of 10 wt % were synthesized using K_2CO_3 (Merck), V_2O_5 (BASF), Aerosil 300 (Dequssa), and applying the thermal spreading method. To do so, water slurries of K_2CO_3 , V_2O_5 and Aerosil with a systematic variation of potassium and vanadium content were prepared. Based on the phase diagram of $K_2O-V_2O_5$ ²³, the mole percentage of K_2CO_3 at the intervals of 20-0 which gives catalysts that remain solid under the reaction temperature was the region of interest. The pure V/Aerosil and K/Aerosil catalysts were also prepared as references. The slurries were spray dried in a Büchi mini spray dryer with the inlet temperature of 200 °C and the outlet temperature of 130 °C. The obtained powders were calcined at 700 °C which is above the expected melting point for the coating phases. The calcination was done in 21 % $O_2/79$

% Ar for 16 hours in a rotating quartz tube. In addition, $K_2V_8O_{21}$ was also prepared as reference. A detailed description of the synthesis is given elsewhere (Chapter 2).

The catalysts are denoted further in the text by the symbols xKV, where x corresponds to the experimental atomic percentage of K in the coating determined by XRF. For instance the catalyst denoted 15KV contains 15 mol% K_2O and 85 mol% V_2O_5 deposited on Aerosil support. V/Aerosil and K/Aerosil are labeled as 100V and 100K, respectively.

4.2.2 Characterization

X-ray Fluorescence (XRF)

The amount of potassium, vanadium and silicon in the prepared catalysts was determined by X-ray fluorescence analysis (XRF). The catalysts and corresponding standards were mixed with lithiumtetraborate flux (FX-X100, Fluxana) and fused in a Vulcan Fusion Machine (HD Electronic & Elektrotechnik GmbH) under formation of flat molten glass discs, which were analyzed by X-Ray Fluorescence spectroscopy applying the spectrometer Pioneer S4 (Bruker AXS GmbH). The XRF instrument was wavelength dispersive and equipped with a Rh-anode.

X-ray Diffraction (XRD)

The X-ray diffraction (XRD) measurements were performed in Bragg-Brentano geometry on a Bruker AXS D8 Advance II theta/theta diffractometer, applying Ni filtered $Cu\ K\alpha$ radiation and a position sensitive energy dispersive LynxEye silicon strip detector. The catalyst powder was filled into the recess of a cup-shaped catalyst holder, the surface of the powder bed being flush with the catalyst holder edge (front loading). The in situ XRD data were collected on a STOE Theta/theta X-ray diffractometer ($CuK\alpha$ radiation, secondary graphite monochromator, scintillation counter) equipped with an Anton Paar XRK 900 in-situ reactor chamber with the gas feed flowing from the top to the bottom of the chamber. The temperature was measured by two type K thermocouples. While the first one (TC1) was in close contact to the catalyst bed, the second thermocouple (TC2) was situated near the entrance of the gases.

BET

Surface areas of the catalysts were analyzed by nitrogen adsorption (Autosorb AS-6B, Quantachrome) after a pretreatment at 150 °C for 1 h in vacuum. The specific surface areas were determined according to the Brunauer–Emmett–Teller (BET) method using 11 data points in the relative pressure p/p_0 range of 0.05–0.3.

Differential Scanning Calorimetry (DSC)

Calorimetric experiments were carried out on a Mettler-Toledo HP DSC 827 calorimeter, with Au–AuPd Sensor, in an Alumina crucible in a dynamic 21 % O₂/ 79 % Ar (70 ml/min) flow with 10 Kpm heating rate and 5 Kpm cooling rate. Temperatures were calibrated against the melting points of In and Zn.

Scanning Electron Microscopy (SEM) and Energy-Dispersive X-ray Spectroscopy (EDX)

The SEM images were captured on a Hitachi S-4800 Field Emission Scanning Electron Microscope, working in the kV range 0.1 to 30. Morphology studies were undertaken at a voltage of 1.5 kV and a relatively close working distance of 3mm. The Energy Dispersive X-ray Analysis Data were detected with Bruker EDX System applying a SDD (silicon drift detector) Detector. The working distance for detecting x-rays is, in our case, optimized to 10mm.

X-ray Photoelectron Spectroscopy (XPS)

All catalysts were investigated as pressed pellets. Spectra were recorded at room temperature, using non-monochromatized Al K α (1486.6 eV) excitation and a hemispherical analyzer (Phoibos 150, SPECS). The correction for charging effects was carried out by internal referencing the Si2p peak of SiO₂ to 103.3 eV. The level of charging was in the range of 3.9-4.9 eV. To calculate the elemental composition, theoretical cross sections from Yeh and Lindau²⁴ have been applied. Additional experiments were performed to assess the surface state and composition at various temperatures. Since V was expected to undergo reduction in UHV during heating, very small amount of O₂ (2x10⁻⁸ mbar) was dosed into the UHV chamber during the experiment to at least partially counteract the reduction. Since the magnitude of charging was changing during high temperature measurements, the referencing to Si2p did not work very well. For V2p, instead, the O1s spectrum was fitted, which was recorded together with V2p in one scan, to extract the O1s binding energy of the K_xV_yO_z, under the assumption that this should be at 530 eV. Then the V2p was shifted accordingly, and these V2p(3/2) spectra were plotted.

Raman spectroscopy

Raman measurements were conducted applying a 532 nm, 50 mW DPSS Laser (Cobolt 05-01 series) and a TriVista Raman Microscope System (TriVista TR 557, S&I GmbH) equipped with a CCD camera (Spec10: 100BR, Princeton Instruments) applying a 10X Objective resulting in a laser power of 2 mW at catalyst position. For spectrometer frequency calibration a silicon

wafer ($520.7 \pm 0.5 \text{ cm}^{-1}$) was applied. The in-situ reaction cell was a CCR 1000 cell from Linkam with the feed flowing from the top to the bottom of the chamber. The gas feed was mixed by means of Bronkhorst mass flow controllers, using helium as inert balance gas. The effluent gas composition was monitored with a micro-GC (Agilent) connected to the outlet of the cell. The Linkam cell was modified to accurately measure the temperature close to the surface of the catalyst sample by installing a second thermocouple.

UV-Vis spectroscopy

UV-Visible diffuse reflectance spectra were measured on a Cary 5000 spectrometer (Agilent) equipped with a Harrick Praying Mantis™ diffuse reflectance attachment (DRP-P72) and a reaction chamber (HVC-VUV). All data were obtained in % reflectance and then converted to the Kubelka-Munk function. Spectralon was loaded into the reaction chamber to collect a baseline spectrum in the range between 1000 and 200 nm. To elucidate the change of vanadium environment due to adsorption of water, the experiments have been done after one step of pretreatment under the flow of synthetic air at 350 °C for 0.5 hours. The reaction gas feed was mixed by means of mass flow controllers (Bronkhorst), using helium as inert balance gas. The effluent product gas composition was monitored with a micro-GC (Agilent). The temperature was raised stepwise with a rate of 5Kpm and the spectra and catalytic data were collected after stabilization of the temperature. Once the catalyst reached the desired temperature, spectra were collected every 3 minutes until changes were no longer observed.

Activity test

The catalytic activities of catalysts were tested in the oxidative dehydrogenation of propane in an eight-fold parallel reactor set-up (Integrated Lab Solutions, Berlin, Germany). The prepared catalysts were first pressed, then crushed in a mortar, and finely sieved to have a particle size of 200 - 355 μm . The temperature range applied for the reaction was between 375 °C to 500 °C. The feed composition of C_3H_8 , O_2 , and N_2 in a molar ratio of 7.5:7.5:85 has been applied. Reactants and products were analyzed by online gas chromatography (Agilent 7890). The conversion and selectivity were calculated based on the number of carbon atoms and the products found. Propene, carbon monoxide, and carbon dioxide were found to be the main reaction products. The amount of oxygenates was below 1 % of the total amount of products. The propane conversion on pure Aerosil support and K/Aerosil (100K) was below 3 % up to 500 °C.

4.3 Results

4.3.1 Physical and chemical properties of prepared catalysts

Table 4.1. Physical and chemical properties of prepared catalysts

Catalyst number	ID	Temperature of calcination (°C)	Atomic ratio (K:V)	Metal oxide loading ^a (wt %)	BET (m ² /g)	XRD expected phases ^c	XRD observed phases
24679	18KV	700	18:82	9	15	$K_2V_8O_{21'}$ V_2O_5	$K_2V_8O_{21'}$ unknown phase ^b
22200	15KV	700	15:85	8.4	15	$K_2V_8O_{21'}$ V_2O_5	$K_2V_8O_{21}$
24660	13KV	700	13:87	9.6	23	$K_2V_8O_{21'}$ V_2O_5	$K_2V_8O_{21}$
24639	11KV	700	11:89	9,8	24	$K_2V_8O_{21'}$ V_2O_5	$K_2V_8O_{21'}$, V_2O_5
22214	7KV	700	7:93	8.8	27	$K_2V_8O_{21'}$ V_2O_5	V_2O_5
22665	100V	700	0:100	9.5	44	V_2O_5	V_2O_5

^aanalyzed by XRF, based on $V_2O_5+K_2O$

^bsimilar to $K_2V_6O_{16} \cdot 1.5 H_2O$

^caccording to phase diagram²³

To examine the content of K and V in the prepared catalysts, XRF analysis was applied. The obtained chemical compositions are listed in Table 4.1 In the performed XRF analysis, the loading of catalysts was calculated based on the sum of K_2O and V_2O_5 in the coating, which scatters around 9. The specific surface area of the catalysts was determined applying the BET method. A notable decrease in BET surface area has been observed for all samples, in particular the potassium containing samples. The values of the specific surface area are smaller for high K content catalysts. The XRD patterns of the fresh catalysts are presented in Figure 4.1. The results demonstrate that SiO_2 exists mostly amorphous. However, by increasing the content of alkali in catalysts 15KV and 18KV minor contribution of cristoblite like phase, peak at 21.8° , is also noticeable. Table 4.3.1 summarizes the present phases of the freshly prepared catalysts. V_2O_5 and $K_2V_8O_{21}$, based on the XRD results, are the main phases present. XRD of the catalyst with the lowest potassium content reveals presence of V_2O_5 as the only detectable crystalline phase. The amount of V_2O_5 is decreasing by increasing the K content and instead of that $K_2V_8O_{21}$ is developing on the surface of support. Crystalline V_2O_5 was not observed by XRD in the catalysts with higher K content, 15KV and

18KV, in contrast to the phase diagram of bulk mixtures of V_2O_5 and potassium carbonate reported in the literature.²³ In the case of catalyst 18KV a new phase with a XRD pattern similar to $K_2V_6O_{16} \cdot 1.5 H_2O$ was also detected.

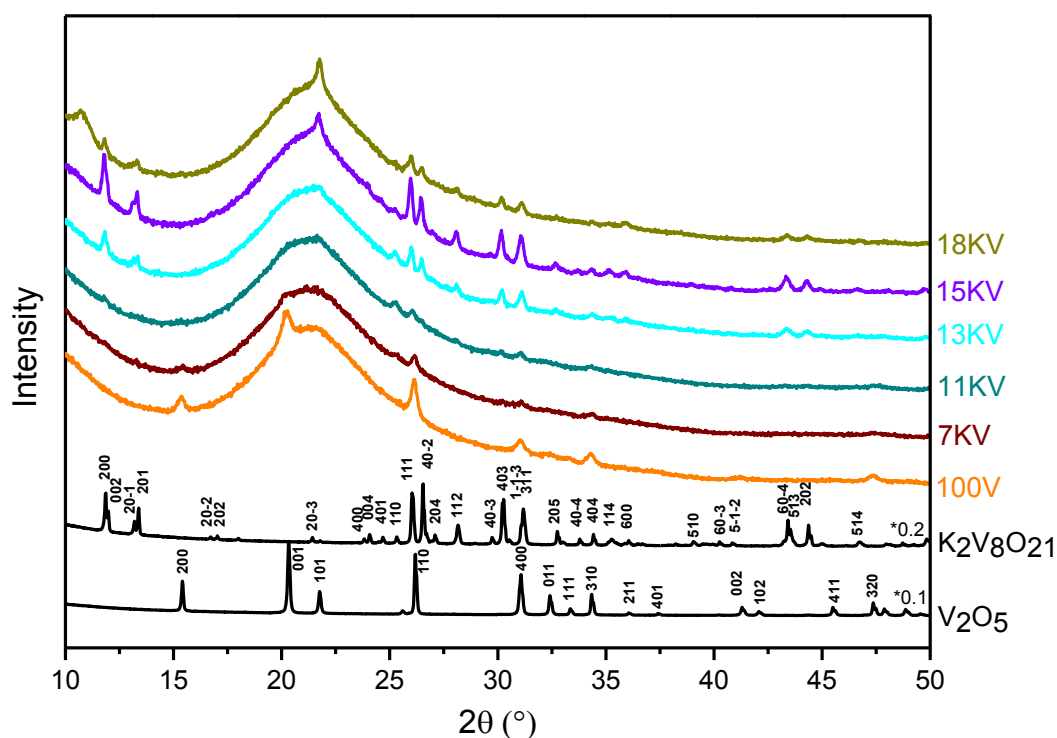


Figure 4.1. XRD patterns of xKV catalysts recorded at room temperature after synthesis. The patterns are offset for clarity.

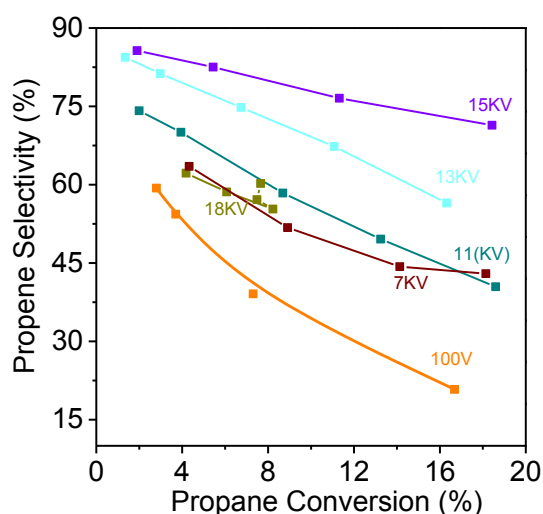
4.3.2 Oxidative dehydrogenation of propane

A summary of ODP reaction results for all catalysts is shown in Figure 4.2. Comparing the performance of xKV catalysts at comparable conversion with a sub-monolayer vanadium oxide supported on mesoporous silica (SBA-15) as a reference catalyst²⁵ showed that xKV catalysts lead to higher propene yields. However, in the case of xKV catalysts, higher temperatures are needed to achieve the same level of activity as $VO_x/SBA-15$. The lower activity of the xKV catalysts is most likely attributed to the comparatively low specific surface area (Table 1), which might be a result of the reaction, in particular, of the potassium component with silica. However, the poisoning of active species by potassium cannot be excluded. Propene yields and productivities of all catalysts determined at 500 °C under the conditions indicated in Figure 4.2 are listed in Table 2.

The propene selectivity was increased with an increase of K content and maximized in a medium K content, see Figure 4.2b. The best performance is achieved with catalyst 15KV. The high selectivity of 15KV is remarkable and comparable with a boron nitride catalyst.²⁶ The sample with the highest K content, catalyst 18KV, shows low propene yield. One possible explanation could be crystallization of support due to too much potassium which is present in the coating. A second reason could be formation of molten layer at higher temperatures which cause further decrease of surface area. Lowering of calcination temperature during preparation in this case would be one way to prevent reaction of K with support for preserving the surface area. This topic is investigated in details in Chapter 3. The selectivity to propene decreases with increasing conversion. The slope of this decrease is getting less with increasing the amount of potassium. This is in agreement with consecutive reaction of propene.

As mentioned before, for catalyst 15KV, $K_2V_8O_{21}$ was the only phase detected by XRD. Therefore, investigation of performance for $K_2V_8O_{21}$ in ODP reaction was performed. Preliminary results of the reactivity test for phase-pure $K_2V_8O_{21}$ bulk material demonstrated low activity of this material (0.8 % conversion at 450 °C). This is perhaps partially related to the low surface area of the sample ($1.5 \text{ m}^2/\text{g}$). The phase deactivates at higher temperatures, most likely due to sintering or reduction. In addition, K/Aerosil showed less than 2 % conversion at 500 °C under the applied reaction condition.

a)



b)

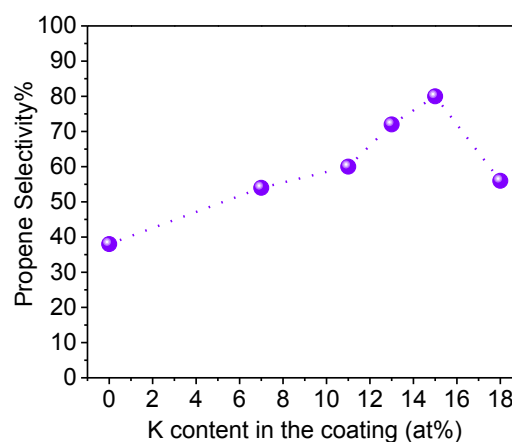
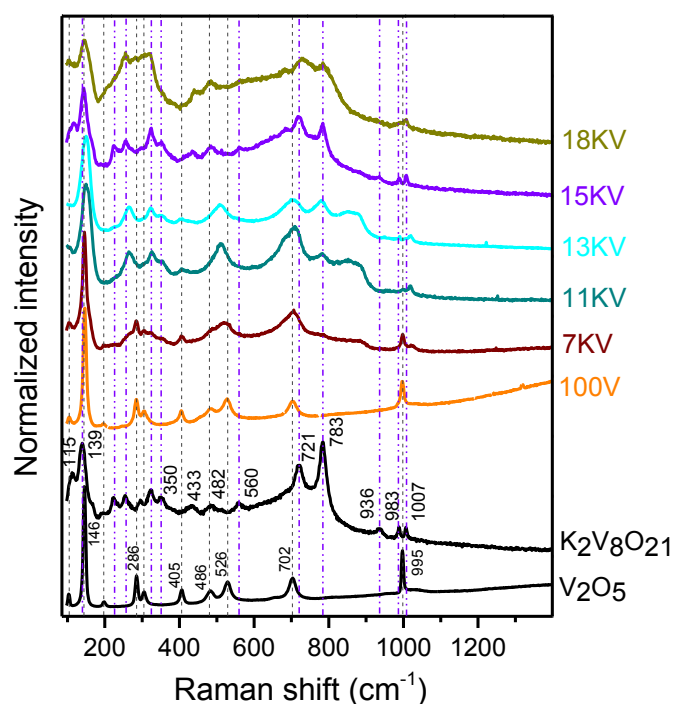


Figure 4.2. a) Selectivity versus conversion, b) propene selectivity at 8% conversion as a function of potassium content (at %) in the coating, in oxidative dehydrogenation or propane, feed composition $C_3H_8:O_2:N_2$ 7.5:7.5:85, Temperature: 450-500 °C (for catalyst 100V, 410-475 °C), contact time: 1.8 gs/ml.

4.3.3 Characterization of fresh catalysts

a)



b)

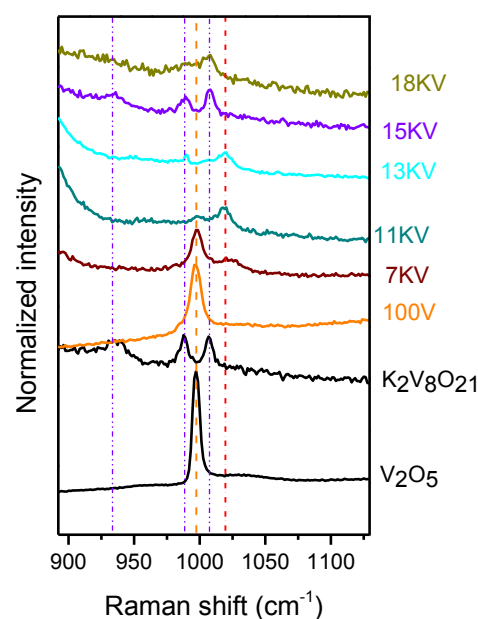


Figure 4.3. Raman spectra of freshly prepared catalysts, a) Overview, b) Zoom in at around 1000 cm^{-1} .

The Raman spectra of catalysts are reported in Figure 4.3 and compared with those of phase pure $K_2V_8O_{21}$ and V_2O_5 . Assignments of Raman modes for $K_2V_8O_{21}$ have been done elsewhere (Chapter 2). The spectra of catalysts 100V and 7KV match essentially the spectroscopic features of V_2O_5 . For sample 7KV there is also an extra band at $883cm^{-1}$ in the Raman spectrum which is tentatively attributed to the formation of polymeric vanadate species. Besides, the strong broadening of lines in the Raman spectrum of this catalyst can be accounted for the existence of a broad distribution of surface vanadate species and consequently the larger distribution of bond angles and broadening of atomic bond distances. By increasing the potassium content the contributions from vibrational modes of V_2O_5 gets weaker and Raman modes of $K_2V_8O_{21}$ become dominant.

Catalyst 15KV, having $K_2V_8O_{21}$ in the coating based on XRD, displays a nearly identical Raman spectrum as $K_2V_8O_{21}$, presenting all the vibrational modes of $K_2V_8O_{21}$ and comparable broad

spectral features. Comparing the Raman spectra of $K_2V_8O_{21}$ with that of 15KV a noticeable difference in relative intensity of bands at 720 and 782 cm^{-1} is present. The mentioned deviation is most likely arising from partially reduced state of $K_2V_8O_{21}$ formed during thermal spreading at relatively high temperature (see Chapter 2).

Table 4.2. Content of $K_2V_8O_{21}$ in the coating of prepared catalysts obtained by quantification of DSC analysis, and propene yield and productivity of catalysts at ODP feed of $C_3H_8:O_2:N_2$ 7.5:7.5:85 at 500 °C (475 °C for catalyst 100V)

ID	$K_2V_8O_{21}$ content in coating (wt %)	Productivity ($g_{C_3}/g_{cat}\cdot h$)	Yield (%)
18KV	24	0.011	4
15KV	48	0.038	13
13KV	33	0.025	9
11KV	22	0.021	7
7KV	17	0.021	7
100V	0	0.009	3

In the DSC patterns of catalysts (Figure 4.4) the endothermic peak at 520 °C, attributed to melting of $K_2V_8O_{21}$, is present for all the xKV catalysts. The disagreement with the XRD results is due to detection limit of XRD. A comparison between the enthalpy of melting for phase pure $K_2V_8O_{21}$ with that of the supported catalysts can be applied for quantification of the content of $K_2V_8O_{21}$ in the prepared catalysts. The calculated $K_2V_8O_{21}$ content of catalysts is listed in Table 3. Considering the results of DSC quantification and loading of catalyst 15KV, less than 50 % of coating contributes to $K_2V_8O_{21}$. So, it is evidenced that for catalyst 15KV extra probably highly dispersed vanadium oxide species beside crystalline $K_2V_8O_{21}$ are present. This is also the case for 13KV and 11KV. Therefore, XRD and DSC differ for most of the catalysts. The degree of crystallinity of present $K_2V_8O_{21}$ on the support, however, may prevent an accurate quantification applying DSC. Therefore, supplementary characterization techniques, such as EDX analysis XPS and UV-Vis spectroscopy, have been performed for further prove of existence of extra species on the surface of the catalysts.

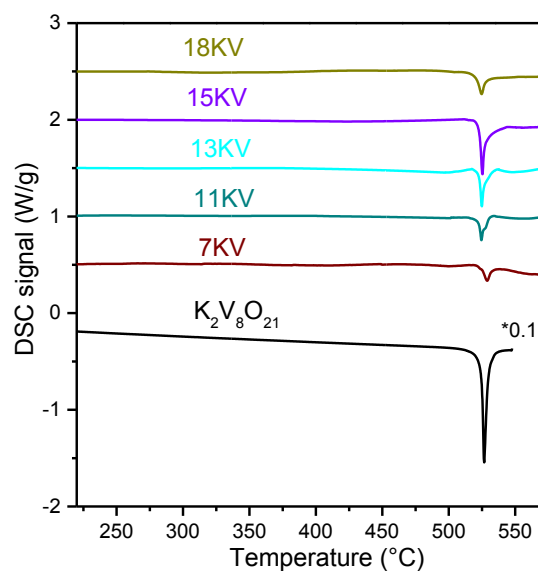


Figure 4.4. DSC patterns of prepared catalysts under the flow of 70 ml/min 21 % O₂/ 79 % Ar with the heating rate of 10Kpm.

Table 4.3. Quantification of DSC melting signal

ID	Area under peak	Loading (g _{K-V oxide} /g _{cat})	K ₂ V ₈ O ₂₁ content (wt %)
18KV	1.188	0.09	24
15KV	2.16	0.084	48
13KV	1.701	0.096	33
11KV	1.188	0.098	22
7KV	0.7992	0.088	17
K ₂ V ₈ O ₂₁	54	1	100

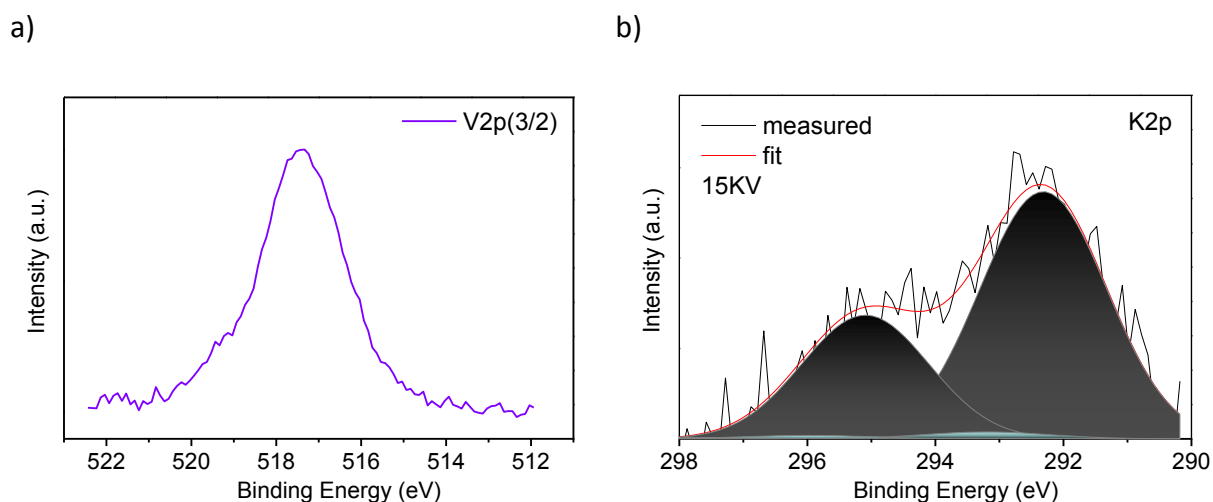


Figure 4.5. a) V2p(3/2) and b) K2p core level XPS spectra of as prepared 15KV sample after Shirley background subtraction and charging correction.

Table 4.4. Surface-near molar ratios of catalyst 15KV according to XPS

ID	V/Si	O/(V+Si)	C/Si	K/Si	V/K
15KV	0.064	2.04	0.068	0.0091	7.1

The room temperature XPS spectra of catalyst 15KV are depicted in Figure 4.5. When comparing the surface to the bulk V/K ratios, the values deviate and the surface V/K ratio of 7.1 is clearly higher than the bulk ratio of 5.7, see table 4.4.

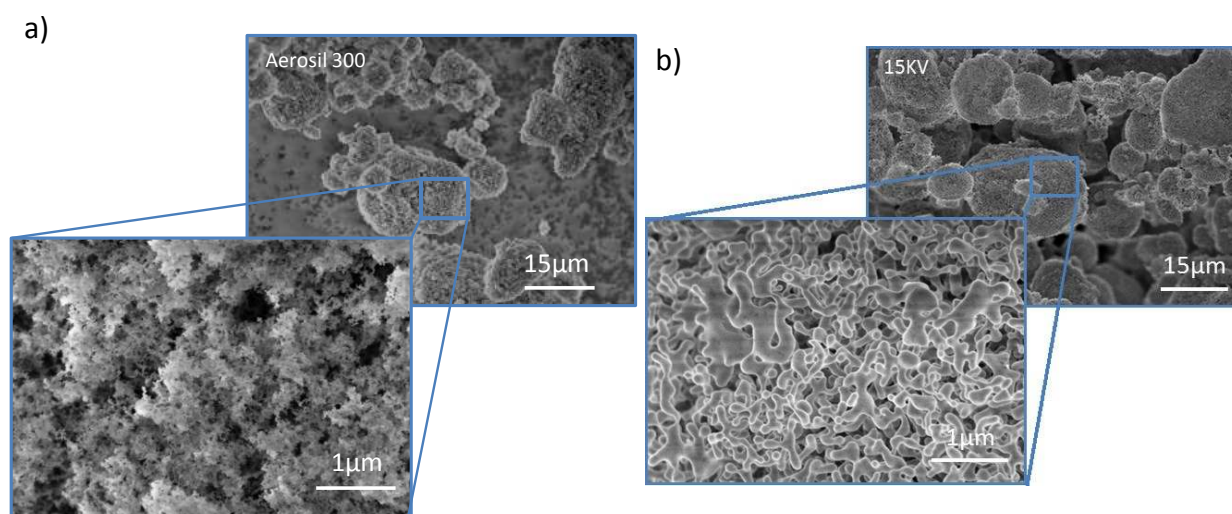


Figure 4.6. SEM images of a) Aerosil 300 and b) as-prepared catalyst 15KV.

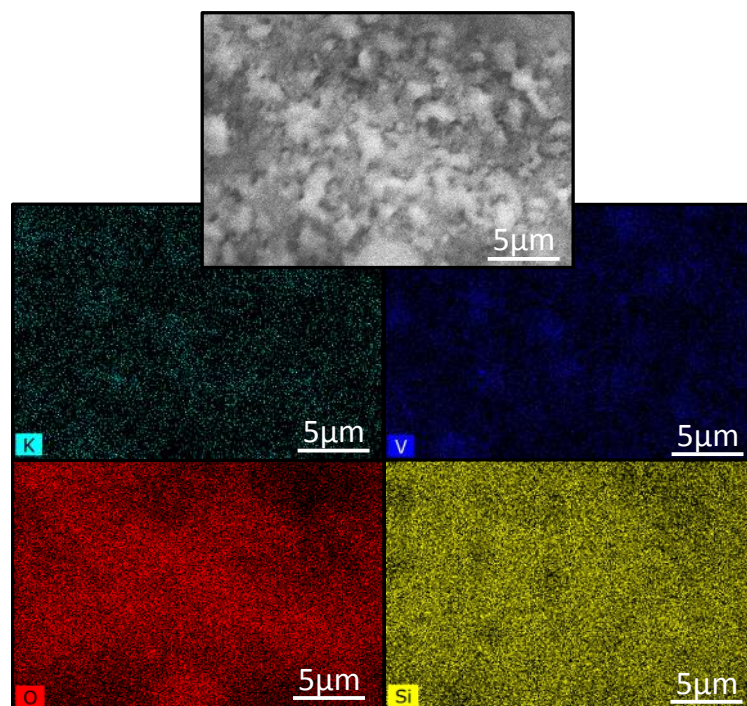


Figure 4.7. SEM image and elemental mappings of catalyst 15KV.

As it can be seen from SEM image of catalyst 15KV, shown in Figure 4.6b, the particles of Aerosil support are maintained and they were not fused during the applied thermal spreading method. However, comparing the primary particles of pure Aerosil with that of 15KV in Figure 4.6 reveals that the silica particles are linked together in catalyst 15KV. In the EDX mapping of catalyst 15KV, patches of potassium vanadate phase are present on top of the silica spheres, see Figure 4.7. In addition, the ratio of 9.3 for V/K, obtained by EDX analysis measured at different spots, is an extra evidence for presence of extra vanadium species, see supporting information Table S4.1.

4.3.4 Characterization of spent catalysts

Physical and chemical properties of spent catalysts are listed in Table 4.5. XRF analysis of spent catalysts demonstrates stability of compositions since the potassium to vanadium ratio in the coating and calculated loading scatter around the same values as the fresh catalysts. Regarding BET surface area, small decrease was observed. In the XRD patterns of spent catalysts, shown in Figure 4.8, for all potassium containing samples, clear change in the phase composition due to formation of reduced phases ($K_{0.5}V_2O_5$ and $K_{0.25}V_2O_5$) was observed, see Table 4.5.

Table 4.5. Physical properties of spent xKV catalysts, after being one month under ODP reaction conditions.

Catalyst number	ID	Analytical ratio (K:V)	Analytical loading ^a (wt %)	BET (m ² /g)	XRD main phases
25442	18KV	19:81	8.8	11	K _{0.5} V ₂ O ₅
22920	15KV	15:85	9	13	K _{0.5} V ₂ O ₅ , K ₂ V ₈ O ₂₁
25440	13KV	13:87	9.5	18	K _{0.25} V ₂ O ₅ , K _{0.5} V ₂ O ₅ , UN ^b
25439	11KV	11:89	10	20	K _{0.25} V ₂ O ₅ , K _{0.5} V ₂ O ₅ , UN ^b
22919	7KV	7:93	9.6	25	K _{0.25} V ₂ O ₅ , UN ^b
25438	100V	0:100	9.6	35	V ₂ O ₅

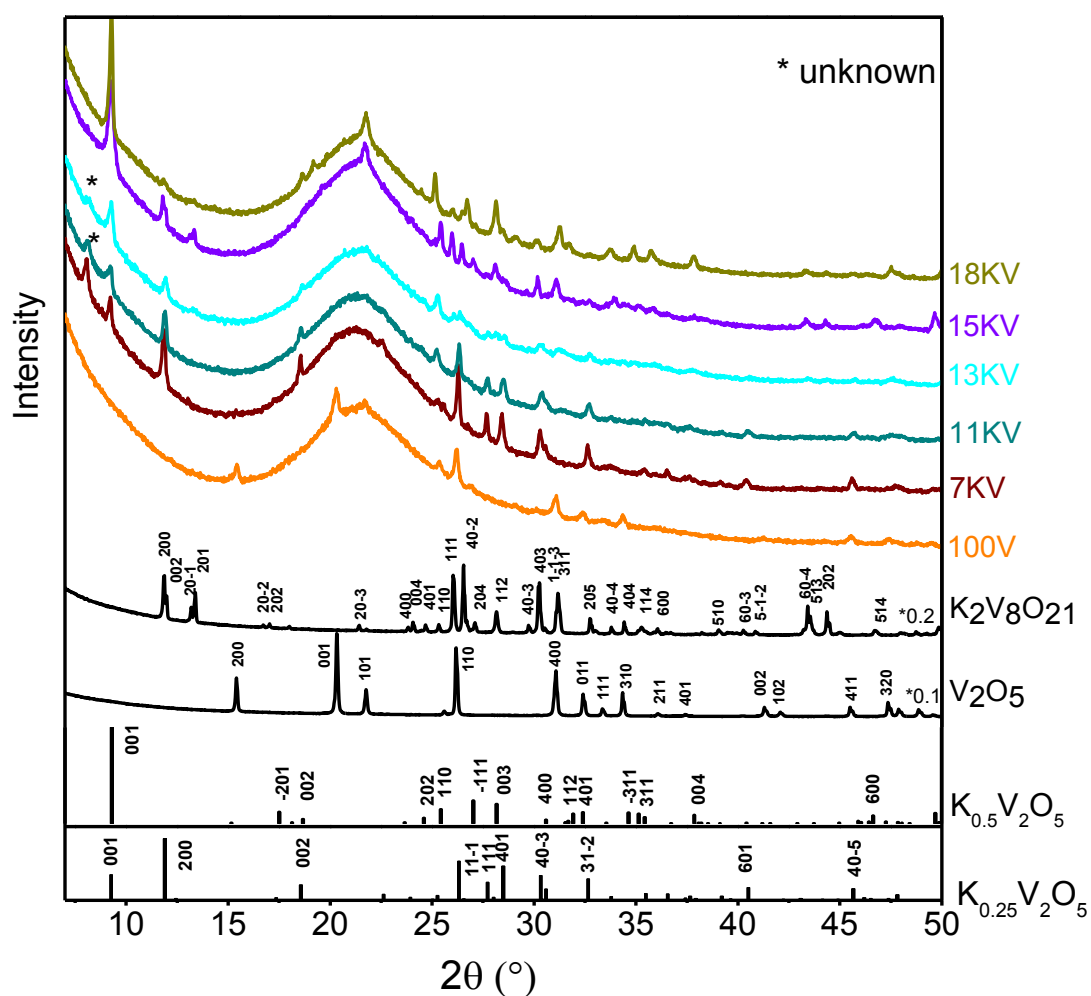
^aanalyzed by XRF, based on V₂O₅+K₂O^bunknown phases

Figure 4.8. XRD patterns of spent xKV catalysts, one month time on stream.

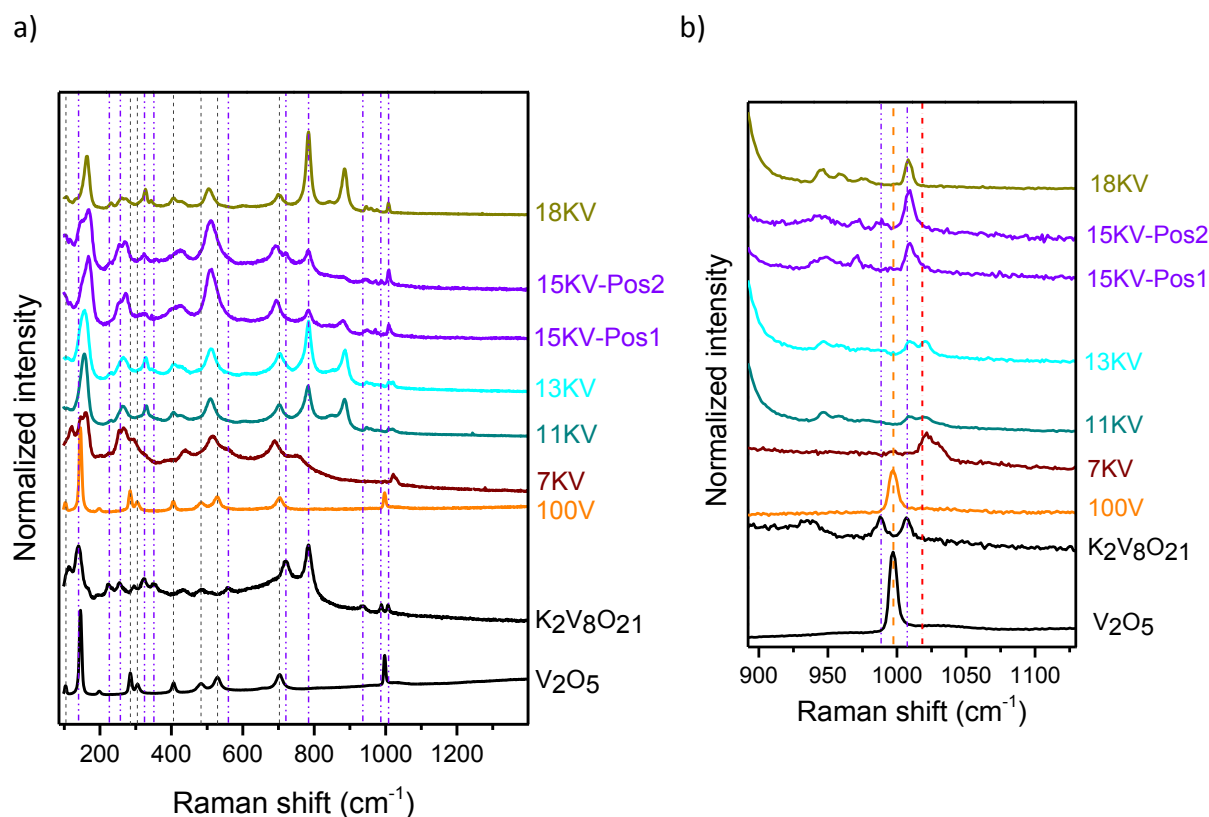


Figure 4.9. Comparisons of the Raman spectra of spent catalysts a) Over view, b) Zoom in at around 1000 cm⁻¹.

The Raman spectra of spent catalysts, depicted in Figure 4.9, are in accordance with the XRD results. The Raman spectrum of spent 15KV demonstrates presence of K₂V₈O₂₁ accompanied by K_{0.5}V₂O₅²⁷. The spectrum of catalyst 7KV is dominated with spectral features of K_{0.25}V₂O₅²⁷ which was measured in literature. Having a closer look at the Raman spectra at around 1020 cm⁻¹ reveal possible presence of dispersed vanadia species in all spent catalysts except for 100V and 18KV. However, K_{0.25}V₂O₅ has also a peak in this region of Raman spectra which make it difficult for catalysts 7KV, 11KV and 13KV to distinguish dispersed vanadia species. The observed changes in the phase composition of spent catalysts could be attributed to partial reduction of the catalysts, which is particularly evident by change of the color from dark brown to green.

In the SEM and EDX mapping of spent 15KV catalyst, shown in Figure 4.10 and 11, a further agglomeration of potassium vanadate is noticeable based on elemental mapping of K and V. The present needles are mainly due to remains of quartz wool which was used to fix the catalyst in the reactor for catalysis measurement.

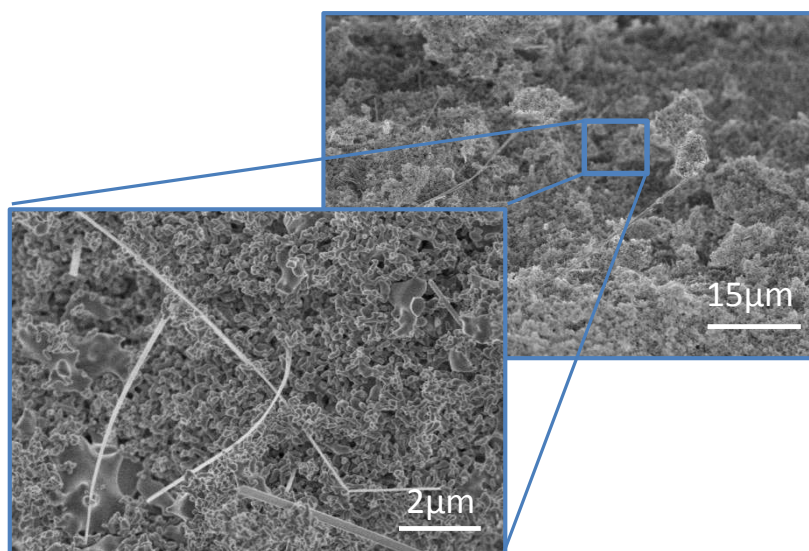


Figure 4.10. SEM of spent catalyst 15KV after one month time on stream.

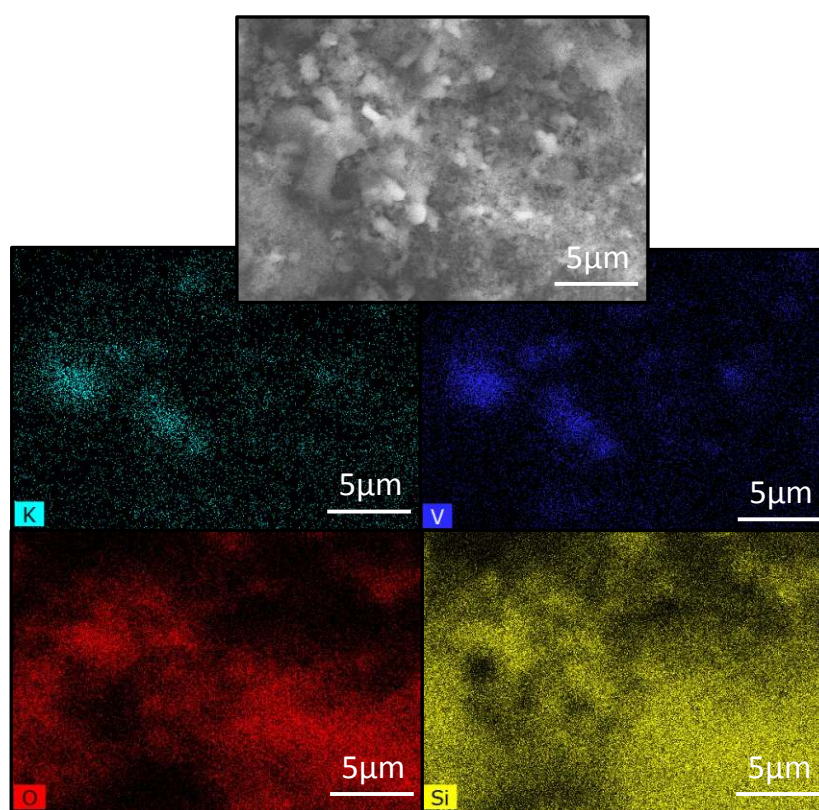


Figure 4.11. SEM image and elemental mappings of spent catalyst 15KV, after one month time on stream.

From the K2p core level spectra of spent 15KV catalyst formation of a new potassium doublet in addition to the original one is noticeable. The extra doublet with K2p(3/2) peak at 293.1 eV is most likely attributed to formation of potassium-silicate glass²⁸ or simply silica-

supported potassium oxide which was measured as reference (see Chapter 3). The developed shoulder in the position of V^{4+} species in the $V2p$ core level spectra is a prove of reduction that occurred under the reaction conditions. In EDX analysis of different spots for the spent catalyst a better dispersion of potassium over the surface of catalyst was observed, see supporting information Table S4.2.

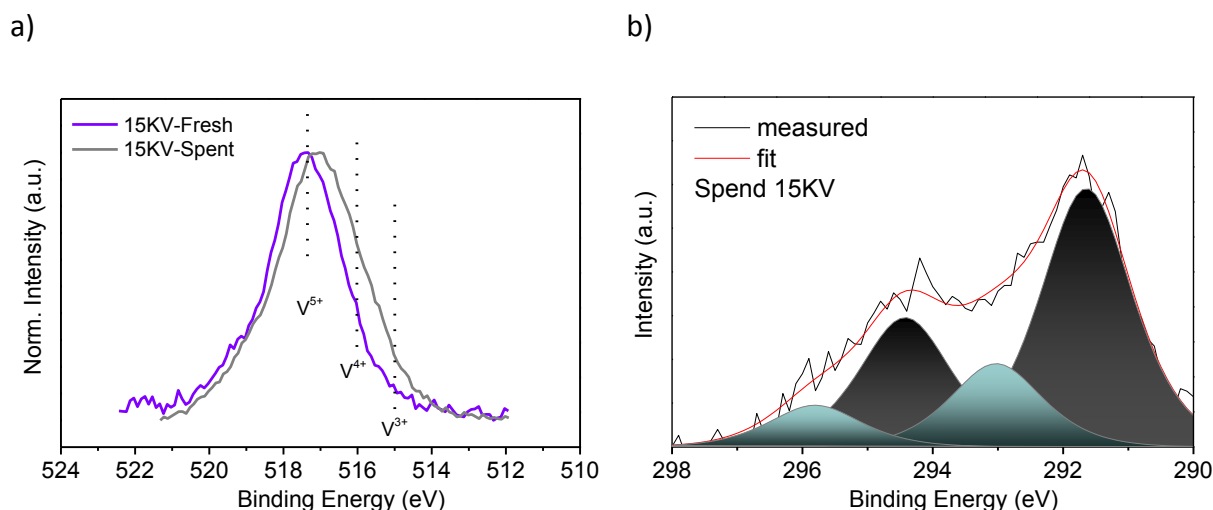


Figure 4.12. a) $V2p(3/2)$ and b) $K2p$ core level XPS spectra of spent 15KV catalyst after Shirley background subtraction and charging correction.

4.4 In-situ characterization

Among the explored catalysts, sample 15KV has demonstrated the most interesting results in ODP reaction. Therefore, the possible alterations of catalyst 15KV at the reaction temperatures were studied by high temperature XRD and XPS, in-situ Raman, and in-situ UV-Vis spectroscopy. The explored catalyst shows a complex dynamic behavior during the in-situ experiments. The dynamic behavior is likely associated with the formation of oxygen vacancies, and phase transformation into vanadium bronze phases in the coating which will be discussed in the following.

4.4.1 High temperature XRD

Figure 4.13 presents the temperature dependent XRD of catalyst 15KV under the flow of 10 ml/min 21 % O_2 /79 % Ar. In oxidizing atmosphere the catalyst remains relatively stable over

the applied temperature range. Formation of an extra small peak at about 9.2° by reaching 450°C and via cooling is probably due to formation of $\text{K}_{0.5}\text{V}_2\text{O}_5$.

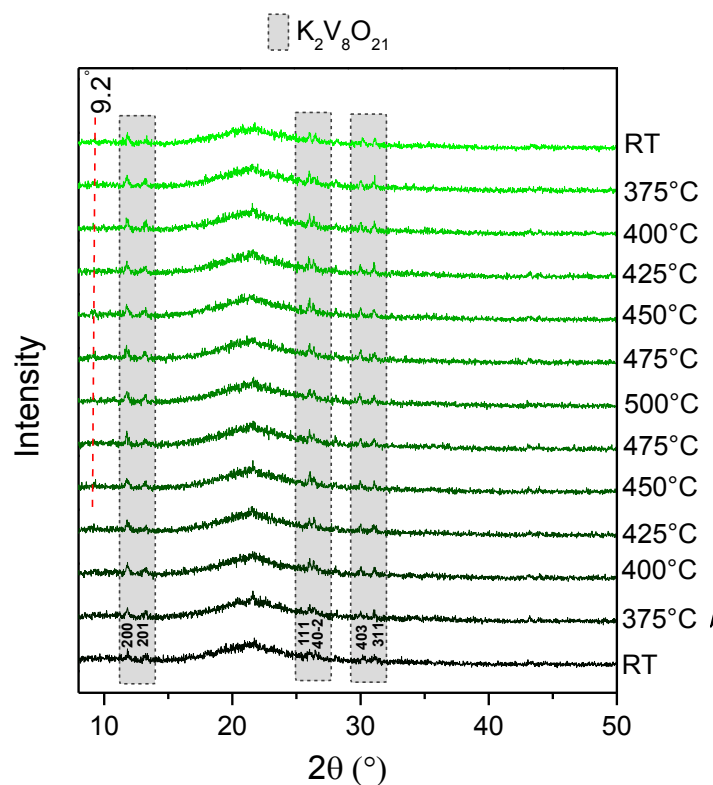


Figure 4.13. Temperature dependent XRD of catalyst 15KV under the flow of 10 ml/min 21 % O_2 /79 % Ar.

4.4.2 High temperature XPS

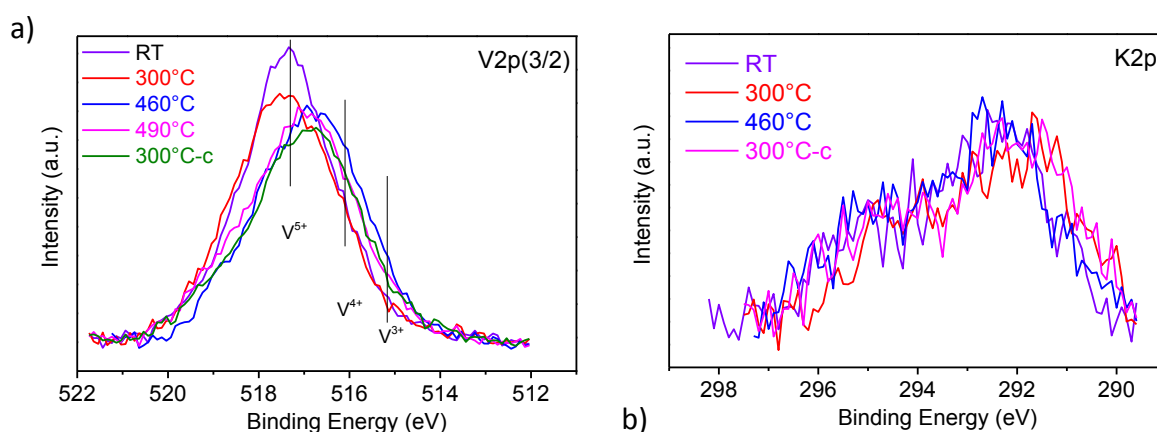


Figure 4.14. a) $\text{V}2\text{p}(3/2)$ and b) $\text{K}2\text{p}$ core level XPS spectra of catalyst 15KV via heating and cooling.

XPS measurements at elevated temperatures were performed to investigate the V/K surface ratio via reduction in the catalyst 15KV.

Table 4.6. Near-surface composition of catalyst 15KV at different temperatures in the XPS cell (small amount of O₂ (2x10⁻⁸ mbar) was dosed into the UHV chamber during the experiment)

	V/Si	O/(V+Si)	C/Si	K/Si	V/K
RT					7.7
300 °C	0.054	2.07	0.09	0.007	7.6
460 °C	0.052	2.08	0.09	0.008	6.5
300 °C_c	0.05	2.07	0.09	0.008	6.1

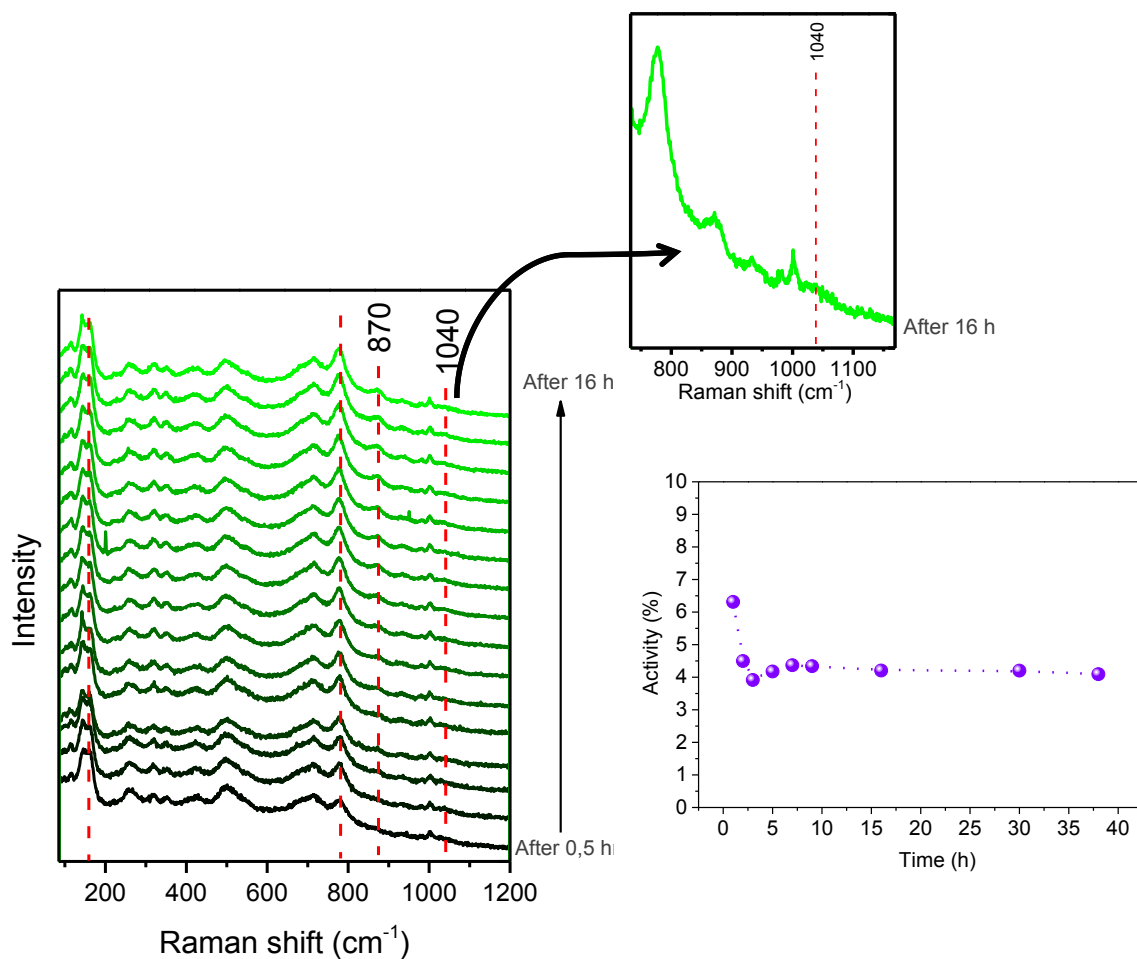
c: during cooling

Figure 4.14 shows the V2p and K2p spectra of the catalyst. As evidenced by the shift to lower binding energy, vanadium underwent reduction with increasing temperature. However, the contributions of beam induced reduction and vacuum cannot be excluded. Table 6 contains the surface-near elemental ratios during the heating experiments. Based on the results, it can be argued that K segregation occurs upon the reduction of vanadium.

4.4.3 In-situ Raman

In order to determine the dynamic structural change of the catalyst during oxidative dehydrogenation of propane, real-time Raman spectra over 15KV catalyst were recorded under reaction conditions.

a)



b)

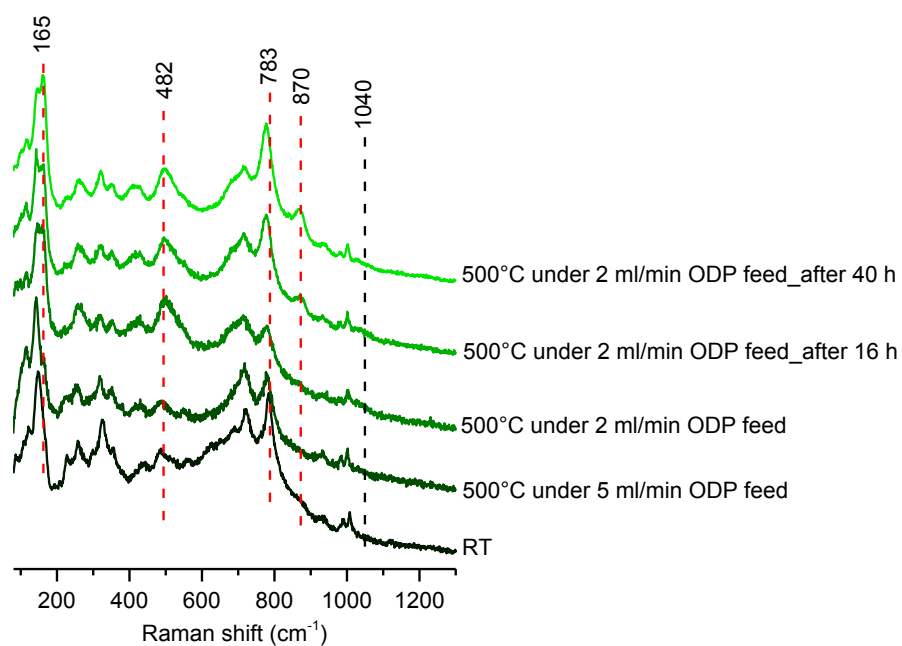


Figure 4.15. In-situ Raman spectroscopy of catalyst 15KV under ODP reaction conditions with the feed composition of $\text{C}_3\text{H}_8:\text{O}_2:\text{N}_2$ 7.5:7.5:85, a) Raman spectra and activity data while keeping at 500 °C, flow: 2 ml/min b) comparison of Raman spectra taken in different conditions.

Temperature dependent Raman spectra of the catalyst are shown in Figure S4.1. The changes in the spectra within the measured temperature range were small, but detectable. Growth of the band at 165 cm^{-1} , see Figure S4.1, was the most prominent one.

To investigate the induced change in more detail a second run of experiment applying lower flow of gas has been performed. In this experiment the observed change is more pronounced. Formation of a band at 870 cm^{-1} is quite noticeable with time on stream, see Figure 4.15a. The spectra taken at different conditions are summarized in Figure 4.15b for direct comparison. The intensity of the peak at 482 cm^{-1} and the band at 165 cm^{-1} increase and the weak band at 870 cm^{-1} develops. In addition, the band at 783 cm^{-1} gets sharper. With the progress of time, the mentioned changes get quite pronounced (see the peaks indicated by the red dotted lines in Figure 4.15b). These results correlate well with the spectrum of the catalyst used in ODP for about one month, see Figure 4.9. For the used catalyst the changes in the spectrum are more pronounced. The observed changes are due to the partial reduction during catalysis.

The transformation of Aerosil supported $\text{K}_2\text{V}_8\text{O}_{21}$ into $\text{K}_{0.5}\text{V}_2\text{O}_5$ has been confirmed by high temperature XRD performed under flow of propane to simulate reducing conditions (Figure S4.2 in the Appendix). Accordingly, formation of the vanadium bronze starts at $450\text{ }^\circ\text{C}$. This transformation is associated with the alteration of unit cell parameters and perfectly distinguishable color change and also turn of morphology²⁹. Previous comparison study applying IR spectroscopy for $\text{K}_2\text{V}_8\text{O}_{21}$ in oxidize and reduce states has proven that the reduced vanadium bronze has more VO_6 polyhedron in its crystal structure.²⁹ The layers of VO_6 could give rise to the stretching mode of V-O-V bridges observed at 883 cm^{-1} for the spent catalyst. Moreover, the increase in the intensity of band at 483 cm^{-1} may be associated with $\nu(\text{V-O})$ which get sharper after formation of chains of VO_6 .

The reactivity data taken in in-situ cell demonstrates small deactivation of sample followed by stable activity over tested period of time. This performance data are taken while the reduced bronze phase has been developing continuously over time. Therefore, it is not logical to conclude from the present in situ Raman studies if the $\text{K}_2\text{V}_8\text{O}_{21}$ in its oxidized or reduced state is acting as the active phase. On the other hand the mentioned reduction is accompanied by release of potassium as it is clear from comparison of K/V ratio in $\text{K}_2\text{V}_8\text{O}_{21}$ with that of $\text{K}_{0.5}\text{V}_2\text{O}_5$. This was also evidenced by temperature dependent XPS spectroscopy

via increase of surface K/V ratio. In this view, $K_2V_8O_{21}$ can release potassium for the surface vanadium groups.

The Raman bands at $1027\text{--}1040\text{ cm}^{-1}$ are attributed to the vanadyl bond of vanadium monolayer catalysts.³⁰ This band is detectable in catalyst 15KV at higher temperatures, see Figure 4.15a.

4.4.4 In-situ UV-Vis spectroscopy

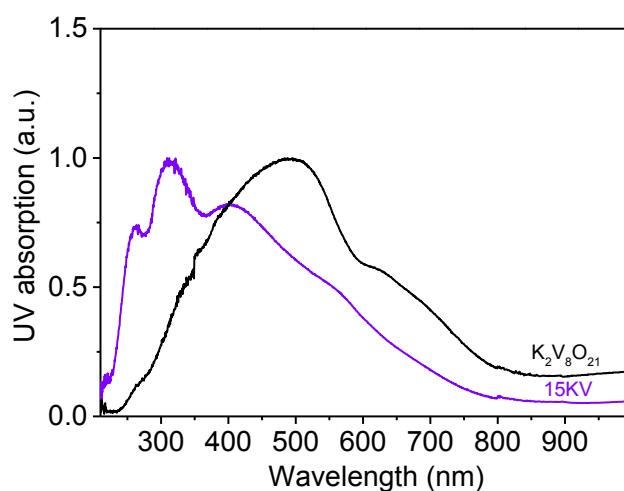


Figure 4.16. Comparison of UV-Vis spectrum of catalyst 15KV with that of $K_2V_8O_{21}$.

Comparison of the room temperature spectrum of phase-pure $K_2V_8O_{21}$ with that of catalyst 15KV, shown in Figure 16, demonstrates obvious differences. The observed deviation is more pronounced for the band at about 313 and 260 nm which are present in catalyst 15KV, but not in $K_2V_8O_{21}$. Based on the structural information the bands around 320 and lower are due to V^{5+} in tetrahedral environment³¹, which are clearly detectable in obtained UV-Vis spectrum from catalyst 15KV. Formation of the band around 500nm is usually occurring for vanadium in octahedral environment. In the case of $K_2V_8O_{21}$ it should be attributed to presence of VO_6 units in the structure. The presence of broad bands in the entire region of the UV-Vis spectrum is expected considering the complex structure of octavanadate composed of VO_5 and VO_6 polyhedra.

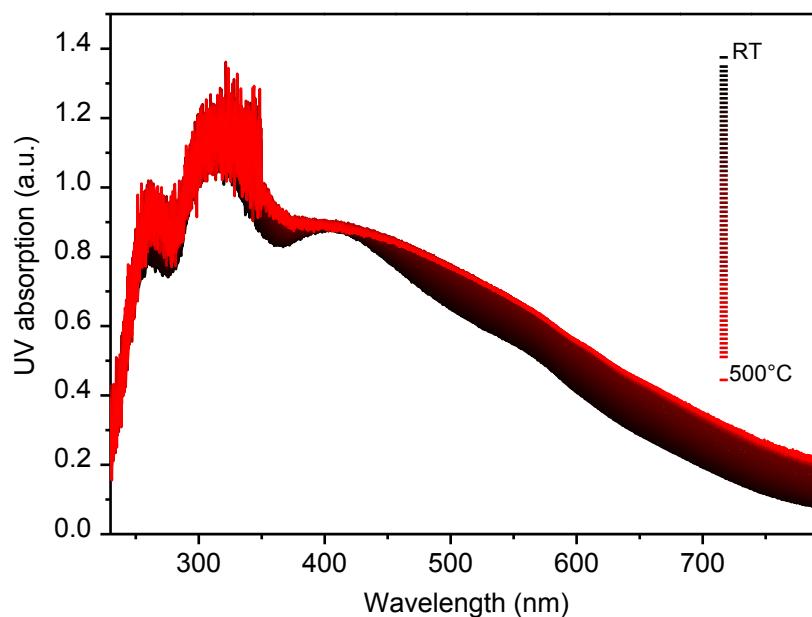
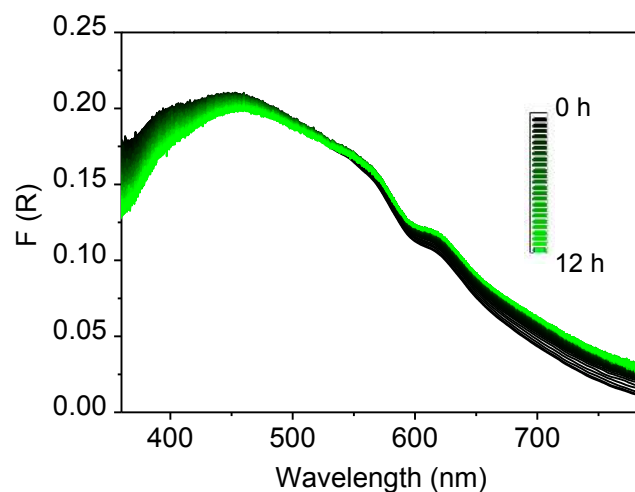


Figure 4.17. In-situ UV-Vis spectra of catalyst 15KV under ODP reaction conditions ($\text{C}_3\text{H}_8:\text{O}_2:\text{N}_2$ 7.5:7.5:85 %, m_{cat} : 10mg, Flow: 2 ml/min).

The alteration of catalyst 15KV under reaction conditions was investigated applying in-situ UV-Vis spectroscopy. Figure 4.17 shows the UV-Vis spectra of catalyst 15KV without any normalization under the ODP feed of $\text{C}_3\text{H}_8:\text{O}_2:\text{N}_2$ 7.5:7.5:85 %. The original trace obtained at room temperature in the dehydrated state is illustrated in black. The colors of subsequent spectra taken during heating from room temperature to 500 °C change from black to red. The intensity between 600-800nm related to d-d transitions of V^{4+} ³¹ is increasing with increasing temperature indicating possible reduction of vanadium. As the mentioned change has been occurred already before reaching the reaction temperature, structural-activity correlation study was not possible in this experiment. Therefore, in a second experiment the sample was heated to 500 °C under the flow of synthetic air, then the feed of reaction was introduced at 500 °C (Figure 4.18). The increase in intensity at 600-800nm, shown in Figure 4.18a, is accompanied by an initial deactivation followed by stable performance during 12 h of measurement. Figure 4.18b shows the correlation between reactivity data and spectroscopy ones.

a)



b)

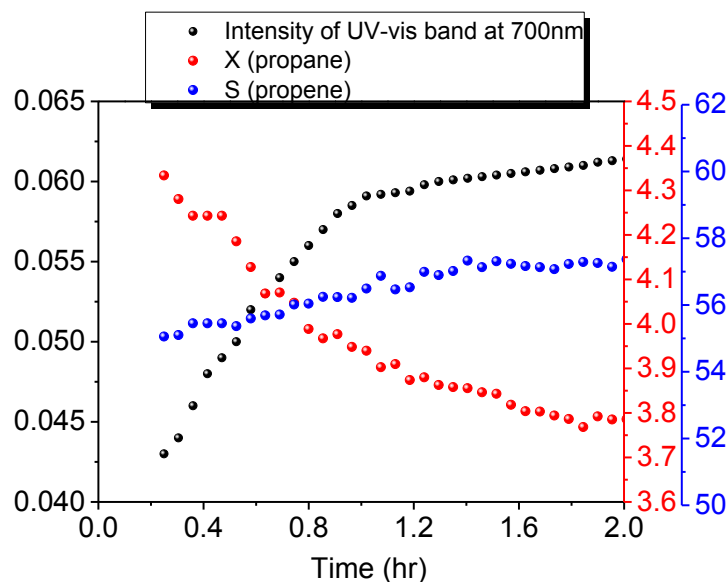


Figure 4.18. In-situ UV-Vis spectroscopy of catalyst 15KV under the ODP reaction conditions at 500 °C ($\text{C}_3\text{H}_8:\text{O}_2:\text{N}_2$ 7.5:7.5:85 %, m_{cat} : 10mg, Flow: 2 ml/min) a) UV-Vis spectra over 12 hr time on stream, b) Comparison of reactivity data with the intensity of UV-vis band at 700 nm.

Formation of V^{4+} species in catalyst 15KV is consistent with the results of in-situ Raman spectra taken under the reaction conditions. However, formation of bronze phase was a relatively slow process in the Raman experiment while the initial reduction which is evidenced by UV-Vis experiment was a relatively fast response which correlates well with initial deactivation observed in the in-situ experiment. Therefore, formation of bronze phase is not an essential step for good performance of catalyst, but a side phenomenon happening

during reaction. However, this phenomenon can contribute to the release of potassium and doping of segregated vanadium sites with potassium as it is also evidenced by high temperature XPS data.

4.5 Discussion

Comparison of XRD results with the reactivity data of xKV/Aerosil catalysts reveals that by decreasing the content of crystalline V_2O_5 in the coating via increasing the content of potassium and formation of $K_2V_8O_{21}$ better performance was achieved. The selectivity to propene approaches a maximum at medium potassium content of 15 at% in the coating.

The calibration of DSC melting signals demonstrates that less than 50 % of the vanadium atoms in the catalyst belong to the present $K_2V_8O_{21}$ crystalline phase. Therefore, contributions of highly dispersed phases on reactivity of the catalysts should be taken into account. Moreover, according to the V/K stoichiometric ratio of 4 in $K_2V_8O_{21}$ compared with that of XPS data, 7.1, there should be extra vanadia species on the surface of catalyst that do not belong to the phase. These data agree well with the results of Raman and SEM-EDX mapping, providing evidences for the presence of extra vanadium sites on the surface of catalyst. That was also supported by comparison of UV-Vis spectra of catalyst 15KV with that of $K_2V_8O_{21}$ revealing presence of vanadium in tetrahedral environment on the surface of the catalyst. Structural activity study of catalyst under the operating conditions was necessary to discriminate catalytically relevant surface sites from spectator species. For investigation of possible active site at the reaction temperature, a combination of in-situ Raman and UV-Vis spectroscopy accompanied by reactivity test of bulk $K_2V_8O_{21}$ and V_2O_5 crystalline phases were applied. The Raman spectra taken under ODP reaction conditions revealed the slow formation of the reduced phase ($K_{0.5}V_2O_5$) during ODP reaction monitored over 12 h time on stream. The subsequent formation of bronze phases observed by Raman spectroscopy during ODP is in agreement with the results of the Raman spectrum of the spent catalyst. The color of the catalyst bed also turned to green during the ODP reaction, suggesting the presence of reduced vanadium species. On the other hand reactivity data taken simultaneously in the in-situ cell demonstrate slight deactivation over the first two hours of experiment followed by stable performance. In-situ UV-Vis spectroscopy with simultaneous reactivity measurements provides the explanation for the initial slight deactivation during

the oxidative dehydrogenation of propane. A relatively fast reduction via increasing intensity of UV-Vis band related to d-d transition of V^{4+} was noticeable. Moreover, potassium enrichment on the surface of the catalyst via reduction which was evidenced by high temperature XPS might also contribute to the initial deactivation.

Considering the low level of activity for the pure (unsupported) crystalline $K_2V_8O_{21}$ phase, we propose that the major active site is K-doped vanadium with the low coordination number rather than present potassium vanadate.

Four-coordinated vanadium oxide species were shown to be more selective in ODP reaction (see Chapter 3). In accordance with this fact, $K_2V_8O_{21}$ in the coating seems to act most likely as a sink for taking the extra potassium and vanadium out of play, and the main active species of catalyst 15KV seems to be potassium doped vanadium which is acting selectively. However, the role of $K_2V_8O_{21}$ as a reservoir for providing potassium for the vanadium active species via reduction to bronze phase cannot be excluded. On account of presented results, segregated vanadium oxide species are the most likely responsible for activity. The relatively high level of selectivity is due to the presence of potassium which is known as a good promotor for supported vanadium oxide catalysts. Higher selectivity of catalyst 15KV in comparison to other reported potassium doped vanadia on silica is most likely due to formation of segregated vanadia on the surface of $K_2V_8O_{21}$ which is acting as a better support than SiO_2 .

4.6 Conclusion

The applied undemanding preparation method appears to be quite promising for synthesis of potassium doped vanadium monolayer catalyst for ODP reaction. The obtained yield of 13 % for catalyst 15KV is higher than the best results obtained from other reported studies on K-V/ SiO_2 .¹⁶ The good performance of this catalyst could be explained by in-situ formation of potassium doped vanadium monolayer. A correlation between formation of $K_2V_8O_{21}$ and increase in selectivity to propene was noticeable. This observation is consistent with the above conclusion that beside preparation of monolayer catalyst, applying the right composition where the excess of elements go to a dead phase would also give relatively good performance applying even very simple preparation techniques. It consists in use of heterogeneous two-phase systems; one phase being a sink for excess amount of elements,

whereas the real active phase are located in the second part. In our case study, $\text{K}_2\text{V}_8\text{O}_{21}$ serve this purpose. However, the role of $\text{K}_2\text{V}_8\text{O}_{21}$ as a reservoir for providing potassium for the vanadium active species via reduction to bronze phase cannot be excluded.

Acknowledgments

This research was conducted in the framework of the BasCat, collaboration between BASF SE, TU Berlin, FHI, and the cluster of excellence “Unified Concepts in Catalysis” (UniCat, www.unicat.tu-berlin.de). We thank Maike Hashagen, Jasmin Allan and Dr. Olaf Timpe for technical assistance.

4.7 Bibliography

1. T. Blasco and J. M. L. Nieto, *Appl Catal A Gen*, 1997, **157**, 117-142.
2. F. Cavani, N. Ballarini and A. Cericola, *Catalysis Today*, 2007, **127**, 113-131.
3. G. C. Bond and S. F. Tahir, *Applied Catalysis*, 1991, **71**, 1-31.
4. J. T. Grant, C. A. Carrero, A. M. Love, R. Verel and I. Hermans, *ACS Catalysis*, 2015, **5**, 5787-5793.
5. D. A. Bulushev, F. Rainone, L. Kiwi-Minsker and A. Renken, *Langmuir*, 2001, **17**, 5276-5282.
6. A. E. Lewandowska, M. Calatayud, E. Lozano-Diz, C. Minot and M. A. Bañares, *Catalysis Today*, 2008, **139**, 209-213.
7. F. Amano, T. Yamaguchi and T. Tanaka, *Catalysis Today*, 2007, **120**, 126-132.
8. H. Si-Ahmed, M. Calatayud, C. Minot, E. L. Diz, A. E. Lewandowska and M. A. Bañares, *Catalysis Today*, 2007, **126**, 96-102.
9. G. Garcia Cortez, J. L. G. Fierro and M. A. Bañares, *Catalysis Today*, 2003, **78**, 219-228.
10. G. Deo and I. E. Wachs, *Journal of Catalysis*, 1994, **146**, 335-345.
11. I. E. Wachs and B. M. Weckhuysen, *Appl Catal A Gen*, 1997, **157**, 67-90.
12. G. Ramis, G. Busca and F. Bregani, *Catal Lett*, 1993, **18**, 299-303.
13. L. Lietti, P. Forzatti, G. Ramis, G. Busca and F. Bregani, *Applied Catalysis B: Environmental*, 1993, **3**, 13-35.
14. R. Grabowski, B. Grzybowska, K. Samson, J. Słoczyński, J. Stoch and K. Weisło, *Appl Catal A Gen*, 1995, **125**, 129-144.
15. B. Grzybowska, P. Mekšs, R. Grabowski, K. Weisło, Y. Barboux and L. Gengembre, in *Studies in Surface Science and Catalysis*, eds. V. C. Corberán and S. V. Bellón, Elsevier, 1994, vol. Volume 82, pp. 151-158.
16. A. Klisińska, A. Haras, K. Samson, M. Witko and B. Grzybowska, *J. Mol. Catal. A Chem.*, 2004, **210**, 87-92.
17. J. C. Vedrine, J. M. M. Millet and J.-C. Volta, *Catalysis Today*, 1996, **32**, 115-123.
18. D. Courcot, A. Ponchel, B. Grzybowska, Y. Barboux, M. Rigole, M. Guelton and J. P. Bonnelle, *Catalysis Today*, 1997, **33**, 109-118.
19. G. Garcia Cortez, J. L. G. Fierro and M. A. Bañares, *Catalysis Today*, 2003, **78**, 219-228.
20. D. Courcot, B. Grzybowska, Y. Barboux, M. Rigole, A. Ponchel and M. Guelton, *Journal of the Chemical Society, Faraday Transactions*, 1996, **92**, 1609-1617.
21. A. Klisińska, S. Loidant, B. Grzybowska, J. Stoch and I. Gressel, *Appl Catal A Gen*, 2006, **309**, 17-27.
22. R. Grabowski and J. Słoczyński, *Chemical Engineering and Processing: Process Intensification*, 2005, **44**, 1082-1093.
23. F. Holtzberg, A. Reisman, M. Berry and M. Berkenblit, *Journal of the American Chemical Society*, 1956, **78**, 1536-1540.
24. J. J. Yeh and I. Lindau, *Atomic Data and Nuclear Data Tables*, 1985, **32**, 1-155.
25. P. Kube, B. Frank, S. Wrabetz, J. Kröhnert, M. Hävecker, J. Velasco-Vélez, J. Noack, R. Schlögl and A. Trunschke, *ChemCatChem*, 2017, **9**, 573-585.
26. J. T. Grant, C. A. Carrero, F. Goeltl, J. Venegas, P. Mueller, S. P. Burt, S. E. Specht, W. P. McDermott, A. Chiericato and I. Hermans, *Science*, 2016, **354**, 1570-1573.
27. R. Baddour-Hadjean, A. Boudaoud, S. Bach, N. Emery and J. P. Pereira-Ramos, *Inorg Chem*, 2014, **53**, 1764-1772.
28. J. Zemek, P. Jiricek, O. Gedeon, B. Lesiak and A. Jozwik, *Journal of Non-Crystalline Solids*, 2005, **351**, 1665-1674.

29. V. N. Krasil'nikov, L. A. Perelyaeva, I. V. Baklanova, L. Y. Buldakova and M. Y. Yanchenko, *Russ J Inorg Chem*+, 2009, **54**, 1537-1542.
30. C. A. Carrero, R. Schloegl, I. E. Wachs and R. Schomaecker, *ACS Catalysis*, 2014, **4**, 3357-3380.
31. G. Catana, R. R. Rao, B. M. Weckhuysen, P. Van Der Voort, E. Vansant and R. A. Schoonheydt, *The Journal of Physical Chemistry B*, 1998, **102**, 8005-8012.

4.8 Appendix

Table S 4.1. EDX diffractogram for catalyst 15KV, as synthesized.

Spectrum	C	O	Si	K	V	V/K
22200_ov01.spx	6.137014	46.71657	43.88016	0.244174	3.022083	12.37674
22200_ov02.spx	5.590568	54.36364	37.33524	0.197952	2.512602	12.693
22200_ov03.spx	9.819829	55.56578	31.68713	0.274176	2.653082	9.67655
22200_ov04.spx	5.481526	49.9194	41.18171	0.249748	3.167615	12.68322
22200_ov05.spx	9.00857	53.2297	31.04132	0.874487	5.84592	6.684968
Mean value:	7.207501	51.95902	37.02511	0.368108	3.44026	9.345798

Table S 4.2. EDX diffractogram of spent 15KV.

Spectrum	C	O	Si	K	V	V/K
22920_ov01.spx	14.4675	55.4078	26.3859	0.333591	3.405215	10.20774
22920_ov02.spx	7.958839	52.86136	35.51247	0.35723	3.3101	9.26602
22920_ov03.spx	11.51484	43.01753	41.59201	0.342696	3.532925	10.30921
22920_ov04.spx	10.0963	47.97267	37.83707	0.35509	3.738866	10.52934
22920_ov05.spx	13.81376	52.87911	29.07665	0.434002	3.796477	8.747599
Mean value:	11.57025	50.4277	34.08082	0.364522	3.556716	9.757209

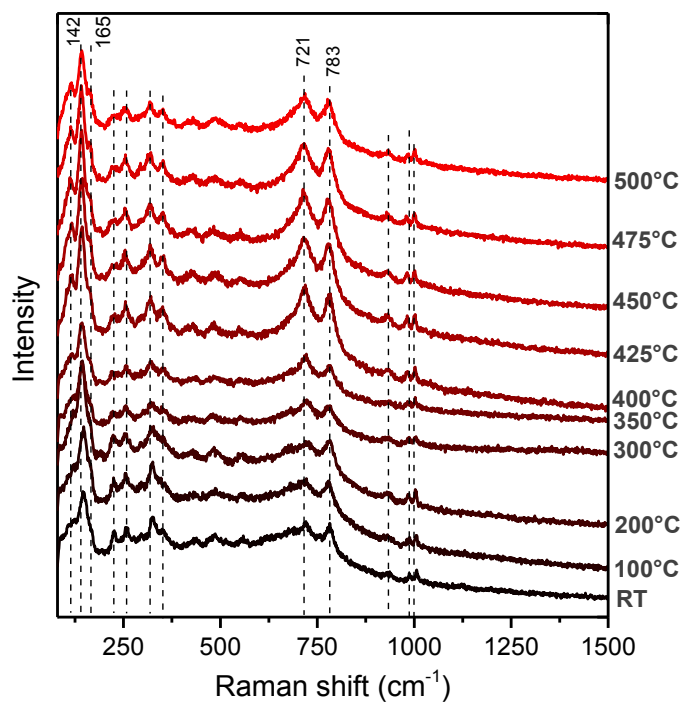


Figure S 4.1. In-situ Raman spectroscopy of catalyst 15KV under ODP reaction conditions via heating, feed composition: $\text{C}_3\text{H}_8:\text{O}_2:\text{N}_2$ 7.5:7.5:85, flow: 5 ml/min, Temperature: 25-500 °C.

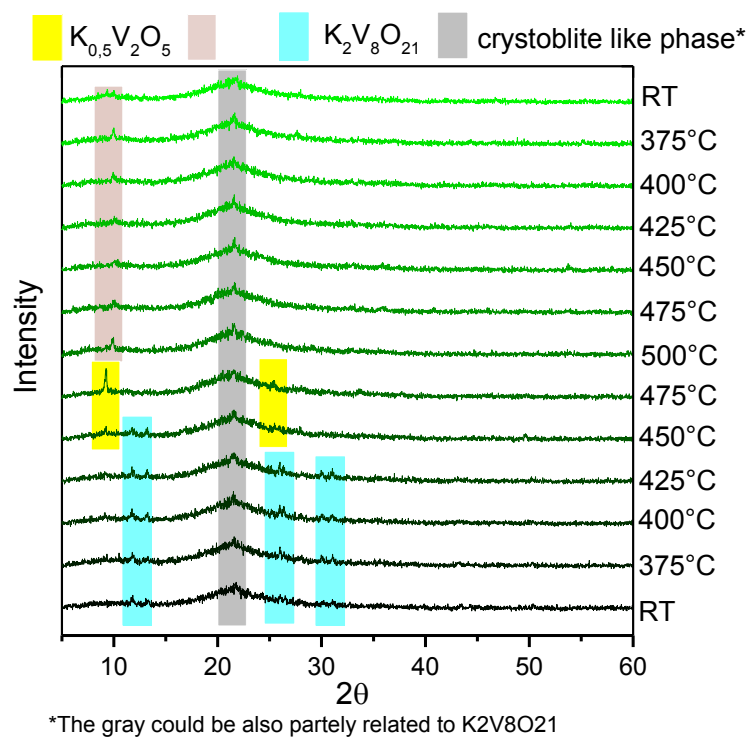


Figure S 4.2. Temperature dependent XRD under the flow of propane.

5 Summary and final conclusions

The performed study was intended in use of a rather new area of catalysts, so called SLP catalysts, in oxidative dehydrogenation of lower alkanes. With the aim of getting better insights into the structural-activity relationships, the catalytic data were measured below and above the melting point. For the preparation of the catalysts, to find the proper composition, the phase diagram of $K_2O-V_2O_5$ has been applied. The potassium content of 20-40 at% in the coating was applied for synthesis of SLP catalysts, due to proper melting point of formed potassium vanadates, being in the range of 400-500 °C. The potassium content below 20 which end up with a solid coating layer under the reaction conditions, 350-500 °C, was employed for preparation of solid catalysts. Preparation of selected alkali vanadates along with full characterizations enabled an insight into the course of stability of this material at elevated temperatures. Herein the intent was to create a complete data set applicable as fingerprint for in-situ characterization of supported catalysts. This study tries to go one step further by using DFT calculations to determine vibrational assignments to the Raman and IR spectral features of crystalline $K_2V_8O_{21}$ and $K_3V_5O_{14}$. $K_3V_5O_{14}$ which is stable under the molten state is interesting for catalysis related application with respect to preparation of supported liquid phase catalysts.

The reactivity measurements of SLP catalysts at elevated temperatures confirm the ability of a liquid layer in activation of lower alkanes. The influence of phase transition from solid to

liquid on performance of supported potassium vanadates in terms of decrease in activity but increase in propene selectivity at comparable conversion and temperature has been exhibited. The possible reasons for increase in selectivity after liquefaction were investigated applying in-situ spectroscopy and kinetic studies. The prominent reasons for higher selectivity of molten layer are proposed as following:

- A decline in coordination number via partial breaking of bridging bonds demonstrated by UV-Vis spectroscopy and Raman,
- and consequently, change of kinetic of reaction

The conducted study about performance of SLP catalysts before and after melting can let on detailed structural-activity correlations that will contribute to a better understanding of the effect of coordination environment in heterogeneous catalysis. Vanadium species in tetrahedral geometry which are corner linked are considered as active species in SLP catalysts. A loss of surface area after melting point of coating could contribute to a decline in activity for the molten layer. This inspires us to propose a new concept for achieving well performing catalysts. Increased coordination number in the structure of active species, being probably beneficial for activity, does not have a positive effect on propene selectivity. Staying in an optimum configuration which provides species with low coordination number but still active enough could bring the maximum productivity for the new designed catalysts.

It should be taken into account that the lower coordination number can be also achieved by potassium doped vanadium system, via partial breaking of bridging bond when potassium is introduced into the system. This hypothesis was investigated applying the prepared supported solid catalysts. On account of performed experiments it can be concluded that the thermal spreading method with the applied conditions (K:V 15:85, Temperature of calcination: 700 °C, loading : 8.4 wt %) is quite promising for synthesis of potassium doped vanadium monolayer catalyst. In-situ formation of potassium doped vanadium monolayer is most likely responsible for the good performance of this catalyst. Raman and UV-vis spectroscopy suggest presence of vanadium in tetrahedral environment accompanied by vanadium in higher coordination numbers initiating from presence of potassium octavanadate. The phase pure $K_2V_8O_{21}$ provides very low activity in oxidation of propane followed by fast deactivation. Accordingly, despite a certain amount of high coordinated species coexist, low coordinated vanadium has been suggested to be the relevant catalyst

precursors. The present $K_2V_8O_{21}$ is served as a sink to remove excess of vanadium and potassium from system. It can be expressed by use of heterogeneous two-phase systems; one part being a sink for excess amount of elements, whereas the real active phase are located in the second part.

Abbreviations

BET	Brunauer Emmett Teller
GC	Gas Chromatography
GHSV	Gas Hourly Space Velocity
SEM	Scanning Electron Microscopy
TCD	Thermal Conductivity Detector
XRD	X-Ray Diffraction
XPS	X-Ray Photoelectron Spectroscopy
BE	Binding Energy
TEM	Transmission Electron Microscopy
XAS	X-Ray Absorption Spectroscopy
XRF	X-Ray Fluorescence Spectroscopy
DSC	Differential Scanning Calorimetry
EDX	Energy Dispersive X-Ray
UV-Vis	Ultraviolet-Visible
IR	Infrared

List of Figures

Figure 1.1. Yields of various propene production processes.....	2
Figure 1.2. Potential structures of supported vanadium oxide surface species on fully oxidized and partially reduced surfaces; color code: vanadyl oxygen in purple, V-O-V bridges in blue, V-O-support bridges in green, vanadium hydroxyl groups in red.	3
Figure 1.3. HR-TEM of the a) basal b) prism c) Non-crystalline adlayer on the surface of a VPP particle.	4
Figure 1.4. Molecular structural models for vanadium species in sulfuric acid catalyst (adopted from Ref 24)	6
Figure 2.1. XRD patterns and Rietveld refinements of a) $K_2V_8O_{21}$ and b) $K_2V_8O_{21} K_3V_5O_{14}$	20
Figure 2.2. Polyhedral diagram of a) $K_2V_8O_{21}$ viewed along the b axis, b) $K_{0.5}V_2O_5$ viewed along the a axis.....	22
Figure 2.3. Polyhedral diagram of $K_3V_5O_{14}$	22
Figure 2.4. DSC of $K_2V_8O_{21}$ and $K_3V_5O_{14}$ under 70 ml/min O_2/Ar 21/79, heating rate: 10 Kpm.	23
Figure 2.5. Room temperature ATR-IR of $K_2V_8O_{21}$ accompanied by calculated IR active vibrational modes (Calc.). General vibrational assignments from DFT calculations are indicated.	24
Figure 2.6. Room temperature ATR-IR of $K_3V_5O_{14}$ accompanied by calculated IR active vibrational modes (Calc.). General vibrational assignments from DFT calculations are indicated.	25
Figure 2.7. The room temperature Raman spectrum of $K_2V_8O_{21}$ accompanied by calculated Raman active vibrational modes (Calc.). General vibrational assignments from DFT calculations are indicated.....	27
Figure 2.8. Comparison of experimental and calculated Raman spectra of $K_3V_5O_{14}$	27
Figure 2.9. Temperature dependent Raman of $K_2V_8O_{21}$ during heating up to the melting point under the flow of 5 ml/min O_2/Ar 21/79, a) spectra from room temperature to 520 °C, normalized to (0-1), b) enlargement of vibrational modes at higher Raman shifts.	28
Figure 2.10. Raman spectroscopy of $K_2V_8O_{21}$ after reaching the melting point a) holding in the molten state b) via cooling in the in-situ cell.....	29
Figure 2.11. Comparison of XRD of $K_2V_8O_{21}$ with the sample after high temperature Raman analysis.	30
Figure 2.12. Temperature dependent Raman of $K_3V_5O_{14}$ under 5 ml/min 21% O_2 in He.	32
Figure 2.13. Comparison of Raman spectra of $K_3V_5O_{14}$ in the solid and molten states.....	32
Figure 2.14. UV-Vis spectra of $K_2V_8O_{21}$ in dehydrated state.	33
Figure 2.15. Temperature dependent UV-Vis spectra of $K_2V_8O_{21}$ under the flow of O_2/He 21/79, a) temperature dependent UV-Vis spectra of dehydrated sample from room temperature to 500 °C, b) spectra from 500 °C to the melting point, g) spectra taken at 520 °C over 5 h.	34
Figure 2.16. UV-Vis spectrum of $K_3V_5O_{14}$ after dehydration.	35
Figure 2.17. Temperature dependent UV-Vis spectroscopy of $K_3V_5O_{14}$ under 5 ml/min 21% O_2 in He.	36
Figure 3.1. XRD patterns of xKV catalysts recorded at room temperature after synthesis [The patterns are offset for clarity].	60
Figure 3.2. Raman spectra of the freshly prepared catalysts recorded at room temperature.	61
Figure 3.3. SEM images of a) as-prepared catalyst 35KV, and b) Aerosil support.	62
Figure 3.4. SEM image and elemental mappings of catalyst 35KV.	62
Figure 3.5. DSC profiles of the xKV catalysts with the heating rate of 10Kpm under 70 ml/min flow of 21 % $O_2/79$ % Ar. DSC of $K_3V_5O_{14}$ and $K_2V_8O_{21}$ are also included for comparison.	63
Figure 3.6. XRD patterns of catalysts a) 35KV, b) 27KV, under the flow of 10 ml/min 21 % $O_2/79$ % Ar recorded at different temperatures (heating rate of 10Kpm and cooling rate of 5Kpm)	65
Figure 3.7. Surface-near a) K/Si, b) V/Si, and c) V/K ratios as a function of the analytical bulk values determined by XRF	67
Figure 3.8. Deconvolution of K2p spectra applying four peaks.....	68
Figure 3.9. a) Selectivity versus conversion in oxidative dehydrogenation of propane, feed composition $C_3H_8:O_2:N_2$ 10:5:85, W/F=1.8 gs/ml, m_{cat} = 300 mg b) Contact time variation at 475 °C, feed composition $C_3H_8:O_2:N_2$ 10:5:85 %, W/F=0.9-1.2-1.8-2.25 gs/ml, m_{cat} = 300 mg	69
Figure 3.10. a) Conversion of propane in the oxidative dehydrogenation of propane with increasing temperature, and b) propene selectivity as a function of propane conversion in the temperature range below and above the conversion drop over the catalysts indicated in the legend; feed composition $C_3H_8:O_2:N_2$ 7.5:7.5:85 %, contact time: 1.8 gs/ml, mass of catalyst: 300 mg.	70
Figure 3.11. Propane consumption rates in the ODP feed of $C_3H_8:O_2:N_2$ 7.5:7.5:85% and contact time of 1.8 g.s/ml, as a function of vanadium content on the surface determined by XPS a) at 390 °C b) at 490 °C.....	71
Figure 3.12. comparison of Product distribution for solid and super-cooled liquid. Feed $C_3H_8:O_2:N_2$ 7.5:7.5:85%, Conversion:0.3-0.4%, T:370 °C, CT_{solid} : 0.3 g.s/ml, CT_{liquid} : 6.6 g.s/ml.	72

Figure 3.13. XRD patterns of spent xKV catalysts, one month time on stream.	75
Figure 3.14. Raman spectroscopy of spent xKV catalysts at room temperature after one month time on stream.	76
Figure 3.15. DSC profiles of spent xKV catalysts after one month time on stream, heating rate: 10Kpm, under the flow of 70 ml/min 21 % O ₂ / 79 % Ar.	76
Figure 3.16. SEM of spent catalyst 35KV after one month time on stream.	77
Figure 3.17. SEM image and elemental mappings of spent catalyst 35KV, after one month time on stream.	78
Figure 3.18. V2p(3/2) and K2p core level XPS spectra of catalyst 35KV via heating and cooling	79
Figure 3.19. In-situ Raman of catalyst 35KV under reaction conditions; feed: C ₃ H ₈ :O ₂ :He-7.5:7.5:85; flow rate 5.5 ml/min; mass of catalyst:40 mg a) Raman spectra via heating, b) comparison of Raman spectra after cooling in-situ cell with fresh catalyst.....	81
Figure 3.20. Temperature dependent intensity of K ₃ V ₅ O ₁₄ vibrational modes during in-situ experiment of catalysts 35KV under the ODP reaction feed, feed: C ₃ H ₈ :O ₂ :He-7.5:7.5:85; flow rate 5.5 ml/min; mass of catalyst:40 mg	82
Figure 3.21. Comparison of Raman spectra of 35KV at room temperature with that of 500 °C (molten state) taken under reaction conditions , feed: C ₃ H ₈ :O ₂ :He-7.5:7.5:85; flow rate 5.5 ml/min; mass of catalyst:40 mg ..	83
Figure 3.22. Comparison of Raman spectra of K ₃ V ₅ O ₁₅ measured in the molten state with that of catalyst 35KV measured after melting under the ODP reaction conditions (feed: C ₃ H ₈ :O ₂ :He-7.5:7.5:85; flow rate 5.5 ml/min; mass of catalyst:40 mg).....	83
Figure 3.23. In-situ UV-Vis spectroscopy of catalyst 35KV under the ODP reaction conditions, feed: C ₃ H ₈ :O ₂ :He 7.5:7.5:85; flow rate 2 ml/min; mass of catalyst:10 mg a) UV-Vis spectra via heating b) Correlation of the reaction data taken form in-situ UV-Vis cell and intensity of UV-Vis spectra at 480 nm	84
Figure 3.24. Deconvolutions of UV-Vis spectra in the solid and molten states under ODP reaction conditions. ...	85
Figure 4.1. XRD patterns of xKV catalysts recorded at room temperature after synthesis. The patterns are offset for clarity.	101
Figure 4.2. a) Selectivity versus conversion, b) propene selectivity at 8% conversion as a function of potassium content (at%) in the coating, in oxidative dehydrogenation or propane, feed composition C ₃ H ₈ :O ₂ :N ₂ 7.5:7.5:85, Temperature: 450-500 °C (for catalyst 100V, 410-475 °C), contact time: 1.8 gs/ml.	103
Figure 4.3. Raman spectra of freshly prepared catalysts, a) Overview, b) Zoom in at around 1000 cm ⁻¹	103
Figure 4.4. DSC patterns of prepared catalysts under the flow of 70 ml/min 21 % O ₂ / 79 % Ar with the heating rate of 10Kpm	105
Figure 4.5. a) V2p(3/2) and b) K2p core level XPS spectra of as prepared 15KV sample after Shirley background subtraction and charging correction.	106
Figure 4.6. SEM images of a) Aerosil 300 and b) as-prepared catalyst 15KV.	106
Figure 4.7. SEM image and elemental mappings of catalyst 15KV.	107
Figure 4.8. XRD patterns of spent xKV catalysts, one month time on stream.	108
Figure 4.9. Comparisons of the Raman spectra of spent catalysts a) Over view, b) Zoom in at around 1000 cm ⁻¹	109
Figure 4.10. SEM of spent catalyst 15KV after one month time on stream.	110
Figure 4.11. SEM image and elemental mappings of spent catalyst 15KV, after one month time on stream. ...	110
Figure 4.12. a) V2p(3/2) and b)K2p core level XPS spectra of spent 15KV catalyst after Shirley background subtraction and charging correction.	111
Figure 4.13. Temperature dependent XRD of catalyst 15KV under the flow of 10 ml/min 21 % O ₂ /79 % Ar.	112
Figure 4.14. a) V2p(3/2) and b) K2p core level XPS spectra of catalyst 15KV via heating and cooling.....	112
Figure 4.15. In-situ Raman spectroscopy of catalyst 15KV under ODP reaction conditions with the feed composition of C ₃ H ₈ :O ₂ :N ₂ 7.5:7.5:85, a) Raman spectra and activity data while keeping at 500 °C, flow: 2 ml/min b) comparison of Raman spectra taken in different conditions	114
Figure 4.16. Comparison of UV-Vis spectrum of catalyst 15KV with that of K ₂ V ₈ O ₂₁	116
Figure 4.17. In-situ UV-Vis spectra of catalyst 15KV under ODP reaction conditions (C ₃ H ₈ :O ₂ :N ₂ 7.5:7.5:85 %, m _{cat} : 10mg, Flow: 2 ml/min).....	117
Figure 4.18. In-situ UV-Vis spectroscopy of catalyst 15KV under the ODP reaction conditions at 500 °C (C ₃ H ₈ :O ₂ :N ₂ 7.5:7.5:85 %, m _{cat} : 10mg, Flow: 2 ml/min) a) UV-Vis spectra over 12 hr time on stream, b) Comparison of reactivity data with the intensity of UV-vis band at 700 nm.....	118

List of tables

Table 2.1. Crystal data for prepared $K_2V_8O_{21}$ and $K_3V_5O_{14}$	21
Table 3.1. Physical and chemical properties of prepared catalysts	58
Table 3.2. Calculated Percentage of potassium vanadates in the coating of xKV catalysts by comparison of area of endothermic peak corresponding to melting of $K_3V_5O_{14}$ and $K_2V_8O_{21}$ in DSC heating curves of compounds with that of xKV catalysts. The amount of hexavanadate like phase has been calculated by subtraction of percentage of $K_3V_5O_{14}$ and $K_2V_8O_{21}$ in the coating from 100.	66
Table 3.3. Surface-near molar ratios of as prepared xKV catalysts according to XPS.	66
Table 3.4. Kinetic data below (380 °C) and above (480 °C) the melting point for catalyst 35KV, mass of catalyst: 100 mg, CT: 0.6 gs/ml.	73
Table 3.5. Physical properties of spent xKV catalysts, after being one month under ODP reaction conditions. ..	74
Table 3.6. The surface-near elemental ratios during heating in XPS cell (small amount of O_2 (2×10^{-8} mbar) was dosed into the UHV chamber during the experiment)	79
Table 4.1. Physical and chemical properties of prepared catalysts	100
Table 4.2. Content of $K_2V_8O_{21}$ in the coating of prepared catalysts obtained by quantification of DSC analysis, and propene yield and productivity of catalysts at ODP feed of $C_3H_8:O_2:N_2$ 7.5:7.5:85 at 500 °C (475 °C for catalyst 100V)	104
Table 4.3. Quantification of DSC melting signal	105
Table 4.4. Surface-near molar ratios of catalyst 15KV according to XPS.....	106
Table 4.5. Physical properties of spent xKV catalysts, after being one month under ODP reaction conditions.	108
Table 4.6. Near-surface composition of catalyst 15KV at different temperatures in the XPS cell (small amount of O_2 (2×10^{-8} mbar) was dosed into the UHV chamber during the experiment)	113

List of contributions/supports:

- Dr. Yuanqing Wang (DFT calculations)
- Pierre Kube (reactivity measurement supports)
- Dr. Frank Girgsdies (XRD measurement and analysis)
- Dr. Detre Teschner (XPS measurement and analysis)
- Dr. Olaf Timpe (XRF measurement)
- Jasmin Allan (TG-MS measurement)
- Dr. Marc Willinger and Wiebke Frandsen (SEM and analysis)
- Dr. Thomas Lunkenbein (TEM and analysis)
- Maike Hashagen (IR spectroscopy)